Karlsruhe Institute of Technology

Department of Physics
Institute of Experimental Particle Physics

Application Cases of Transverse Energy Filters in the KATRIN Experiment

Master’s Thesis
of

Joscha Nepomuk Lauer

at the Institute of Experimental Particle Physics

Reviewer:	Prof. Dr. Guido Drexlin
Second Reviewer:	Prof. Dr. Kathrin Valerius
Advisor:	Dr. Anton Huber
Second Advisor:	M. Sc. Dominic Hinz

Submission: July 7th, 2022

Declaration of Authorship

I truthfully affirm that I have written the work independently, that I have completely and precisely specified all aids used and that I have identified everything that has been taken from the work of others unchanged or with modifications, as well as having complied with the “Satzung zur Sicherung guter wissenschaftlicher Praxis am Karlsruher Institut für Technologie (KIT)” (statutes for safeguarding good scientific practice at the KIT) in the valid version of October 5th, 2021. [KIT15]

Ich versichere wahrheitsgemäß, die Arbeit selbstständig verfasst, alle benutzten Hilfsmittel vollständig und genau angegeben und alles kenntlich gemacht zu haben, was aus Arbeiten anderer unverändert oder mit Abänderungen entnommen wurde sowie die Satzung zur Sicherung guter wissenschaftlicher Praxis am Karlsruher Institut für Technologie (KIT) in der gültigen Fassung vom 5. Oktober 2021 beachtet zu haben. [KIT15]

Eggenstein-Leopoldshafen on July 6th, 2022

Joscha Nepomuk Lauer

Accepted as **examination copy**.

Eggenstein-Leopoldshafen on July 6th, 2022

Prof. Dr. Guido Drexlin

Contents

1. Introduction

After photons, neutrinos are the second most abundant particles in our cosmos [Zub20]. Although their interactions are weak, neutrinos play an important role on the small scale of nuclear processes because of their participation in beta decay, but also on the giant cosmic scales since they act as "cosmic architects" in the evolution of large scale structures. The latter is possible due to their non-vanishing mass. Neutrino experiments provide evidence for oscillations between the different flavors of the weak interaction's eigenstates in the late 1990s. These oscillations can only occur in the case of massive neutrinos. Neutrinos are massless in the Standard Model of particle physics. Thus, neutrino oscillations require an extension by means of physics beyond the Standard Model. Although the absolute differences of the three neutrino mass states are known, the scale of their absolute mass itself is not. Numerous observations and experiments restricted the mass to small values below half a millionth of the electron mass, which is the lightest of the remaining massive elementary particles, giving rise to a puzzling discrepancy of the elementary fermions' mass scales. Hence, many experiments aim to further restrict and also measure its value.

The most stringent direct and model-independent constraint on the effective electron anti-neutrino mass is set by the Karlsruhe Tritium Neutrino Experiment (KATRIN) [A$^+$21c, A$^+$22], which provides an upper limit of

$$m_\nu < 0.75\,\mathrm{eV}c^{-2}\;(90\,\%\,\mathrm{C.L.}). \tag{1.1}$$

This value is still above the design sensitivity of $m_\nu < 0.2\,\mathrm{eV}c^{-2}$ (90 % C.L.) after 1000 days of data-taking, but already corresponds to sub-electronvolt sensitivity after 50 days. The subject of investigation is beta decay of molecular tritium from the windowless gaseous tritium source, wherein an activity of 10^{11} Bq is achieved by high throughput of gas. Precise spectroscopy of the emitted electron energies allows to infer the neutrino mass, because it causes a slight shift of the spectral endpoint at $E_0 = 18.6\,\mathrm{keV}$ and a deformation of the spectrum. In spite of the high decay rate, only long measuring times result in sufficient statistics, because a very small fraction acquires energies in the relevant region close to the endpoint. The principle of magnetic adiabatic collimation combined with an electrostatic filter (MAC-E) makes the main spectrometer (MS) a high-pass filter with an excellent energy resolution of $\Delta E = 2.77$ eV (design value of $\Delta E = 0.93$ eV) for the measurement of the integral beta spectrum. To achieve the design sensitivity, further prerequisites have to be met. The major issue is the current background level, ranging by a maximum factor of about 25 above the design value.

With a volume of $1240\,\mathrm{m}^3$ the MS is the world's largest ultra-high vacuum tank. Previous works show that the inner stainless steel surface is contaminated with progenies of the nuclide ^{222}Rn, resulting in an implantation of ^{210}Pb in the steel. Alpha decays of this contaminant give rise to excited neutral messenger particles, propagating into sensitive magnetic fluxtube regions in the MS volume, where they are ionized, i.e. emit electrons, due to processes that are still subject to ongoing research. These electrons constitute the "remaining background" in the experiment.

Different models (e.g. room temperature black body radiation-induced Rydberg state-ionization) and measurements indicate electrons with energies in the 100 meV regime. From the creation process and subsequent propagation through the electromagnetic fields of the experiment, it can be concluded that the shape of their trajectories in general differs from the trajectories of beta electrons, as they reach the focal plane detector. In contrast to beta electrons, the gyroscopic propagation of these background electrons along guiding magnetic field lines is governed by the much more pronounced longitudinal component of motion. [F+22]

This circumstance can be exploited by the application of transverse energy filters (TEFs). Their three-dimensional structure provides access to the spatial profile of electron trajectories, characterized by a certain gyroradius and pitch angle, which relates the transverse and longitudinal component of motion. A passive TEF structure (pTEF) acts as a low-pass filter, mainly transmitting low pitch angle electrons like the background electrons. The actual rate reduction could prove certain assumptions regarding the creation mechanisms of the remaining background and serve as a proof of principle for the TEF approach. On the other hand, the signal-to-background ratio could be improved towards the required level with an active TEF (aTEF), relying on active detection of mainly signal electrons with the structure. Thus, TEFs represent a novel possibility of background discrimination and also characterization in the KATRIN experiment.
Both applications are investigated in this work. In the first part it is aimed towards a simulation-based characterization of background electrons regarding their important properties for filtering using the software package *Kassiopeia*. The dependence on the spectrometer settings is worked out for background electrons from a Rydberg-mediated model and radon decays. It is concluded that the distributions can be tuned by application of different magnetic field and retarding voltage settings. In addition, the expected filtering properties and systematic effects are important for the first pTEF campaign and are thus studied for both the pTEF and a conceptual double pTEF (2pTEF). Systematics due to geometric aspects are found to be on the few percent scale for the pTEF, whereas the considered aspects for the 2pTEF could already cause an effect at the 10 % level.

In case of the aTEF, a novel detector concept is introduced and investigated: the scintillating aTEF (scint-aTEF) relies on a microstructured scintillator grid as active filter component, combined with a single-photon avalanche diode (SPAD) detector. This work gives an extensive overview of the concept and requirements but also addresses the current research and development (R&D) status. The properties of a scint-aTEF are investigated, based on a simulation environment that is set up using the toolkit *Geant4*. Detector concepts are also established and implemented. A dedicated detector layout is optimized. Moreover, a strategy to discriminate dark current of the detector is proposed and investigated. Altogether, the results suggest the feasibility of beta electron detection with the scint-aTEF structure, while reducing the background level. However, R&D is ongoing as several practical hurdles have to be overcome. A short overview of the experimental status is provided.

This thesis is structured in six parts. A comprehensive presentation of the historic progress in neutrino physics, the phenomenon of neutrino oscillations and the determination of the neutrino mass is given in chapter 2. The KATRIN experiment is explained in chapter 3. Background sources are also addressed in detail.
Afterwards, chapter 4 gives an overview on the principle and current status of TEFs. The studies concerning the pTEF application are found in chapter 5. After an introduction to the first pTEF, Kassiopeia simulations of background angular distributions and their results are discussed. This is followed by investigations of geometric systematics and simulations of the actual filtering properties. In chapter 6, basics of scintillators and photon detection are outlined and the scint-aTEF setup is explained. In addition to the physical setup, the virtual version in the Geant4 environment

is introduced with some general information on the simulation toolkit. The configuration of the scintillator grid is investigated, regarding its light collection properties and energy deposition as well as scintillation in the material. Finally, potential signatures and detector responses are established from the simulation results. The possibility of enhancing the signal-to-noise ratio of the setup with a certain trigger strategy is investigated. To account for the experimental progress that is made, a brief overview addressing this topic completes the chapter. Chapter 7 summarizes the work and a conclusion is drawn. It also provides an outlook to the perspective of the R&D and application of TEFs.

2. Neutrino Physics

In December 1930, Wolfgang Pauli writes a letter from Zürich to the “radioactive ladies and gentlemen” in Tübingen, addressing them with an urgent request: in light of the current puzzle of the continuous beta spectrum he proposes a solution which does, i.a., not require to violate the conservation of energy. A light-weight neutral particle, the “neutron” (which is called neutrino later by Enrico Fermi [Fer33]), allowed for an explanation of the observations while preserving the prevalent conservation laws. Since a particle with the properties he predicts is not discovered yet, Pauli’s request is to think of possible ways to detect the proposed particle. [Pau30]
After his letter it takes 26 more years until the first detection of the elusive particle is finally announced by Clyde Cowan and Frederick Reines in July 1956 [CR+56]. In the new sector of neutrino physics several findings and breakthroughs follow these milestones, which will be presented within this chapter: a summary of the neutrino’s history in section 2.1 is followed by section 2.2, which is dedicated to the phenomenon of neutrino oscillations. Afterwards, different methods for the determination of the neutrino mass are presented in section 2.3.

2.1. History of the Neutrino

After Henri Becquerel’s discovery of nuclear radiation in 1896 [Bec96], nuclear physics becomes an important topic around the beginning of the 20th century. Experiments with various radioactive samples reveal three radiation types which could be classified by their different penetration powers (“Durchdringungsvermögen” [Pau30]) and other properties. Ernest Rutherford labels them as alpha, beta and gamma radiation until 1903 [Rut99, Rut03]. It is discovered that nuclear decay results in the transmutation of elements [Faj13, Sod13].
As for alpha and gamma particles, a narrow energy distribution is expected for beta particles due to the assumed processes and kinematics. However, James Chadwick performs a momentous experiment to follow preceding indications on a continuous energy spectrum of beta radiation: using a magnetic spectrometer and a Geiger counter, he measures the spectra of “radium B” (lead-214) and “radium C” (bismuth-214) with never before achieved precision to be clearly continuous and broad contrarily to the assumption [Cha14]. As the understanding of beta decay – the emission of nothing but a beta particle by the nucleus – is that of a two-body decay at this time, the decay products should have discrete energies determined by their masses’ ratio under the prerequisite of energy conservation.
Instead, Chadwick’s findings provide spectra which imply a loss of fractions of energy which are determined statistically, if the description as two-body decay was correct. This would mean that conservation of energy was violated within the process. Additionally, it becomes clear that the decay would also imply a violation of the conservation of angular momentum: because beta decay leaves the atomic mass number unchanged, the nuclear spin can only change by an integral multiple of $\hbar$ within the process. The fact that electrons and positrons are spin-$1/2$ particles is not

in agreement with this behavior if one requires the prevalent conservation laws to be valid, thus being known as the “problem of the spin and statistics” of the nucleus.

In both cases, the energy and the spin puzzle, some quantity seems to be carried away by a particle which could obviously not be detected. This motivates Pauli to pursue the idea of a barely interacting (he states electrical neutrality) spin-$1/2$ particle, carrying away the missing energy. Also, the particle should have a mass not above the order of the electron’s mass and below one percent of the proton’s mass [Pau30]. Fermi provides an extensive theoretical foundation for the neutrino and beta decay later [Fer34]. Back then, the cross section σ of interactions with atomic nuclei is estimated to be $\sigma < 10^{-44}\,\mathrm{cm}^2$ which translates to a penetrating power of 10^{16} km in solid matter [BP34].

The first successful attempt to detect the “poltergeist” is made by Clyde Cowan and Frederick Reines in the 1950s. Next to a nuclear reactor, electron anti-neutrinos $\bar{\nu}_e$ interact via inverse beta decay, which reads

$$\bar{\nu}_e + p \longrightarrow n + e^+, \tag{2.1}$$

with the protons p of water molecules. Decay processes within the Savannah River reactor provide an intense neutrino flux. The annihilation of the ejected positron e^+ results in a pair of gamma quanta, both with an energy of 511 keV, while the neutron n propagates for a longer time and is moderated throughout this process. Because of its capability to capture thermalized neutrons with subsequent gamma emission, 40 kg cadmium chloride (isotope ^{113}Cd) are added to the 200 l of water. Scintillators and photomultiplier tubes (PMTs) are used to detect the photons using the photons’ delayed coincidence. The efforts result in a reaction rate of about three reactions per hour which can be assigned to neutrinos from the reactor; the neutrino is finally confirmed. [CR+56]

As the charged leptons, neutrinos also occur in three different families, corresponding to the lepton flavors $f_\ell = \{e, \mu, \tau\}$ (electronic, muonic, tauic). Despite their very similar properties, detection has to be be achieved with different approaches depending on the flavor. In 1962, Jack Steinberger, Leon Ledermann and Melvin Schwartz provide evidence of a neutrino with different flavor. It is the muon neutrino ν_μ. Charged mesons, namely pions π, are produced by bombardment of a beryllium target with protons from the Brookhaven accelerator. The decay of pions follows

$$\pi^\pm \longrightarrow \mu^\pm + \left(\nu_\mu/\bar{\nu}_\mu\right), \tag{2.2}$$

where a muon μ and a muon neutrino are produced. For detection, particles would have to pass through a massive 5000 t of steel which the neutrinos will easily penetrate (vide supra, cf. [Fer34]). Hence, it acts as a shielding for the neon-filled spark chamber detector, filtering out everything besides neutrinos, which can then be detected indirectly by means of a muon, since

$$\nu_\mu + n \longrightarrow p + \mu^- \tag{2.3}$$

takes place with neutrons of the aluminum. This reaction is much alike equation 2.1. Yet, the lack of electrons clearly implies that another neutrino flavor (μ) is responsible for the events. [D+62]

Until evidence of the third neutrino flavor τ is provided experimentally, it requires a longer time span since it is postulated only after the tau’s discovery [P+75, K+01]. In 2001, first results of tau neutrino (ν_τ) interactions are published by the DONUT collaboration. As by Steinberger et al., a proton beam (from the Tevatron at Fermilab) is fired at a target to indirectly induce neutrino production. The beam dump for the 800 GeV protons consists of tungsten. Some of the therein produced strange D mesons (D_s^+) decay according to the branch

$$D_s^+ \longrightarrow \tau^+ + \nu_\tau. \tag{2.4}$$

Downstream of proper shielding, different combination of so-called emulsion targets and detector instrumentation allow for an identification of taus created analogously to equation 2.3 (with tauic flavor). At the experiment's energies, the track length of these leptons is around 2 mm until they decay into a lighter electron or muon and two corresponding neutrinos, fulfilling the conservation laws of the lepton family numbers. Typically, this decay causes a pronounced kink after the tau's propagation path, hence making an identification of the tau possible. [K⁺01]

To determine the number N_ν of light neutrino families, which was already stated to be three above, the Z^0 boson's resonance is investigated around 1990: precise measurements of the line shape at the large electron-positron collider (LEP) yield a value of $N_\nu = 3.01 \pm 0.15\,(\text{exp.}) \pm 0.05\,(\text{theo.})$, confirming three families or flavors f_ℓ [D⁺90]. From combination of all four experiments carried out at the LEP one obtains $N_\nu = 2.9840 \pm 0.0082$ [A⁺06].

2.2. Neutrino Oscillations

In this thesis, natural units will be used. This means that the speed of light c, the reduced Planck constant $\hbar$, the electron mass m_e and the vacuum permittivity ε_0 are defined as $c = \hbar = m_e = \varepsilon_0 = 1$. Nevertheless, they might occur explicitly in some cases on purpose.

2.2.1. Standard Model of Particle Physics

After a "time of confusion and frustration" in particle physics, the Standard Model (SM) of particle physics is established and brought to its final form in the 1970s [Wei04]. It is the model describing the known fundamental particles and their interactions, namely strong, weak and electromagnetic interactions, while gravitation is not included in the theory. All of its constituents are presented in figure 2.1, where the classification becomes evident. Two major classes make up the model: bosons with integral and fermions with half-integral spin. The former (vector or gauge bosons and a scalar boson) are force carriers mediating interactions, whereas the latter are considered as matter and divided on one hand into three generations, and on the other into two categories, quarks and leptons, due to the different interactions they are participating at (indicated by circlings between fermions and bosons in fig. 2.1). For example, only quarks interact strongly (via gluons), while neutrinos do not couple to any gauge bosons besides the ones mediating the weak force, Z^0 and the W bosons W^+ and W^-. The three flavors from section 2.1 match with the three generations of matter.

Despite the SM being very successful, it soon turns out that it can not explain some phenomena (besides gravity). One of them is the oscillation of neutrino flavors. In the course of neutrino physics research, the solar electron neutrino flux is measured to be lower than expected, pointing towards neutrino oscillations ("solar neutrino problem", cf. [Dav94, BB90]). This, in turn, implies massive neutrinos. However, non-zero masses of neutrinos can not be integrated into the model – they have to be massless in the SM. Thus, a theory beyond the Standard Model (BSM) is required to achieve a proper description.

2.2.2. Solar Neutrino Problem

The fact that neutrinos do not interact electromagnetically or strongly results in a propagation through space and time almost unperturbed by interstellar magnetic fields, or absorbed by matter. Thus, they are suitable cosmological messengers. On our earth's surface, solar neutrinos are the neutrino flux's main component over the entire keV-regime [Spi12]. With the Homestake experiment, which is the pioneer experiment for neutrinos as astrophysical messengers, Raymond Davis succeeds in both confirming nuclear fusion processes as the sun's energy source and

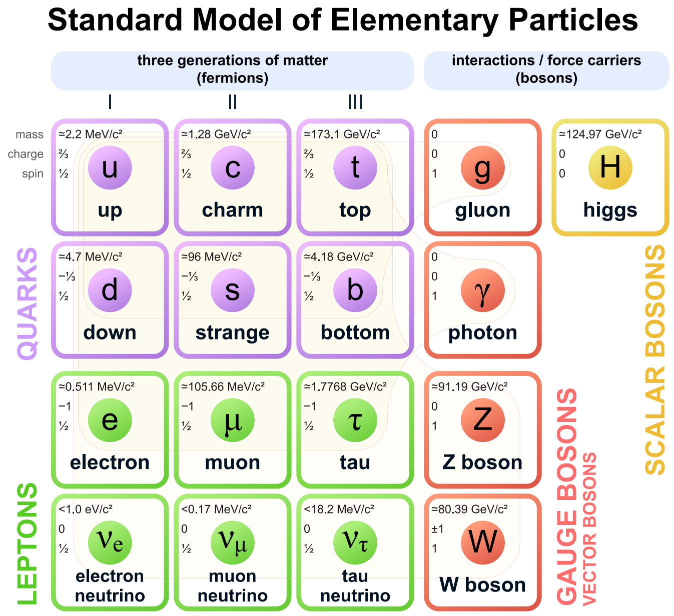

Figure 2.1.: Standard Model of particle physics (from [Wik21]): Left: The three generations of fermions (matter). The fermions divide into leptons and strongly-interacting quarks. Right: bosons, acting as force carriers. They occur as vector bosons (spin-1) and scalar boson (spin-0, higgs boson).

measuring the solar electron neutrino flux with a radiochemical approach [D$^+$98]. It is set up about 1.5 km below the shielding surface of earth in the Homestake gold mine, where a tank of 615 t perchloroethylene (PCE, C_2Cl_4) is located as detector. PCE is chosen because it is rich in chlorine. The isotope chlorine-37, accounting for 24.23 % of natural chlorine [SM05] and has a low energy threshold of $E_{\mathrm{min}} = 0.814\,\mathrm{MeV}$ for the neutrino capture reaction [D$^+$98]

$$\nu_e + {}^{37}\mathrm{Cl} \longrightarrow {}^{37}\mathrm{Ar}^+ + e^-. \tag{2.5}$$

The assumed model of fusion processes fueling the sun – established around the 1960s – indicate neutrino energies ranging from multiple kilo- to some megaelectronvolts, corresponding to different reactions of the proton-proton chain and the CNO cycle [B$^+$63, Bah64]. Mainly neutrinos originating from the β^+ decay of ^{8}B with energies of $E_\nu \lesssim 15\,\mathrm{MeV}$ [Zub20] participate in the reaction 2.5. The small amounts of produced ^{37}Ar can be quantified by exploiting its short half-life of only 35 days, allowing for the determination of the solar electron neutrino flux above E_{min}. Though, the flux obtained from 25 years of observation only amounts to only ⅓ of the theoretical prediction. This discrepancy is in accordance with the measurements of Kamiokande-II [H$^+$91] and other experiments and known as solar neutrino problem [D$^+$98]. An approach to overcome the problem are flavor transitions during propagation in space [Pon58b, BB90].

Indeed, the seeming deficit vanishes in 2001 with the SNO experiment, which finally solves the solar neutrino problem [A$^+$01]. Consisting of a 1000 t tank of heavy water (D_2O), the experiment is based on Cherenkov ring imaging. This is achieved by instrumentation of the walls with 9700 PMTs to capture the light produced by electrons, originating from neutrino interactions with D_2O. The usage of a deuterium-enriched target is beneficial, because in addition to charged current (CC) interactions like reaction 2.5 with contributions from electron neutrinos only, neutral current (NC) interactions and elastic scattering (ES) can be detected, both being flavor-independent.

Consequently, the muon and tau neutrinos of the solar neutrino flux contribute to the rate. The determined total flux is in agreement with the predicted value [A$^+$01]. The underlying mechanism of flavor transitions, the oscillation of neutrinos, is already discovered a few years in advance with Super-Kamiokande [F$^+$98]. Takaaki Kajita (Super-Kamiokande) and Arthur McDonald (SNO) are awarded with the Nobel Prize in Physics "for the discovery of neutrino oscillations, which shows that neutrinos have mass" in 2015 [Roy15]. Not only did they discover that, but also provided evidence for BSM physics with the results.

2.2.3. Oscillation Mechanism

Inspired by the oscillation of kaons, Bruno Pontecorvo proposes the oscillation of neutrinos in 1957 [Pon58a]. While his work addresses oscillations between neutrinos and anti-neutrinos, Ziro Maki, Masami Nakagawa and Shoichi Sakata pick up this idea for a theory of neutrino oscillations between flavors (only e and μ at this time) [MNS62]. Neutrino states can be represented in different bases: the base of the weak interaction's eigenstates, the three flavor states $|\nu_{f_\ell}\rangle$, or in terms of the eigenstates of the free Hamiltonian (mass states), denoted as $|\nu_j\rangle$ with indices $j = \{1, 2, 3\}$. While a certain flavor can be assigned to each $|\nu_{f_\ell}\rangle$, each mass state corresponds to a specific energy eigenvalue E_j and therefore to a mass m_j. The Pontecorvo-Maki-Nakagawa-Sakata (PMNS) matrix U is a unitary 3×3 matrix which describes the linear relationship between both bases. The relationship reads

$$\begin{pmatrix} |\nu_e\rangle \\ |\nu_\mu\rangle \\ |\nu_\tau\rangle \end{pmatrix} = \begin{pmatrix} U_{e1} & U_{e2} & U_{e3} \\ U_{\mu1} & U_{\mu2} & U_{\mu3} \\ U_{\tau1} & U_{\tau2} & U_{\tau3} \end{pmatrix} \begin{pmatrix} |\nu_1\rangle \\ |\nu_2\rangle \\ |\nu_3\rangle \end{pmatrix}, \tag{2.6}$$

where $U_{f_\ell j} = \langle \nu_j | \nu_{f_\ell} \rangle$ are the complex elements of U. Accordingly, the connection of flavor and mass states becomes evident:

$$\left|\nu_{f_\ell}\right\rangle = \sum_j U_{f_\ell j} \left|\nu_j\right\rangle \quad \text{and} \quad \left|\nu_j\right\rangle = \sum_{f_\ell} U^*_{f_\ell j} \left|\nu_{f_\ell}\right\rangle . \tag{2.7}$$

The following is based on [Z$^+$20]. Often a representation by three rotational matrices is used for the PMNS matrix. The concatenation is

$$U = \begin{pmatrix} 1 & 0 & 0 \\ 0 & \cos(\theta_{23}) & \sin(\theta_{23}) \\ 0 & -\sin(\theta_{23}) & \cos(\theta_{23}) \end{pmatrix} \begin{pmatrix} \cos(\theta_{13}) & 0 & \sin(\theta_{13})\,\mathrm{e}^{-\mathrm{i}\delta_{\mathrm{CP}}} \\ 0 & 1 & 0 \\ -\sin(\theta_{13})\,\mathrm{e}^{\mathrm{i}\delta_{\mathrm{CP}}} & 0 & \cos(\theta_{13}) \end{pmatrix} \begin{pmatrix} \cos(\theta_{12}) & \sin(\theta_{12}) & 0 \\ -\sin(\theta_{12}) & \cos(\theta_{12}) & 0 \\ 0 & 0 & 1 \end{pmatrix}. \tag{2.8}$$

Four independent parameters occur in this matrix: The mixing angles θ_{23}, θ_{13} and θ_{12} and the CP-violating Dirac phase δ_{CP}. Additionally, the Majorana phases α_1 and α_2 can be introduced to account for the possible Majorana nature of neutrinos. In case neutrinos are Majorana particles, these phases would be different from zero and added to the concatenation in equation 2.8 on the rightmost side in the form of $\mathrm{diag}\left(\mathrm{e}^{\mathrm{i}\alpha_1/2}, \mathrm{e}^{\mathrm{i}\alpha_2/2}, 1\right)$.

Of course, the neutrino states in equation 2.7 are time-dependent. Thus, a state $|\nu_{f_\ell}\rangle$ will evolve over time and in space as $\left|\nu_{f_\ell}(t, \vec{x})\right\rangle$. In the following, the states from equation 2.7 will correspond to the stationary initial states at the origin, i.e., $(t, \vec{x}) = (0, \vec{0})$. The free neutrino states propagate as plane waves in space and time. Hence, the evolution will be expressed in terms of the states $|\nu_j\rangle$ with energies E_j and momenta $\vec{p}_j$:

$$\left|\nu_j(t, \vec{x})\right\rangle = \mathrm{e}^{-\mathrm{i}\left(E_j t - \vec{p}_j \cdot \vec{x}\right)} \left|\nu_j\right\rangle = \mathrm{e}^{-\mathrm{i}p_j \cdot x} \left|\nu_j\right\rangle , \tag{2.9}$$

where $p_j \cdot x = p_j^\eta x_\eta$ is the scalar product of the four-vectors of momentum $p_j = (E_j, \vec{p}_j)$ and position $x = (t, \vec{x})$. With the PMNS matrix, the evolution of a flavor state is therefore

$$\left|\nu_{f_\ell}(t, \vec{x})\right\rangle = \sum_j U_{f_\ell j}\, \mathrm{e}^{-\mathrm{i} p_j \cdot x} \left|\nu_j\right\rangle \tag{2.10}$$

and the probability $\mathcal{P}(\nu_{f_{\ell,\mathrm{i}}} \longrightarrow \nu_{f_{\ell,\mathrm{f}}})$ to find a neutrino of initial flavor $f_{\ell,\mathrm{i}}$ in the flavor $f_{\ell,\mathrm{f}}$ at the spacetime position $x = (t, \vec{x})$ is given by the squared scalar product of the corresponding states:

$$\begin{aligned} \mathcal{P}(\nu_{f_{\ell,\mathrm{i}}} \longrightarrow \nu_{f_{\ell,\mathrm{f}}})(t, \vec{x}) &= \left|\left\langle \nu_{f_{\ell,\mathrm{f}}} \middle| \nu_{f_{\ell,\mathrm{i}}}(t, \vec{x})\right\rangle\right|^2 && (2.11) \\ &= \left|\sum_{i,j} U^*_{f_{\ell,\mathrm{f}} i} U_{f_{\ell,\mathrm{i}} j}\, \mathrm{e}^{-\mathrm{i} p_j \cdot x} \left\langle \nu_i \middle| \nu_j \right\rangle\right|^2 && (2.12) \\ &= \sum_{j,k} U_{f_{\ell,\mathrm{f}} j} U^*_{f_{\ell,\mathrm{i}} j} U^*_{f_{\ell,\mathrm{f}} k} U_{f_{\ell,\mathrm{i}} k}\, \mathrm{e}^{\mathrm{i} p_j \cdot x}\, \mathrm{e}^{-\mathrm{i} p_k \cdot x}. && (2.13) \end{aligned}$$

Orthonormality $\langle \nu_i | \nu_j \rangle = \delta_{ij}$ of states is used in the last step. As neutrinos are usually highly relativistic, $p := |\vec{p}_j| \simeq |\vec{p}_k|$ and $m_j \ll p$ hold and the energy relation $E_j = \sqrt{m_j^2 + \vec{p}_j^2}$ can be approximated omitting $\mathcal{O}((m_j/p)^4)$:

$$E_j \simeq p\left(1 + \frac{m_j^2}{2p^2}\right) \simeq p + \frac{m_j^2}{2E}. \tag{2.14}$$

After insertion of this result in equation 2.13 all momenta in the exponential cancel out. For relativistic neutrinos $t = ct$ is approximately the propagation distance L and equation 2.13 can be written as

$$\mathcal{P}(\nu_{f_{\ell,\mathrm{i}}} \longrightarrow \nu_{f_{\ell,\mathrm{f}}}) = \sum_{j,k} U_{f_{\ell,\mathrm{f}} j} U^*_{f_{\ell,\mathrm{i}} j} U^*_{f_{\ell,\mathrm{f}} k} U_{f_{\ell,\mathrm{i}} k}\, \mathrm{e}^{\mathrm{i} \frac{\Delta m_{jk}^2}{2E} L} = \mathcal{P}(\nu_{f_{\ell,\mathrm{i}}} \longrightarrow \nu_{f_{\ell,\mathrm{f}}})\left(\frac{L}{E}\right), \tag{2.15}$$

where $\Delta m_{jk}^2 := m_j^2 - m_k^2$ is introduced. By using the representation of U from equation 2.8 in this expression, terms with sums of powers of sine and cosine terms will occur, accounting for the mixing angles' contributions. In the chosen representation, it is however easy to see that the transition probability only depends on the ratio of neutrino energy E and the distance L and is oscillating, indeed. On the other hand, the PMNS matrix's elements and the squared masses' differences Δm_{jk}^2 – also referred to as mass splittings – are natural parameters. However, the above expression implies that flavor oscillations can only occur if neutrinos have a non-zero mass.

By exploiting the large range of the energies E and propagation lengths L between source and detector that can be found in arrangements on earth and in our solar system, the oscillation parameters are determined. Solar, atmospheric, accelerator and reactor neutrinos are suitable and used in such experiments. Table 2.1 contains the oscillation parameters from a global three-flavor oscillation fit [E⁺20]. With these, transition probabilities (eq. 2.15) can be calculated, for example. Another feature of equation 2.15 is, that the amplitude of both splittings in table 2.1 can be extracted based on oscillation behavior, but the ordering of the masses m_j is not definite, as well as the sign of $\Delta m_{31}^2 \approx \Delta m_{32}^2$. Therefore, different hierarchies of the m_j are possible: normal ordering $m_1 < m_2 \ll m_3$ and inverted ordering $m_3 \ll m_1 < m_2$ ($\Delta m_{21}^2 \ll |\Delta m_{3j}^2|$). If the absolute mass of all ν_j is large compared to the splittings, the masses are quasi-degenerated, i.e., $m_1 \approx m_2 \approx m_3$. Although oscillation experiments are providing an approach to all parameters in table 2.1, the absolute mass scale does not appear within the underlying theory, as this section describes. To determine it, different mechanisms are considered and exploited.

Table 2.1.: Neutrino mixing parameters from global three-flavor oscillation fit *NuFIT 5.0* in [E⁺20].

parameter	normal ordering	inverted ordering
$\sin^2(\theta_{12})$	$3.04^{+0.12}_{-0.12} \times 10^{-1}$	$3.04^{+0.13}_{-0.12} \times 10^{-1}$
$\sin^2(\theta_{23})$	$5.73^{+0.16}_{-0.20} \times 10^{-1}$	$5.75^{+0.16}_{-0.19} \times 10^{-1}$
$\sin^2(\theta_{13})$	$2.219^{+0.062}_{-0.063} \times 10^{-2}$	$2.238^{+0.063}_{-0.062} \times 10^{-2}$
δ_{CP}	$197^{\circ}{}^{+27^{\circ}}_{-24^{\circ}}$	$282^{\circ}{}^{+26^{\circ}}_{-30^{\circ}}$
Δm^2_{21}	$7.42^{+0.21}_{-0.20} \times 10^{-5}\,\mathrm{eV}^2$	$7.42^{+0.21}_{-0.20} \times 10^{-5}\,\mathrm{eV}^2$
Δm^2_{3j}	$+2.517^{+0.026}_{-0.028} \times 10^{-3}\,\mathrm{eV}^2$	$-2.498^{+0.028}_{-0.028} \times 10^{-3}\,\mathrm{eV}^2$

2.3. Determination of the Neutrino Mass

Various methods to constrain or measure the neutrino mass exist. They can be separated according to their model-dependence. Three model-dependent methods will be introduced in this section, followed by an independent approach.

The major part of the neutrino flux is provided by the cosmic (relic) neutrino background (CνB) in the low-energy (μeV – meV) regime. This part is followed by solar neutrinos. However, in 1987 the supernova SN 1987A produces an intense neutrino burst with a flux comparable to the solar neutrino flux in the multi-MeV regime [Spi12]. Both, cosmological and astrophysical supernova neutrinos, are suitable for constraining neutrino mass.
CνB neutrinos stem from the first moments of the universe. 1 s after the Big Bang, during the Big Bang nucleosynthesis, they decouple from the thermal equilibrium ("freeze-out") at a temperature of 1 MeV $\approx 10^{10}$ K, as the Hubble parameter exceeds the weak interaction rate of neutrinos [GL18, Zub20]. With a density of $n_{\mathrm{C}\nu\mathrm{B}} = 336\ {}^{1}/_{\mathrm{cm}^3}$ [Zub20] today and non-vanishing mass, these relic neutrinos contribute significantly to the mass density in our universe. The imprint of massive neutrinos on large scale structures shows up in anisotropies of the cosmic microwave background radiation, weak gravitational lensing and the Lyman-α forest [GL18]. Such observations are usually sensitive to the sum

$$m_\nu = \sum_i m_i \tag{2.16}$$

of all three masses can be extracted, allowing to set a constraint on the neutrino mass. For example, a strong upper limit of $m_\nu < 0.12$ eV (95 % C.L.) is set by the data acquired by the Planck satellite [A⁺20a].
Supernovae like SN 1987A are core collapse or type II supernovae, which irradiate around 99 % of their energy (~10^{46} J) as neutrinos. Neutrinos experience dispersion during their propagation over the distance L in space, depending on their energy E and mass m_ν, resulting in a time of flight delay of

$$\Delta t \approx \frac{m_\nu^2 L}{2}\left(\frac{1}{E_2^2} - \frac{1}{E_1^2}\right) + \Delta t_0 \tag{2.17}$$

between two neutrinos with energies E_1 (first) and E_2 (second neutrino), where Δt_0 accounts for the initial time difference of creation in the supernova [Zub20]. As a consequence of SN 1987A, roughly 10^{28} neutrinos created over a period of some seconds traverse earth, some few of them

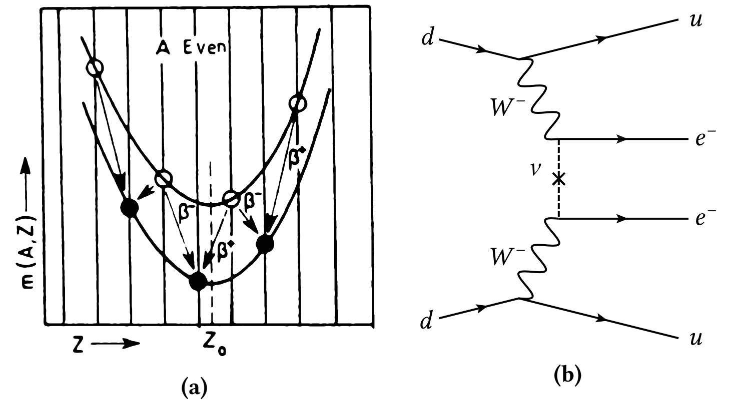

Figure 2.2.: Neutrinoless double beta decay: Figure a (from [Zub20]): Split mass parabolas with respect to atomic number Z of nuclei with even mass number A. Upper parabola of odd-odd, lower of even-even nuclei. Arrows indicate single beta decays. Figure b: Feynman diagram of $0\nu\beta\beta$. The decay of the d quarks is mediated by two W bosons. No neutrino is emitted.

interacting with neutrino observatory detectors (Kamiokande-II, IMB and Baksan). More than 20 neutrinos are detected and associated with the supernova [Zub20, LL02]. An analysis of the measurements is provided in [LL02], where a value of $m_{\bar{\nu}_e} < 5.7\,\mathrm{eV}$ (95 % C.L.) is set as constraint on the mass.
Of course, these approaches strongly depend on the assumed models. Making statements on CνB neutrinos and the cosmological evolution and structure requires a cosmological model, like for example the standard cosmological ΛCDM model. Although the ΛCDM model is very successful, it faces a number of challenges, as [PS21] summarizes. For the astrophysical supernova neutrinos, it is clear that assumed mechanisms of supernovae are a source of uncertainty.

Another approach, comprising large time scales rather than distances, is the neutrinoless double beta decay ($0\nu\beta\beta$). Figure 2.2 illustrates double beta decay. The energetic situation is plotted in figure 2.2a: isotopes with even mass numbers A occur in odd-odd and even-even configurations. Due to the pairing energy, the mass parabolas (over atomic number Z) are split for these configurations. Close to the minimum, if the daughter nucleus' binding energy is larger than the energy of the mother nucleus (upper parabola, odd-odd), only another subsequent beta decay will ensure that the process is energetically allowed. An even-even isotope will transmutate directly to the lower even-even configuration in that case. A Feynman diagram of this interaction is provided in figure 2.2b. Throughout transmutation, two beta quanta (e^-) are emitted as well as two neutrinos, according to lepton number conservation.
Mediated by the weak interaction, this second order process is rare and marked by very long half-lifes of ~10^{20} a. While ordinary double beta decay with emission of two neutrinos ($2\nu\beta\beta$) is already observed directly in the laboratory in ^{82}Se during the 1980s [EHM87], $0\nu\beta\beta$ is not until today. Isotopes like ^{76}Ge, ^{136}Xe or ^{100}Mo are common candidates used in experiments. As formerly expected for beta decay (see sec. 2.1), the spectrum would indeed show a narrow energy distribution at the Q value instead of the continuous spectrum of $2\nu\beta\beta$. However, if no neutrinos are emitted, the lepton number conservation is violated and the neutrino has to be a Majorana particle, i.e., a self-conjugate particle (eq. 2.8, remark: Majorana phases α_1 and α_2). The half-life $T^{0\nu}_{\beta\beta}$, which is related to the effective Majorana mass $\langle m_{\beta\beta} \rangle$, is derived with respect to the phase

space factor $G^{0\nu}$ and nuclear matrix element $M^{0\nu}$:

$$T^{0\nu}_{\beta\beta} = \frac{1}{G^{0\nu}\left|M^{0\nu}\right|^2 \langle m_{\beta\beta}\rangle^2}. \tag{2.18}$$

The electronic components of the PMNS matrix contribute in the effective Majorana mass $\langle m_{\beta\beta}\rangle$. It is obtained by coherent summation as

$$\langle m_{\beta\beta}\rangle = \left|\sum_j U^2_{ej} m_j\right|, \tag{2.19}$$

wherein the physical Majorana phases appear explicitly [Zub20].
Although no evidence is provided for $0\nu\beta\beta$ so far, there are different experiments to further constrain the neutrino mass, like for example MAJORANA [A+19b] and GERDA. Corresponding to the obtained half-life limit of $T^{0\nu}_{\beta\beta} > 1.8 \times 10^{26}$ a (90 % C.L.), an upper limit of $\langle m_{\beta\beta}\rangle < 0.07$ eV – 0.18 eV (90 % C.L.) on the neutrino mass is set by GERDA [A+20b]. The collaborations of both experiments merged to build the next generation experiment LEGEND [A+17, A+21a]. The model-dependence of $0\nu\beta\beta$-based results is given by the uncertainty in the Majorana phases and their effect, by the calculation of matrix elements and by potentially many BSM contributions to the decay [PR15]. Not only can the neutrino mass be constrained by $0\nu\beta\beta$, but is it a sensitive probe to lepton number violation and to answer the question, whether neutrinos are Majorana or Dirac particles.

Spectroscopy of beta decay, once driving the discovery of the neutrino (sec. 2.1), is a model-independent approach to determine the neutrino mass. The beta decay of a neutron is called β^- decay and follows

$$n \longrightarrow p + e^- + \bar{\nu}_e, \tag{2.20}$$

corresponding to an isotope ${}^A_Z X$ transmutating to ${}_{Z+1}^{\ \ A}Y$, as the neutron is usually bound within an atomic nucleus. The reactions' Q value of energy is distributed among the products. Due to the large mass of the nucleus, its recoil energy is almost negligible. From energy-conserving three-body decay kinematics, the beta spectrum can be derived. The neutrino mass affects the entire spectrum, but the imprint becomes most noticeable near the endpoint, as illustrated by Fermi in the 1930s already [Fer34]. The differential beta spectrum of molecular tritium is shown in figure 2.3 from [K+19]. Figure 2.3a displays the full energy range, whereas the endpoint region around E_0 is shown in detail in 2.3b. Apart from an overall deformation compared to the limit of $m_{\bar{\nu}_e} = 0$, the endpoint is shifted proportionally to the neutrino mass, as at least the rest energy has to be provided. This effect is demonstrated in figure 2.3b. Accordingly, the observable for beta spectroscopy is

$$m^2_\nu = \sum_j \left|U_{ej}\right|^2 m^2_j, \tag{2.21}$$

the effective electron anti-neutrino mass [K+19]. Different from equation 2.19, this is the incoherent sum of electronic mass contributions.
Consequently, beta spectroscopy provides an approach to directly access the neutrino mass. It comes along with the advantage of model-independence. In principle, numerous beta isotopes exist and could be investigated, but many challenges have to be overcome to constrain or measure the neutrino mass on a level comparable to the preceding methods. One challenge is, for example, that the neutrino mass is extremely small compared to common Q values of beta decays, ranging

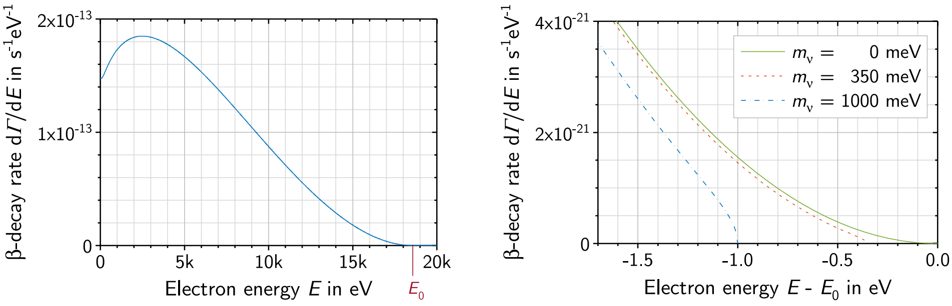

(a) **(b)**

Figure 2.3.: Differential beta spectrum of molecular tritium (from [K⁺19]): Figure a: Full spectrum with E_0 = 18.574 keV. Decay rate for single nucleus. Figure b: Endpoint region of spectrum from fig. a for different neutrino masses m_ν.

from a few kilo- to some megaelectronvolts [Int22]. This is also illustrated by figure 2.3.

Some decays come along with advantageously low Q values. Two isotopes actually used in calorimetric experiments for spectroscopy of decays are ^{187}Re and ^{163}Ho. While the former undergoes beta decay to ^{187}Os with Q = 2.47 keV, the latter decays via electron capture (EC), transmutating to ^{163}Dy. Throughout EC, no electron is emitted by the atom and a two-body decay (^{187}Os, ν_e) with Q = 2.83 keV takes place. As cryogenic calorimeters, both elements are used as source and detector at once, for example in the MARE (^{187}Re and ^{163}Ho) [F⁺15] and the ECHo experiment (^{163}Ho) [G⁺17]. The released energy (minus neutrino energy) is deposited in the calorimeter and induces a measurable rise in temperature. Due to very long half-lifes of $T_{1/2}^{^{187}\mathrm{Re}} \approx 4.1 \times 10^{10}$ a and $T_{1/2}^{^{163}\mathrm{Ho}} \approx 4.6 \times 10^{3}$ a, large amounts of the materials are required. While MARE aims towards a sensitivity of a few keV [F⁺15], sub-eV sensitivity is pursued with ECHo [G⁺17].

Molecular tritium ($^3H_2$ or T_2) decays with a comparably low endpoint energy E_0 of 18.574 keV [K⁺19]. Similar to equation 2.20, the nuclear reaction reads

$$T_2 \longrightarrow {}^3\mathrm{HeT}^+ + e^- + \bar{\nu}_e \tag{2.22}$$

The endpoint is separated slightly (some eV) from the Q value of the decay, since nuclear recoil, molecular final state and the neutrino take up a share of released energy. The half-life of tritium $T_{1/2}^{\mathrm{T}}$ = 12.33 a is short, making high rates feasible. Also, regarding Coulomb interactions, the atomic hull is a rather uncomplicated system, as $Z = 1$. This lowest possible Z is also favorable to reduce inelastic scattering within the gaseous tritium. The presence as gas makes the usage of tritium beneficial because energy losses related to solids do not occur. Spectroscopy of the tritium beta spectrum is achieved in two different ways, by cyclotron radiation emission spectroscopy (CRES) and with electromagnetic filters.

Project 8 [E⁺22] pursues the former technique and already performed first neutrino mass scans using CRES. Different from equation 2.22, atomic tritium T is used. The energy spectrum is extracted by measuring the cyclotron radiation of electrons which are confined in a strong uniform magnetic field. For an electron's gyro- or cyclotron frequency f_g, the relationship with applied magnetic field of strength B and the energy E of the electron is

$$2\pi f_g = 2\pi \frac{f_{g,0}}{\gamma} = \frac{eB}{m_e + E}, \tag{2.23}$$

where γ is the Lorentz factor ($f_{g,0}$ is the electron's cyclotron frequency in the rest frame with $f_{g,0}/B \approx 28\,\mathrm{GHz/T}$ [Z⁺20]) and e and m_e are charge and mass of the electron [E⁺22]. It is aimed towards

a sensitivity of $m_\nu \leq 40\,\text{meV}$. As atomic tritium is used in combination with CRES, remaining systematic uncertainties accompanying molecular tritium, namely the distribution of final states (final state distribution FSD) populated by the decay products of T_2, are wiped out. [E⁺22]
Another approach is provided by experiments based on electrostatic filtering. In principle, an integral spectrum is obtained by applying a variable electrostatic retarding potential to decay electrons, acting as a high-pass filter. To ensure a good energy resolution $\Delta E/E$ for electrons with initially unoriented momenta, the electrostatic filter is combined with magnetic adiabatic collimation. This type of configuration is called MAC-E filter. Former MAC-E filter-based experiments for tritium beta spectroscopy are Mainz and Troitsk, constraining the neutrino mass to $m_\nu \leq 2.3\,\text{eV}$ (95 % C.L.) [K⁺05] and $m_\nu < 2.05\,\text{eV}$ (95 % C.L.) [A⁺11].
Currently, the most stringent constraints on the neutrino mass by a model-independent and direct method is set by the KATRIN experiment, the successor of Mainz and Troitsk. The latest limit obtained from combination the first two measurement campaigns an upper limit of $m_\nu < 0.75\,\text{eV}$ (90 % C.L.) is found [A⁺22]. The following chapter 3 describes the KATRIN experiment and aspects of the experimental technique in detail.

3. The KATRIN Experiment

The Karlsruhe Tritium Neutrino Experiment (KATRIN) is a direct and model-independent approach to probe the effective mass of the electron anti-neutrino $\bar{\nu}_e$ by MAC-E filter-based tritium beta spectroscopy (sec. 2.3). It is designed to achieve a sensitivity of 0.2 eV at 90 % C.L. after 1000 days of data-taking [A⁺21c]. Sub-electronvolt sensitivity is already achieved with KATRIN after 50 days, as the latest limit provided by the experiment is $m_\nu < 0.75\,\mathrm{eV}$ (90 % C.L.) [A⁺22], which surpasses Mainz and Troitsk by a factor of more than two [K⁺05, A⁺11].
An overview of the experiment, the measurement principle and the data analysis is given in section 3.1. Section 3.2 is a description of the experimental setup. This is followed by an overview of the background sources in the experiment in section 3.3.

3.1. Basics of the KATRIN Experiment

For an overview, KATRIN is illustrated in figure 3.1. The displayed setup has an overall length of roughly 70 m. In the left, within the windowless gaseous tritium source (WGTS), about 10^{11} Bq of beta decay electrons are emitted isotropically. They are confined to the magnetic field of the beamline. The magnetic field $\vec{B}$ is provided by solenoids (super- and normal conducting) and extends over the entire length of the experiment with varying strength, allowing for adiabatic guiding of the electrons either downstream, that means towards the focal plane detector (FPD) on the right, or upstream, towards the rear wall (RW). The general principle is to impose a retarding potential U_0, acting as an electrostatic high-pass filter, on the electrons with charge $q = -e$ and measure the remaining rate at the FPD, which would be the integral spectral fraction with $E > qU_0$. In figure 3.1, U_i corresponds to a certain setpoint of U_0. The plane of maximum potential (absolute value) is the analyzing plane (AP), since it represents the highest potential barrier. The blue plane in the main spectrometer vessel's center (fig. 3.1) represents the AP. In general, electrons do not move parallel to the electric field lines, resulting in a bad energy resolution $\Delta E/E$ if no countermeasures are taken, as only a fraction of E can contribute to surpass the threshold qU_0 and $E > qU_0$ is not a sufficient criterion, consequently. [A⁺21c]
An electron's direction depends on the electrons' initial pitch angle θ in the source, of course. The definition of θ is indicated in the bottom of figure 3.1, where the relation to the momentum $\vec{p}$ is shown. Also, the global z-axis of the experiment is specified (dashed gray arrow). It has to be mentioned that usually the angle $\theta = \angle(\vec{p}, \vec{B})$ is referred to as pitch angle [A⁺21c], while $\vec{z} \| \vec{B}$ is not generally satisfied. To allow for differentiation, the angle $\angle(\vec{p}, \vec{z})$ will be called polar angle and labelled θ_z.
The electrons are guided adiabatically to provide full energy conservation. To ensure adiabaticity, sufficiently low magnetic gradients are required. As Lorentz force acts on charged particles in magnetic fields, electrons propagate in a cyclotron motion [A⁺21c]. Following the two components of motion, the energy E can be divided into two components, a transverse component $E_\perp$ and a

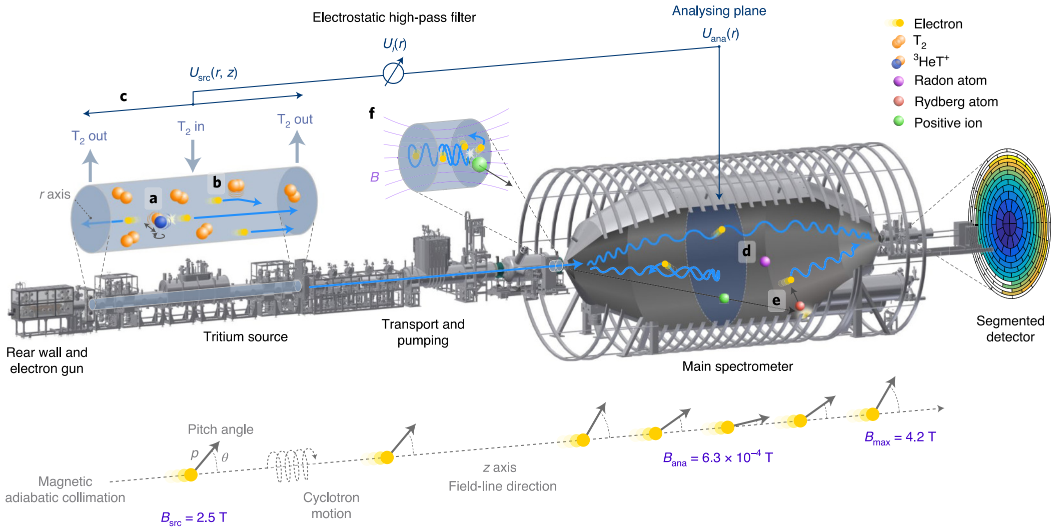

Figure 3.1.: Illustration of the KATRIN experiment (from [A$^+$22]): The main components are displayed. Electron propagation from molecular tritium decay, followed by magnetic guiding, MAC-E filtering and eventual detection on the FPD, can be retraced. Some further processes and details are also indicated.

parallel or longitudinal one $E_\parallel$, according to the pitch angle θ with respect to $\vec{B}$. Conservation of energy reads

$$E = E\sin^2(\theta) + E\cos^2(\theta) =: E_\perp + E_\parallel = \text{const.} \tag{3.1}$$

then. The orbital magnetic momentum μ can be derived from the angular momentum $\vec{\ell}$ of the cyclotron motion:

$$\mu = |\vec{\mu}| = \frac{e}{2m_e}|\vec{\ell}| = \frac{E_\perp}{|\vec{B}|} = \text{const.} \tag{3.2}$$

in non-relativistic approximation [A$^+$21c] $\gamma \approx 1$ (actually $\gamma\mu$ is conserved [Frä10, F$^+$17b]). This means that the ratio of transverse energy $E_\perp$ and the local strength $B = |\vec{B}|$ of the magnetic field is conserved.
Along the source and transport section (STS), the tritium flow rate is reduced by 14 orders of magnitude to prevent those from propagating into the spectrometer and detector section (SDS), where a ultra-high vacuum (UHV) of ~10^{-11} mbar has to be maintained [A$^+$21c]. This section fulfills the spectrometric task of the experiment, making use of the MAC-E filter principle.

MAC-E Filter

The electric field $\vec{E}$ resulting from the vessel potential of the spectrometer can only act on the longitudinal component of the electrons momentum, corresponding to $E_\parallel$ in equation 3.1. Thus, the filtering criterion has to be $E_\parallel > qU_0$ to account for the electrons' directions. Purpose of the MAC-E filter is spectroscopy with respect to the full energy E. Consequently, the magnetic field has to evolve in a way that transfers an electron's – in the ideal case – entire energy E into longitudinal energy $E_\parallel$. Equation 3.2 reveals a way to realize this: a reduction of B causes the transverse component $E_\perp$ to decrease equally. Energy conservation in equation 3.1 is responsible for the corresponding energy transfer into the longitudinal component.

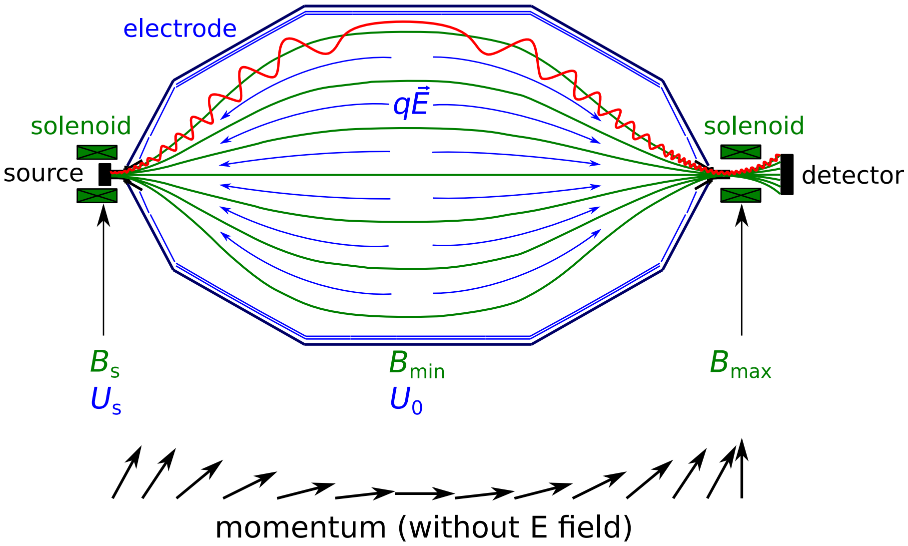

Figure 3.2.: MAC-E filter (from [Wan13]): In this cross-section of the main spectrometer, the electric components are drawn in blue, magnetic components in green. Blue arrows indicate the electrostatic force due to the potential gradient between U_0 and U_s ($|U_\mathrm{s}| < |U_0|$). The green magnetic field lines are pinched by solenoids outside of the spectrometer. The trajectory of a transmitted electron with $E_\| > qU_0$ is also drawn (red). The corresponding evolution of momentum (neglecting the effect of $\vec{E}$) is indicated by arrows (bottom).

A sketch of the situation in KATRIN's main spectrometer (MS) is shown in figure 3.2. The arrows below the spectrometer cross-section indicate the evolution of momentum (neglecting the electrostatic force $q\vec{E}$) and reveal the effect of magnetic adiabatic collimation (MAC), i.e., the adiabatic transfer of the particle's energy into longitudinal energy. As the energy selection is achieved with an electrostatic (E) filter, MAC obtains the suffix -E.

In the experiment, the magnetic field (by design) is drastically reduced from $B_\mathrm{s} = 3.6\,\mathrm{T}$ or $B_\mathrm{max} = 6\,\mathrm{T}$ to B_min of only a few Gauss ($\mathcal{O}(0.1\,\mathrm{mT})$) in the AP (at U_0) [A+21c]. The conservation of magnetic flux $\Phi = \int_A \vec{B}(\vec{r}) \cdot \mathrm{d}\vec{A} \approx B \cdot A$ (reference area A), which is designed to be at $\Phi = 191\,\mathrm{T\,cm^2}$ [A+21c], requires a strong increase of the fluxtube diameter along the beamline.

A vanishing magnetic field $B_\mathrm{min} = 0$ at the AP can not be realized. Therefore, it is not possible to achieve $E_\| = E$. Instead, the MAC-E filter has a finite filter width ΔE, which follows from equation 3.2 and the extrema of the involved quantities. It is

$$\Delta E = \frac{B_\mathrm{min}}{B_\mathrm{max}}\,E. \tag{3.3}$$

The normalized width $^{\Delta E}/_{E}$ is the energy resolution of the MAC-E filter. Similarly, the relation of the transverse energies between an initial point i and final point f of consideration is $^{E_\mathrm{f}}/_{E_\mathrm{i}} = {}^{B_\mathrm{f}}/_{B_\mathrm{i}}$. Both a transmitted and a reflected ($E < qU_0$) electron from the STS on the left can be seen in figure 3.1. A feature of the MAC-E configuration is, that reflection of electrons can not only occur due to low energy. An electron with initial pitch angle θ_0 at a starting point $\vec{r}_0$ will be guided adiabatically to a point $\vec{r}$, where the pitch angle is

$$\theta(\vec{r}) = \arcsin\left(\sqrt{\frac{E(\vec{r}_0)}{E(\vec{r})}\,\frac{|\vec{B}(\vec{r})|}{|\vec{B}(\vec{r}_0)|}}\,\sin(\theta_0)\right). \tag{3.4}$$

This relation is obtained by insertion of the definition of $E_\perp = E_\perp(\vec{r})$ from equation 3.1 into the adiadbaticity relation 3.2. It follows, that the pitch angle can exceed 90°, corresponding to so-called

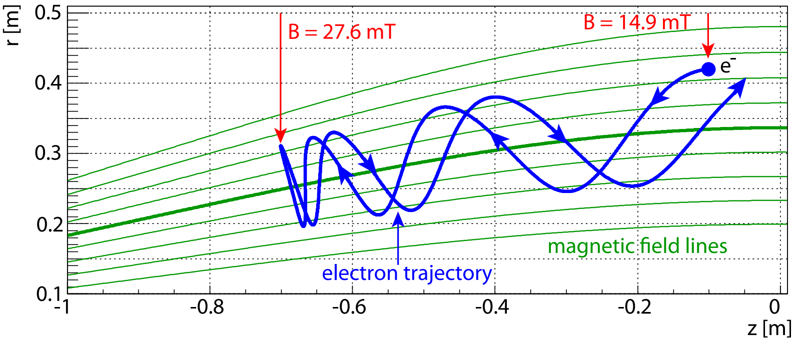

Figure 3.3.: Magnetic mirror effect from [Frä10]: The trajectory of an electron with an initial pitch angle $\theta = 130^\circ$ and an energy of $E = 200\,\mathrm{keV}$ in the pre-spectrometer is shown. It is reflected as the magnetic field increases. The coordinate system (radius r, location on z-axis) corresponds to the pre-spectrometer coordinates. Initial position: $(z, r) = (-0.1, 0.42)\,\mathrm{m}$.

mirroring of the electron, as the orientation of its momentum flips. This happens because of magnetic field gradients in the configuration. To obtain a limit θ_max for θ_0, above which a beta electron will definitely be reflected, $|\vec{B}(\vec{r})| = B_\mathrm{max}$, $|\vec{B}(\vec{r}_0)| = B_\mathrm{s}$, $E(\vec{r}_{B_\mathrm{max}}) = E(\vec{r}_{B_\mathrm{s}})$ and $\theta(\vec{r}) = 90^\circ$ are set. Solving for θ_0 yields the acceptance angle

$$\theta_\mathrm{max} = \arcsin\left(\sqrt{\frac{B_\mathrm{s}}{B_\mathrm{max}}}\right) = 50.77^\circ \tag{3.5}$$

of the configuration with the design values from above or with the standard values [A⁺21c], too ($B_\mathrm{s}/B_\mathrm{max} = 0.6$). The mirror effect is demonstrated in figure 3.3, where an electron is reflected in the region of narrowing magnetic field lines in the pre-spectrometer. Mirroring downstream of the AP can reject formerly accepted electrons with $E_\parallel > qU_0$. This has to be taken into account when making predictions on the signal rate based on the source activity.

Inference of the Neutrino Mass

An integral tritium beta spectrum is obtained from neutrino mass scans, covering multiple setpoints of the retarding potential. These measurements are organized in campaigns, the KATRIN neutrino mass campaigns (KNMs). The corresponding rate for each potential results from the absolute number of counts and the measuring time at the setpoint. A beta spectrum close to the endpoint E_0 from simulated toy data is shown in figure 3.4. In the middle panel, a reduction of the statistical error on the measured rates follows from longer measuring times t (distribution in lower panel). Since a Poisson process describes the underlying statistics of the count number N (and rate $R = \dot{N}$), the uncertainty scales with $1/\sqrt{N} \propto 1/\sqrt{t}$ [Z⁺20].
Actually, the effective electron anti-neutrino neutrino mass m_ν^2 (eq. 2.21) is the observable in KATRIN, occuring as a fit parameter of the theoretical prediction for the count rate of the beta spectrum in the experiment. The following is based on [A⁺21b]. For the expected rate at a retarding voltage of U_0, the expression

$$R_\mathrm{theo}(qU_0) = A_\mathrm{sig} \int_{qU_0}^{E_0} \frac{\mathrm{d}R}{\mathrm{d}E}(E; E_0, m_\nu^2)\, f(E - qU_0)\,\mathrm{d}E + R_\mathrm{bg}(A_\mathrm{bg}) \tag{3.6}$$

is established. $\mathrm{d}R/\mathrm{d}E(E)$ is the differential tritium beta spectrum, $f(E - qU_0)$ the instrumental response function, depending on the electrons' surplus energy, and R_bg the background rate. This representation of R_theo reveals three further parameters that are required for the fit: the signal

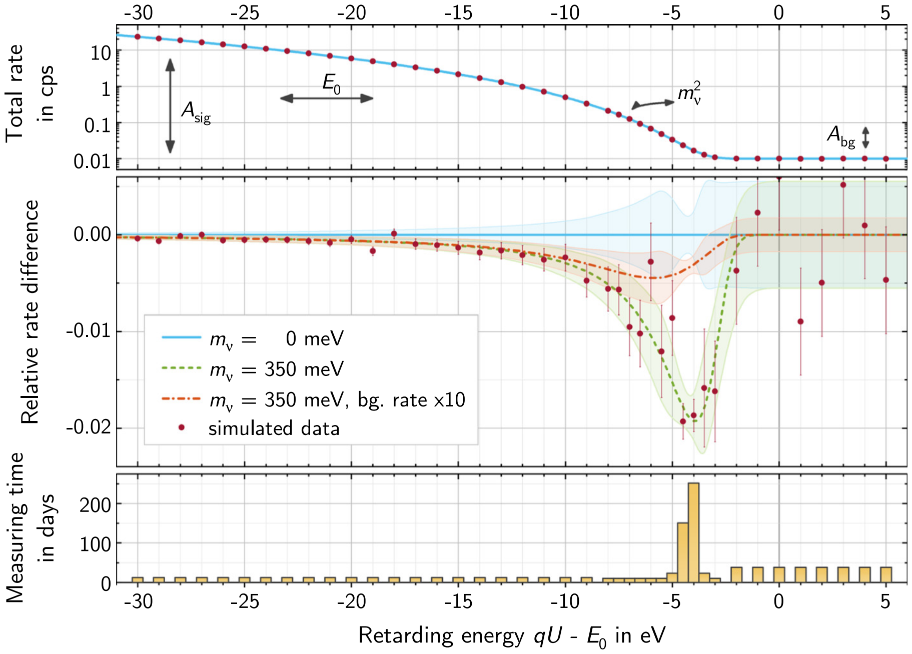

Figure 3.4.: Simulated KATRIN measurement results of the integral tritium beta spectrum (from [K⁺19]): The toy data result from a simulation with $m_\nu = 350\,\mathrm{meV}$. In the top panel, the integral spectrum close to the endpoint E_0 is displayed which is obtained with the measuring time distribution in the bottom panel. Longer measuring times significantly reduce the statistical error bars in the middle panel, where the relative rate difference of calculated spectra for $m_\nu = 350\,\mathrm{meV}$ with different background rates R_{bg} of nominal 10 mcps (green dashed) and elevated 100 mcps (orange dash-dotted) from the $m_\nu = 0$ case are shown. The black arrows in the top panel indicate how the different quantities affect the spectrum. A_{sig} and A_{bg} are the signal and background amplitudes.

(background) amplitude A_{sig} (A_{bg}) and the tritium endpoint E_0 [A⁺21b]. For each of the four parameters in total, the implications for the spectral shape are indicated in figure 3.4. Each data point corresponds to a retarding energy qU_i and rate $R_{\mathrm{theo}}(qU_i) =: R_i$ according to equation 3.6. Properties like, for example, the filter width ΔE (eq. 3.3) and the acceptance angle θ_{max} (eq. 3.5) are of instrumental origin and taken into account by means of the response function $f(E - qU_0)$.

The minimized quantity for parameter inference is the negative logarithm $-2\ln(\mathcal{L})$ of the Poisson likelihood function $\mathcal{L}$. It is minimized for the set of measured rates R_i with respect to the model that relies upon 3.6 with the mentioned fit parameters but also includes systematic nuisance parameters. Because of high statistics, the Poisson likelihood can be replaced by the χ^2 estimator, including the covariance matrix C with both correlated and uncorrelated statistic and systematic uncertainties. The parameters are obtained from minimizing χ^2 to the best fit whereas their uncertainties can be inferred from the χ^2 function's profile around the minimum. For further details on the analysis methods, it should be referred to [A⁺21b].

From equation 3.6 and figure 3.4 it follows that the background plays a fundamental role for the inferred neutrino mass. An increasing signal-to-background ratio (SBR) results in a smaller relative rate difference of $R_{\mathrm{theo}}(m_\nu^2 = 0)$ and $R_{\mathrm{theo}}(m_\nu^2 > 0)$. In consequence, even in the range of maximum distortion (middle panel in fig. 3.4) at ~5 eV below the endpoint the distortion is much weaker than in the low background case because of the constant rate contribution. This reduces the neutrino mass sensitivity.

3.2. Experimental Setup

The principle of the KATRIN experiment is explained in the previous section 3.1. In the following, the focus will be on instrumental aspects of KATRIN. Therefore, this section concerns experimental components that are displayed in figure 3.1. The explanations are based on [A+21c].

Source and Transport Section

The WGTS with a total length of 10 m gives rise to 10^{11} beta electrons of the decaying molecular tritium and represents the first part of the source and transport section (STS). It is situated on the left in figure 3.1. To ensure a high rate stability, the throughput of gas, which is injected in the middle of the WGTS, is regulated precisely. In addition, two turbo-molecular pumps are installed at both ends of the source to achieve the required stability of 0.1 % per hour by constant pumping. Consequently, a constant column density $\rho d = 5 \times 10^{15}\ {}^{1}/_{\mathrm{cm}^2}$ of tritium molecules is provided. The gas composition is monitored with the laser Raman spectroscopy system (LARA). In addition, the source tritium activity is continuously monitored with the bate-induced x-ray spectroscopy system (BIXS). A neon cooling system keeps the temperature of the beamtube at 30 K. Electrons from decays during the diffusion of tritium molecules towards the pumps are already confined in the prevalent source magnetic field B_s of up to 3.6 T.

The electrons that are emitted into downstream direction are adiabatically guided along the transport section. It is equipped with pumping systems to remove remaining molecules, atoms and ions from the beamtube towards the SDS. This is necessary to prevent additional background from being induced by these particles. The first station for this objective is the differential pumping section (DPS). It consists of five beam tube elements, each located in the bore of a superconducting magnet, that are tilted by 20° with respect to each other. Hence, a direct line of sight along the beamtube is blocked to prevent the beaming effect. Six turbo-molecular pumps in total, located at the elements' ends, reduce the flow by differential pumping. The pumping ports are located outside the fluxtube and could thus not remove magnetically guided tritium ions efficiently. Dipole and ring electrodes line the beamtube to remove them nevertheless with electric fields. This way, the flow is reduced by seven orders of magnitude.

The cryogenic pumping section (CPS) is the last component of the STS. Because turbo-molecular pumps can not reduce the flow further, a sorption pump is chosen for this stage. Within the CPS, the inner beamtube surface covered with thin gold-plated fins, onto which a thin layer of argon frost is condensed. During operation, the CPS beamtube is kept at 3 K. Tritium-containing molecules are efficiently adsorbed by the argon layer, which retents the molecules over long time-scales. Moreover, the beamtube segments are again arranged as a chicane. Altogether, the flow is reduced by another seven magnitudes to achieve the required reduction factor of at least 10^{14} in total.

Through a pump port at the downstream end of the CPS, the forward beam monitor (FBM) can be inserted. With this device, the relative beta electron flux in the downstream direction can be monitored. For this purpose, it consists of two PIN diodes, allowing for the measurement with a precision of 0.1 % in less than 60 s.

Spectrometer and Detector Section

Two spectrometers working according to the MAC-E principle (sec. 3.1) – the pre-spectrometer (PS) and the MS – and the FPD represent the main components of the spectrometer and detector section (SDS). The SDS is responsible for the actual beta spectroscopy. In figure 3.5, these components are depicted.

Electrons from the CPS are magnetically guided to the PS at first. Two solenoids at both ends of the vessel, the PS magnets (PS1 and PS2), constrict the guiding field lines. In between, the fluxtube widens as the potential reaches a local minimum to ensure MAC-E properties. Main purpose of the PS is to reduce the flux of high rates in the low energy parts ($E < 18\,\mathrm{keV}$) of the beta spectrum into the MS.

The remaining fraction of beta electrons is guided from the PS1 into the MS. An undisturbed passage for beta electrons would already be possible at 10^{-7} mbar, but background production due to residual gas can only be suppressed effectively in the few 10^{-11} mbar regime. Hence, both spectrometers at these UHV conditions. To achieve the required energy resolution (eq. 3.3) at conserved magnetic flux, the radius at the MS center has to be correspondingly large. A diameter of 9.8 m is therefore chosen. With a length of 23.2 m and a volume of $1240\,\mathrm{m}^3$, the MS is the world's largest UHV tank. To maintain these conditions, the spectrometer is equipped with turbomolecular and non-evaporable getter (NEG) pumps, located in pump ports with a diameter of 1.7 m. For the retention of radon, emanating from the NEG material, liquid nitrogen (LN_2)-cooled copper baffles separate the inner volume and the pumps (see sec. 3.3.2). In addition to the vessel potential, the inner wire electrode system (IE) (indicated by dashed lines in fig. 3.5) is used to fine tune the shape of the electric field and prevents propagation of electrons from the vessel walls into the inner volume. The prevalent axial magnetic fields of the air coil system have the same effect, but main purpose of the air coil system is of course to tune the magnetic field of the MS. It consists of two sub-systems, the low-field correction system (LFCS) and the earth magnetic field compensation system (EMCS). The 12.6 m diameter solenoids of the air coils around the MS can be seen in figure 3.1. To obtain certain magnetic field configurations, the current of each LFCS coil can be set individually. Because the minimum magnetic field of a few Gauss is on the same level as the earth magnetic field, the EMCS is installed for compensation of the local earth magnetic field with two sets of dipole coils around the x- and y-axes of the MS. With both systems in combination, precise fine tuning of the fluxtube and AP is achieved.

Transmitted electrons with $E > qU_0$ are accelerated to their source energy as they are guided through the pinch magnet (PCH in fig. 3.5) into the detector section. The FPD is situated in the bore of the last superconducting solenoid of the beamline, the detector magnet (DET). Together with the pinch magnet, it ensures adiabatic guiding of the electrons from the spectrometer to the FPD wafer. The post acceleration electrode (PAE) is also located in the detector magnet and accelerates the beta electrons by typically 10 keV. This reduces the backscattering probability at the FPD surface and boosts them into a region of lower intrinsic detector background.

A monolithic multi-pixel array is the central piece of the FPD. On a single silicon wafer with a diameter of 125 mm, 148 positive intrinsic negative (PIN) diodes are arranged in a pattern of 13 concentric rings, accounting for a sensitive area with a diameter of 90 mm. The layout is shown in figure 3.9. Each pixel has a surface area of $44\,\mathrm{mm}^2$, onto which the fluxtube is mapped. An overvoltage of 120 V is applied for operation. The beta electron signal is processed by readout electronics and the KATRIN data acquisition (DAQ) system.

3.3. Background in the Experiment

Figure 3.4 illustrates the relevance of the background in the KATRIN experiment which is also addressed in section 3.1. Several components of background are known and summarized in figure 3.5. On the one hand, intrinsic detector background occurs, and on the other hand, background electrons from the spectrometers mingle with the beta electrons, contributing to the total rate. When entering the fluxtube or originating within, they are guided onto the FPD, given they are located downstream the AP or sufficiently energetic. Therefore, preventing background electrons from entering the fluxtube is an obvious and effective measure of background mitigation. Due to

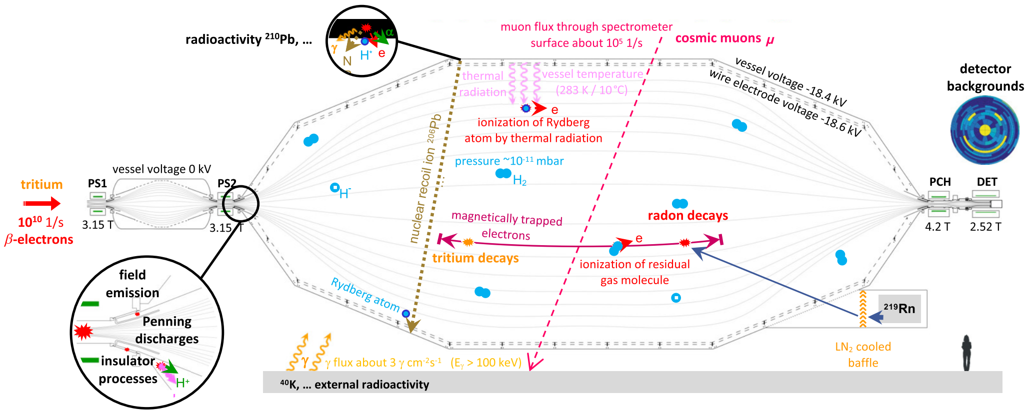

Figure 3.5.: Overview of the background components in the KATRIN experiment (from [Frä22]).

the similar design of the experiments, expertise from Mainz and Troitsk is applied in KATRIN, allowing for predictions regarding background contributions by various processes. This leads to the design value of a background rate $R_{\text{bg}} = 10$ mcps in the region of interest (ROI). With an actual background rate of ~300 mcps, the current level differs by more than an order of magnitude from this value [A+21c]. Thus, efforts to investigate, mitigate and discriminate background mechanisms are ongoing, since countermeasures are required to improve sensitivity towards the design value. While multiple sources of background are well understood, some components are not yet. In the following, components of the spectrometer background will be presented. Of course, energetic particles like cosmic-ray muons can release electrons from experimental components or interact with the detector. Apart from that, background electrons originate from internal sources, like for example Penning traps or stored electrons, both being a characteristic feature of MAC-E filter setups. In contrast, natural radioactivity potentially affects every comparable setup: both external and internal usual concentrations or traces of radioactive nuclides can contribute to the background (fig. 3.5). Of the first, gamma quanta easily penetrate the spectrometer hull, probably causing electrons that might enter the vessel, whereas the latter induces a much broader spectrum of secondaries, which can in turn cause electrons via different mechanisms.

3.3.1. Muons and Trapping

Cosmic-Ray Muons

On the surface of earth, the flux of muons, mostly caused by primary cosmic rays in the upper atmosphere, is on a level of ~10^4 $^1/_{\text{m}^2\text{min}}$ [P+16]. With energies up to some teraelectronvolts [Gri01], these cosmic-ray muons will interact with the spectrometer components, especially large-scaled structures like spectrometer wall and electrode system. Due to the MS's surface area of 690 m^2 [A+21c] being exposed to the flux, a secondary electron rate of 10^5 $^1/_\text{s}$ is expected from the measured rate at the Mainz experiment [Lei14].
In the spectrometer hall, eight modules (2.05 m^2 each) of BC-412 scintillator with a light yield of $Y = 8500$ $^1/_\text{MeV}$ are arranged in three towers around the MS and one more module (0.3 m^2) is placed above the vessel, each of them equipped with four (two in case of the small module) PMTs and wrapped. This setup works sufficiently as muon detector system, as the scintillation light caused by incident muons is collected and the rate is concluded. To validate muon-induced background, correlation measurements are carried out, where the FPD rate and the measured cosmic-ray muon rate are correlated. Guiding electrons from the spectrometer walls and the IE towards the FPD by application of an asymmetric LFCS setting yields a correlation coefficient of 0.70 ± 0.06 but

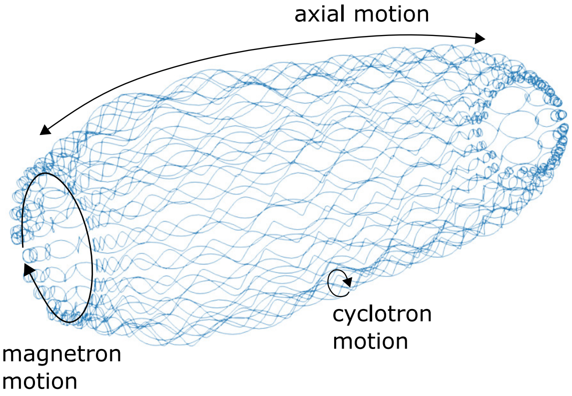

Figure 3.6.: Stored electron (from [Sch20]): The electron oscillates axially in the MS between narrowing fluxtube regions. The typical cyclotron motion (eq. 2.23) is superimposed by a magnetron drift around the global z-axis.

shows that only (12.3 ± 1.2) % of the background is actually muon-induced in the ROI [A⁺19a]. In contrast, the muon-induced fraction is (88 ± 5) % in the high energy region [Lin15].

Apart from this validation of the muon-induced mechanism, when moving to nominal LFCS settings, the correlation vanishes. An upper limit of 16.6 % (90 % C.L.) is established for the muon-induced fraction of the background. Summarizing, the magnetic shielding of the fluxtube is very effective for mitigation of muon-induced background, hence being no significant concern. [A⁺19a]

Stored Electrons

The possibility of mirroring in the spectrometer setup is introduced in section 3.1 and illustrated in figure 3.3. If electrons start their propagation in the fluxtube within the spectrometer, they can be reflected by the increasing magnetic field at both ends of the spectrometer as the longitudinal energy turns into transverse energy and eventually momentum flips direction, corresponding to magnetic trapping. From equation 3.5 it is obvious, that electrons from regions with low initial magnetic fields come along with much lower acceptance angles than θ_{max} for beta electrons. They are therefore likely being stored in the spectrometer and propagate for a long period of time (up to several hours [Lei14]). Figure 3.6 shows a typical trajectory of a stored electron. Throughout propagation, they undergo non-adiabatic interactions like scattering off residual gas molecules, producing up to thousands of tertiary electrons in turn [Lei14]. Furthermore, these processes allow for cooling, that means energy loss, of the stored electrons. The low pressure gives reason for the long cooling times. Plugging an initial energy of ΔE (eq. 3.3) into equation 3.4 yields $\theta(\vec{r}_{B_{\mathrm{max}}}) \approx \theta_0$, whereas $\theta(\vec{r}_{B_{\mathrm{max}}}) < \theta_0$ for energies below the spectrometer's filter width ΔE. This means that only electrons with $E \geq \Delta E$ can be stored, given an appropriate initial pitch angle. Thus, the lower energy threshold for the storage condition is determined by the design (standard) value of the filter width of $\Delta E = 0.93\,\mathrm{eV}$ ($\Delta E = 2.77\,\mathrm{eV}$) [A⁺21c], electrons can escape after sufficient cooling when the storage condition is broken. The upper boundary is provided by the spectrometer dimensions. If the electron's gyroradius (cyclotron motion in fig. 3.6) exceeds the spectrometer radius, which is the case at $E_{\perp} > 200\,\mathrm{keV}$ [Sch20], it will hit the wall, escaping the trap. Accordingly, the energies of stored electrons are ranging from electronvolts to a few hundred kiloelectronvolts.

Being emitted isotropically within the fluxtube and with lower energies than the stored secondary, many of the induced tertiaries will be guided towards the FPD without reflection, elevating the background. Since the involved mechanisms of creation are correlated in time, the distribution of these events does not feature Poissonian behavior. Instead, stored electrons induce the non-Poissonian component of the background. [Sch20]

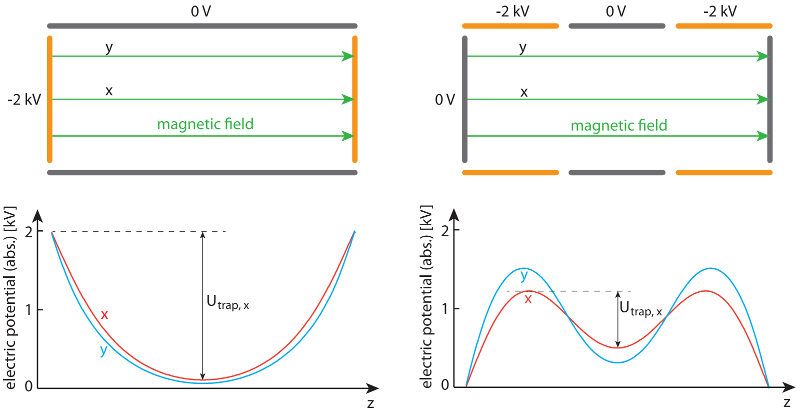

Figure 3.7.: Two types of a Penning trap (from [F⁺14]): The geometry (axially symmetric) of cathodes (orange), anodes (gray) and magnetic field lines (green) is shown in the upper part, whereas the lower part provides the corresponding progress of the electric potential along two selected magnetic field lines x and y. $U_{\text{trap,x}}$ is the depth of the trap along the field line x. Left: Penning trap between two cathodes. Right: Penning trap between two anodes. The electric potential is not quadratic. This type of Penning trap is called Penning-Malmberg trap.

Several effective methods to remove stored electrons from the spectrometers are developed. Electron cyclotron resonance, already tested succesfully in the PS [Mer12], is one possibility. Thereby a high frequency pulse, tuned to the cyclotron frequency f_g, is applied in order to increase the electron energy until their gyroradii exceed the spectrometer dimensions. Also magnetic pulses from the LFCS coils serve to remove stored particles, since a change in coil polarity distorts and opens the fluxtube, so that electrons are guided towards the walls. This procedure takes less than a second and necessary hardware is installed at the MS [A⁺21c]. The third method is an electric dipole. In the MS, an electric dipole field is formed by different potentials of the eastern and western part of the IE. This mode leads to an electromagnetically induced radial drift of the stored electrons, which probably hit the vessel walls. However, aside from the electric dipole field strength, the dipole procedure's efficiency depends on the kinetic energy of the stored electrons. Details can be found in [Wan13]. [A⁺21c, Sch20]

Decays of radon are identified as main source of stored electrons. They will be addressed in section 3.3.2 in detail.

Penning Traps

In the electromagnetic setup of the spectrometers, certain configurations of fields can result in the formation of Penning traps. Basic principle is the confinement of electrons to a defined volume due to an electrostatic potential well, restricting the movement in one direction, and a magnetic field which acts on the electron's movement in the remaining dimensions via Lorentz force. Such traps can be characterized by the potential well's depth U_{trap} [F⁺14]. Two types of Penning traps are schematically illustrated in figure 3.7.

Between PS and MS, a Penning-Malmberg trap (on the right-hand side of fig. 3.7) is formed if both spectrometers operate at a voltage of $-18.6\,\text{kV}$, corresponding to the cathodes. In between, the strong PS2 magnet can cause electrons to become confined to this region. If such a trap is sufficiently deep, secondaries, for example from cosmic rays, will be trapped and undergo non-adiabatic processes as it is the case for the formerly addressed stored electrons. Moreover, ionization of residual gas molecules can occur if the depth exceeds the ionization threshold. The number of produced tertiary electrons which are also trapped can even be on the order of 10^8

for a depth of 18 kV then and is increasing exponentially with the depth. This is also because of positive ions from ionization processes, which do not experience trapping but get accelerated towards the cathodes, producing additional electrons to fill the trap. Energetic UV photons from de-excitation of residual gas molecules give rise to electrons in the same manner, as they propagate towards the walls unaffected by the fields. It becomes evident, that throughout this process many electrons can gather in the Penning trap. If additionally the storage time allowed by the prevalent conditions is long enough and a positive feedback appears, a self-discharge can occur [F⁺14]. Such a Penning discharge releases a large number of electrons in a short time frame and is an enormous background event (> 1 kcps [F⁺17a]). For the trap between the PS and MS, it is shown that Penning discharges occur at a pressure above 5×10^{-10} mbar [A⁺21c]. However, even without a Penning discharge, electrons continuously escape the trap, also adding to the background.

Mitigation of Penning background is achieved by several measures. In addition to careful spectrometer design to prevent Penning traps, the anti-Penning electrode is installed [F⁺14] to suppress a formation and Penning wipers are employed in between of both spectrometers [A⁺20c] to empty the Penning-Malmberg trap and stop or prevent discharges [A⁺21c].

3.3.2. Radioactivity

Omnipresent traces of radioactive nuclides are challenging for particle physics experiments with low rates. This is also the case for KATRIN, where the large structures of the setup and its surroundings account for a significant level of radioactivity. In this context, it is distinguished between natural radioactivity and background due to radon decays.

Natural Radioactivity

An external source of energetic gamma quanta is for example ^{40}K. These will induce electrons when penetrating the spectrometer hull due to interactions with the stainless steel. Investigations of gamma-induced background are carried out using a 53 MBq ^{60}Co source close to the spectrometer vessel. Since the background rate is unaffected by this procedure, it is concluded that the fluxtube is shielded against these secondaries [F⁺17a]. Accordingly, external radioactivity does not contribute to the spectrometer background.

Characteristic signatures of decays show up in long-term background measurements, though. The signatures are assigned to L- and M-shell conversion lines of lead-210 in [Har15] (SDS-II measurements), confirming it as background source deposited in the spectrometer surface. In [Blo17] the ^{210}Pb imprints are validated. Thus, they stem from internal radioactivity. ^{210}Pb is part of the uranium series (primordial $4n + 2$ decay chain of ^{238}U) and formed after multiple subsequent alpha decays. The series is provided in figure A.1 (appendix A). Throughout β^- decay to ^{210}Bi, an electron with 4.16 keV or 16.16 keV [Int22] is emitted and followed by Auger or conversion electron emission. The L-shell conversion (30.15 keV) is predominant, followed in prominence by Auger electron emission (8.15 keV) and, as least probable of the three main channels, the M-shell conversion (42.54 keV) [Har15]. As the stainless steel is, i.a., selected because of its advantageous characteristics regarding radioactivity and additionally electropolished to clean the surface from contaminants before installation [Hin18], the contamination must have taken place later. In [Har15], it is proposed that radon-222 caused the implantation of lead-210 during the five year installation of the IE, as it had to be filled with ambient air with continuous ventilation for the entire procedure.

With a half-life of 3.8 d [Int22], ^{222}Rn follows the uranium series (fig. A.1) to form more short-lifed daughter nuclides until the chain reaches ^{214}Po. Since the radon can be transported towards the wall and adsorbed, it is also likely to find its progenies at the vessel surface. Eventually, the alpha

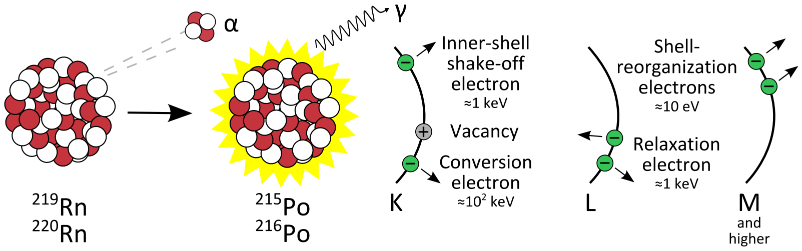

Figure 3.8.: Radon decays and subsequent electron emissions (from [Har15]): The different mechanisms of electron emission by the excited polonium nucleus (Po*) and the corresponding energies are indicated.

decays' (e.g. $Q = 7.834\,\mathrm{MeV}$ for ^{214}Po [Int22]) recoils implant the daughter nucleus, and hence ^{210}Pb, into the steel. Fabian Harms calculates a ^{210}Pb-induced activity of ~1 kBq as an estimate. Like for gamma-induced electrons above, the secondary electrons by which the contamination was identified in the first place are shielded effectively from the fluxtube. In doing so, a direct contribution to the background via Auger and conversion electrons is not provided by lead-210. Admittedly it plays an important role in a more implicit fashion. The remaining part of the background, described in section 3.3.3, requires the recoil energy of its daughter isotope ^{206}Pb to sputter excited Rydberg atoms into the spectrometer volume, neutral messengers that can in turn emit background electrons.

Radon

In ambient air, the radon isotopes ^{219}Rn, ^{220}Rn and ^{222}Rn occur as traces [SM05]. Each of these nuclides corresponds to one of the three primordial decay chains (^{235}U, ^{232}Th and ^{238}U) that are still relevant today. Radon usually emanates from minerals that are rich in their mother nuclides. Likewise in the MS's vacuum region, radon emanates predominantly from the NEG pumps. The magnetic and electrostatic shielding is ineffective against radon as neutral particle. Apart from the relevance in ^{210}Pb contamination, ^{222}Rn does not play a significant role in KATRIN background, because it is removed very quickly from the spectrometers by pumping. Compared to its half-life $T_{1/2}^{^{222}\mathrm{Rn}} = 3.8\,\mathrm{d}$ [Int22], the mean times until removal from the spectrometer volumes $\Delta t_{\mathrm{MS}} \approx 6\,\mathrm{min}$ and $\Delta t_{\mathrm{PS}} \approx 25\,\mathrm{s}$ are vanishing [Wan13]. The remaining isotopes are rather short-lifed with $T_{1/2}^{^{219}\mathrm{Rn}} = 3.96\,\mathrm{s}$ and $T_{1/2}^{^{220}\mathrm{Rn}} = 55.6\,\mathrm{s}$ [Int22] and likely decay within the spectrometer volume. An illustration of the decays and subsequent emission of electrons is provided in figure 3.8. It shows four different mechanisms. The associated energies are ranging from 10 eV to 100 keV.
Comparing these energies with the MS's filter width ΔE, it can be concluded that such electrons will be stored in most cases (see sec. 3.3.1). As a consequence, a large number of secondary electrons is created. A primary electron with $\mathcal{O}(\mathrm{keV})$ energy will induce up to some hundreds of secondaries in the course of scattering and ionization of residual gas. The number of induced electrons scales with the primary energy, until non-adiabatic effects give reason for a decreasing number again above ~10 keV. [Sch20]
To achieve retention of radon from the NEG pumps, the pump ports of the MS are equipped with LN$_2$-cooled copper baffles. These block a direct line of sight in order to ensure collisions of atoms that traverse the baffles. Radon sticks to the LN$_2$-cooled surface, whereas residual gas from the spectrometer side passes the baffles and is pumped out by the NEG pumps, or, in case of noble gases, the turbo-molecular pumps [A$^+$21c]. A reduction factor of (4.4 ± 1.2) for radon spikes in the stored electron background is observed in [G$^+$18]. In [Sch20] a rate of (23.63 ± 5.13) mcps is determined for the remaining radon-induced background. Altogether, the radon-induced background is reduced

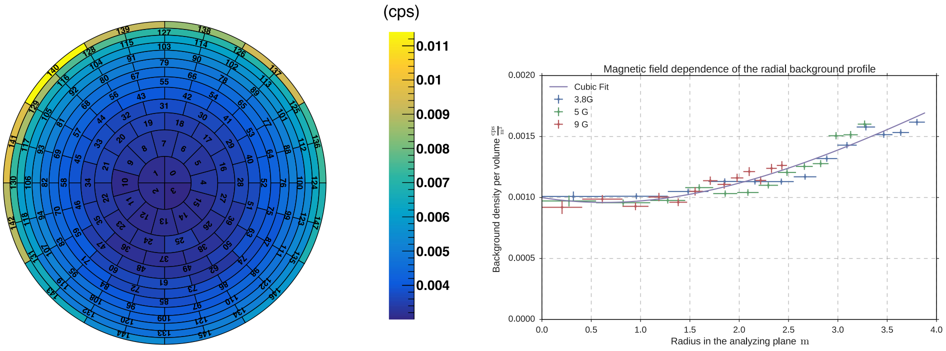

Figure 3.9.: Spatial background profile of remaining background (from [Tro19]): Left: Distribution of raw rate on FPD during background measurement, increasing towards the outer rings. Right: Background density (rate normalized to mapped fluxtube volume) over radius at AP. The subdivisions (abscissa errorbars) in the radius correspond to 13 FPD rings (as on the left). Data of three symmetric field settings with different fluxtube radii are are displayed. The background density increases with the radius.

to an acceptable level.

3.3.3. Remaining Background

In the previous sections, known background sources and countermeasures to mitigate them are discussed. As initially stated, the measured background level is currently still more than an order of magnitude above the design value, despite successful reduction strategies for the addressed components. Thus, the focus is on the remaining background. It has to be understood to make mitigation or discrimination possible.

Characteristics of the Remaining Background

During commissioning of the SDS, the remaining background distribution is observed with the FPD at symmetric LFCS field settings. The measured rate on the 148 pixels is displayed in figure 3.9. The background density per volume over radius at the AP is also provided for three symmetric settings on the right of the figure. While the raw FPD rate increases by a factor of ~3, normalization to the mapped volume reveals a roughly 50 % higher background density in the outer regions of the spectrometer volume ($r \gtrsim 3\,\text{m}$), whereby the MS's maximum inner radius of $r_{\text{max}} = 4.9\,\text{m}$ [A$^+$21c] should be noted. Moreover, the bright pixel 140 and its neighbors experience an increased rate due to a small misalignment of the beamline, since the fluxtube's distance to the spectrometer walls is reduced in this region, corresponding to larger radii. Aside from a changed fluxtube size, the spatial profile at different field settings is not affected by the magnetic field setting. The volume dependence is also investigated by assignment of the fiducial volume to the contained rate. Both quantities are proportional except for the increase towards large radii, that comes into effect by requiring a small quadratic term in the relation between volume and background rate. However, the background is evenly distributed over the MS volume except the increase for large radii, which points towards the walls as origin. [Tro19, Har15]

This hint is followed by further investigations in the same manner as it is described for muon-induced background in section 3.3.1. A highly asymmetric magnetic field setting serves for guiding electrons from the spectrometer walls towards the detector. A total area of about 250 m^2 is mapped onto the FPD this way [Har15]. Moreover, the usual efficient electromagnetic shielding of the fluxtube is evaded for this surface area. Similar results to the ones from [Har15] are obtained in

[Tro19]. The remaining background at 10^{-10} mbar is largely Poissonian, besides a small fraction of (1.99 ± 0.07) ‰. This fraction consists of clusters (correlated events) with interarrival times below $100\,\mu\mathrm{s}$. In contrast, clusters with interarrival times of up to $0.2\,\mathrm{s}$ are observed for the mostly eliminated radon background at elevated spectrometer pressure of ~10^{-8} mbar. Increased pressure is chosen to decrease the interarrival times (higher electron cooling rate due to increased abundance of residual gas molecules), allowing for an identification of clusters. Accordingly the times' distribution would be even broader, towards longer interarrival times, for lower pressures like in the mentioned remaining background scan. Consequently the clusters do not match with stored electrons. On the other hand, the differences in flight times of low energy electrons in the experiment are on the microsecond scale [Bar17], suggesting events with a few low energy electrons created at the same time. [Tro19]

The impact of electric fields on the remaining background is separated in two parts, the retarding potential and the IE offset. When it comes to the first, the behavior is very similar to radon background. The rate significantly decreases for very low retarding potentials qU_0 by a relation $\propto \mathrm{e}^{(qU_0)^{-1}}$. A more characteristic dependence is found for the IE offset voltage. With increasing offset, the overall background rate is clearly reduced (halved from $\mathcal{O}(0.1\,\mathrm{eV})$ to $\mathcal{O}(1\,\mathrm{keV})$). An outbaking procedure that removes the major part of the $\mathrm{H_2O}$-dominated monolayer on the inner spectrometer surface lowers the background rate even further. In contrast, the spatial profile is not affected significantly by variation of the IE voltage. One further tunable parameter is the vessel temperature. During imposing a slow heating cycle from 19 °C to 43 °C on the vessel, measurements of the background rate are performed. A linear relation of $(1.7 \pm 0.2)\,\mathrm{mcps/K}$ is found, corresponding to an increase of $(6.8 \pm 0.6)\,\%$. [Tro19]

To probe the effect of alpha decays in the spectrometer walls, the spectrometer was artificially contaminated with radon from two different sources, thorium-228 in December 2016 (SDS-II) and radium-223 (STS-IIIa) in October 2018 [Hin18, Tro19, Sch20, F⁺22]. The corresponding decay chains [F⁺22] read

$$ {}^{228}\mathrm{Th} \xrightarrow[1.9\,\mathrm{a}]{\alpha} {}^{224}\mathrm{Ra} \xrightarrow[3.7\,\mathrm{d}]{\alpha} {}^{220}\mathbf{Rn} \xrightarrow[56\,\mathrm{s}]{\alpha} {}^{216}\mathrm{Po} \xrightarrow[0.15\,\mathrm{s}]{\alpha} {}^{212}\mathrm{Pb} \xrightarrow[10.6\,\mathrm{h}]{\beta^-} {}^{212}\mathrm{Bi} \left\{ \begin{array}{l} (64\,\%) \xrightarrow[61\,\mathrm{min}]{\beta^-} {}^{212}\mathrm{Po} \xrightarrow[310\,\mathrm{ns}]{\alpha} \\ (36\,\%) \xrightarrow[61\,\mathrm{min}]{\alpha} {}^{208}\mathrm{Tl} \xrightarrow[3.1\,\mathrm{min}]{\beta^-} \end{array} \right\} {}^{208}\mathrm{Pb}, \tag{3.7} $$

$$ {}^{223}\mathrm{Ra} \xrightarrow[11\,\mathrm{d}]{\alpha} {}^{219}\mathbf{Rn} \xrightarrow[4\,\mathrm{s}]{\alpha} {}^{215}\mathrm{Po} \xrightarrow[1.8\,\mathrm{ms}]{\alpha} {}^{211}\mathrm{Pb} \xrightarrow[36\,\mathrm{min}]{\alpha} {}^{211}\mathrm{Bi} \xrightarrow[2.1\,\mathrm{min}]{\alpha} {}^{207}\mathrm{Tl} \xrightarrow[4.8\,\mathrm{min}]{\beta^-} {}^{207}\mathrm{Pb}, \tag{3.8} $$

where the final lead nuclides are stable in both cases and no long half-lifes occur among ^{220}Rn or ^{219}Rn and their progenies, making them suitable for a contamination over a short timescale. At first, the profile of the remaining background is reproduced well by background from contamination with ^{220}Rn (thorium measurement), that leads to a accumulation of ^{210}Pb in the MS. The measured evolution of the rate in time is indeed governed by the long half-life of lead-210. Throughout the radium measurements, the IE voltage dependence is investigated for the alpha-related background from the ^{219}Rn progeny lead-211, that is quickly accumulated after insertion of the radon gas. The remaining background's dependence on the IE potential is reproduced by this measurements [Hin18, Sch20]. In conclusion, the measurements point towards alpha decays in the spectrometer walls as origin of the remaining background. A neutral messenger particle must be produced within the processes to propagate into the MS volume, not being effectively shielded. Increasing IE voltages reduce this background fraction. Hence, it is required that the messenger is nevertheless affected by the electric potential.

Currently, the fluxtube volume that is mainly sensitive to remaining background in neutrino mass scans is reduced by application of a shifted analyzing plane (SAP) LFCS magnetic field setting

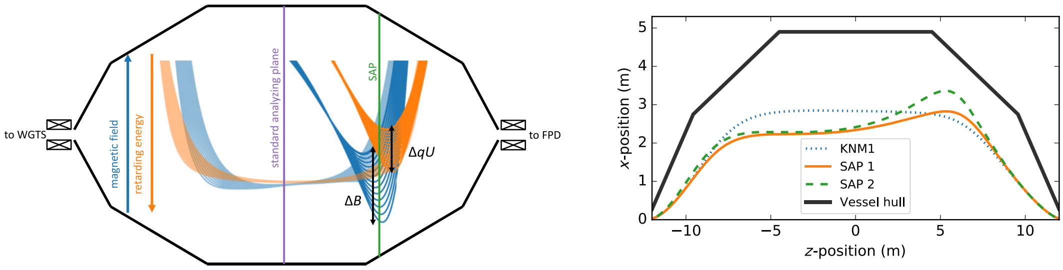

(a) (b)

Figure 3.10.: Shifted analyzing plane (from [Sch20]): Figure a: Schematic progress of the electric potential (orange) and magnetic field (blue) along the guiding magnetic field lines for standard NAP (faint) and shifted analyzing plane SAP setting (solid). The actual positions of the AP in the MS are indicated. Figure b: Fluxtube shapes of the NAP setting from KNM1 and two different examples of the SAP setting.

across the MS [L⁺22]. Compared to the symmetric normal analyzing plane (NAP) setting, SAP is an asymmetric configuration wherein the AP is shifted downstream towards the steep cone. Both magnetic and electric fields are adjusted, as it is schematically illustrated in figure 3.10. The vertical green line in figure 3.10a marks the position (z-coordinate) of the SAP and reveals the reduction of volume downstream the AP compared to NAP. The corresponding fluxtube shapes are provided in figure 3.10b, accounting for a reduction of visible volume by a factor of ~2.5 for all types of low energy electrons created within the MS [Sch20]. A reduction by the factor 2 is found in measurements, making it a powerful tool to mitigate a fraction of the remaining background. However, the SAP setting comes along with a reduced filter width ΔE compared to the KATRIN design value and inhomogeneities of the fields. [L⁺22]

The Model of Rydberg-mediated Background

Intensive studies of the remaining background established an understanding of the properties that are required for the neutral messenger and creation of electrons within the spectrometer volume. Based on the gained insights, the suggestive model of Rydberg-mediated background is established [Har15, Tro19, Sch20, F⁺22, Hin22].

It is based on the validated long-lasting contaminant lead-210 of the MS vessel ($T_{1/2}^{^{210}\mathrm{Pb}} = 22.2\,\mathrm{a}$ [Int22]). Simulations suggest a implantation depth $\mathcal{O}(100\,\text{Å})$ [Hin18, Tro19]. For the subsequent decays, it should be referred to figure A.1 (appendix A). The last step towards stability is governed by ^{210}Po with a alpha decay with a half-life of 138 d and a Q value of about 5.3 MeV [Int22]. The recoiling ^{206}Pb acquires a share of $E_{\mathrm{rec}} = 103\,\mathrm{keV}$ and propagates through the stainless steel in consequence. At the vessel surface, the ^{206}Pb interacts with the compounds of the steel, which results in the sputtering of multiple species (mainly O, Cr and Fe) into the vacuum, if the transferred energy exceeds their binding energy. A sputtering yield of about 63 atoms per ion is extracted from simulations [Hin18]. In addition, a large number of adsorbed hydrogen molecules of the monolayer covering the vessel surface contribute to the sputtered spectrum. Interestingly, sputtering can also take place at a completely different location of the spectrometer, because the recoiled ^{206}Pb might traverse the MS and interact elsewhere. Charged primary sputtered ions can propagate through the inner volume, only weakly affected by the fields, since they carry energies up to 100 keV. As long as the produced sputtering products are neutral in charge or sufficiently energetic, they can propagate into the fluxtube volume. Otherwise they will be repelled back to the wall (anion) or accelerated onto the IE (kation), also depending on their kinetic energy. [F⁺22] Throughout the energetic interactions with ^{206}Pb the sputtered atoms are additionally excited.

Highly excited states are of particular interest in the context of remaining background. Such atomic states are known as Rydberg states, named after the Swedish physicist Johannes Rydberg [Gal94]. The following introduction to Rydberg atoms is based on [Dem13] and [Gal94].
In the Bohr model of atoms, the small nucleus is surrounded by orbiting electrons, attracted by the electrostatic force. From quantization of the angular momentum to $L = n\hbar$, where the principal quantum number n occurs, and the equilibrium of forces, the orbital radius is found to be

$$r_n = \frac{4\pi\varepsilon_0\hbar^2}{m_e e^2}\frac{n^2}{Z} \tag{3.9}$$

for a nuclear charge of Ze. The smallest possible orbital radius r_1 of the hydrogen atom ($Z = 1$) is the proportionality constant a_0 of r_n and n^2/Z, adding up up to $a_0 = 0.529\,\text{Å}$. This constant is referred to as Bohr radius. The binding energy E_n of the electron is the sum of the electric potential energy $-eU(r_n)$, hence scaling with r_n^{-1} and the atomic number Z, and the kinetic energy $E_{\text{kin},n} = -1/2(-eU(r_n))$ (with the virial theorem for the Coulomb force):

$$E_n = E_{\text{kin},n} - eU(r_n) = -\frac{1}{2}eU(r_n) = -\frac{1}{2}\frac{Ze^2}{4\pi\varepsilon_0 r_n} = -\frac{e^4 m_e}{2(4\pi\varepsilon_0\hbar)^2}\frac{Z^2}{n^2} = -R_y\frac{Z^2}{n^2}. \tag{3.10}$$

Here, the Rydberg energy $R_y = 13.6\,\text{eV}$ is introduced. For very high n, the electron is only very loosely bound with $\propto n^{-2}$ and can easily be excited into the continuum. The above formula applies for systems with one electron. In case of more than one, corrections to the Coulomb potential have to be made due to the other electrons. These resolve the accidental degeneracy of states with different allowed angular momenta (orbital quantum number ℓ) for a fixed principal quantum number n. Rydberg already noted that a small phenomenological correction can be used for hydrogen-like systems (alkali atoms), where the single outer electron approximately experiences an effective nuclear charge as in the hydrogen atom at large distances from the nucleus. The energy becomes

$$E_{n\ell} = -\frac{R_y}{(n-\delta_{n\ell})^2} =: -\frac{R_y}{n^{*2}} \tag{3.11}$$

with the effective principal quantum number n^* that takes the quantum defect $\delta_{n\ell}$ into account. The difference between n and n^* increases with low values of n and ℓ, because the shielding effect of the inner electrons decreases due to a higher probability of finding the considered electron at the nucleus.
Excited atomic states decay via radiative transitions. The computation of both transition rate and lifetime $\tau_{n\ell}$ of a state is based on the Einstein coefficients $A_{n'\ell',n\ell}$ of the $n,\ell \longrightarrow n',\ell'$ transition. These are depending on the frequency $\omega_{n'\ell',n\ell}$ of the decay, n, ℓ and the radial matrix element of the involved states and are related to the lifetime by

$$\tau_{n\ell} = \frac{1}{\sum_{n'\ell'} A_{n'\ell',n\ell}}. \tag{3.12}$$

Since $\Delta\ell = \pm 1$, the highest frequency ω_{max} of a radiative decay is always determined by the transition to lowest possible state with $\ell' = \ell - 1$. In the limit of high n, this frequency approaches a constant value and the rate only depends on the radial matrix element between Rydberg state and lower lying state, which occurs squared with and scales with n^{-3} due to wavefunction normalization. Hence, the lifetime of a $n\ell$ Rydberg state is $\tau_{n\ell} \propto n^{-3}$, if the angular momentum is not too high. In [Tro19], $\tau_{n\ell} \propto \ell(\ell+1)n^3$ is semiclassically motivated, which is in agreement with the obtained result for low ℓ.

For states with high orbital momenta $\ell \approx n$ (we will consider $\ell = n - 1$) the frequency can not assumed to be constant. It scales with n^{-3} instead. As it contributes cubed and is multiplied by the high ℓ transition radial matrix element $\propto n^2$, the lifetime is $\tau_{n,n-1} \propto n^5$, which also matches the relation from [Tro19] for high $n - 1 = \ell$. In practice, it is useful to form a statistical mixture of different ℓ and m_ℓ (magnetic quantum number) states and average over their lifetimes. By following this procedure, the average lifetime

$$\bar{\tau}_n \propto n^{4.5} \tag{3.13}$$

of a n state is obtained. The proportionality constant for the relations and thus the associated time scale of the lifetimes is $\mathcal{O}(0.1\,\mathrm{ns})$ [Tro19].

We will refer to Rydberg atoms as states with about $n > 10$ up to arbitrarily high n. They can reach remarkable dimensions according to equation 3.9, which yields $r_{10} = 100a_0 = 5.29\,\mathrm{nm}$ and for $n = 100$ even $r_{100} = 0.529\,\mu\mathrm{m}$ in case of an excited hydrogen atom. The corresponding binding energies are $E_{10} = -136\,\mathrm{meV}$ and $E_{100} = -1.36\,\mathrm{meV}$, making an ionization even by low energy photons possible. Additionally, the lifetime of the Rydberg state is strongly prolonged by $n^{4.5}$ to $\mathcal{O}(\bar{\tau}_{10}) = 1\,\mu\mathrm{s}$ or $\mathcal{O}(\bar{\tau}_{100}) = 0.1\,\mathrm{s}$. Moreover, the state can decay in a lower state, which still features high n and lifetime.

Altogether, sputtered atoms that are excited to high n Rydberg states with a probability of n^{-3} serve as potential neutral messengers. The extraordinary lifetimes and electric neutrality allow for a propagation into the spectrometer volume. The remaining background decreases with higher IE offsets, meaning that a dependence also has to be given for the messenger. This is the case for Rydberg states, indeed, due to the Stark and Zeeman effect: within an external electric field they are not stable. The electron can escape the bound state due to the external potential, which would be expressed as increasing fluxtube shielding, as the Rydberg states are ionized in the between vessel wall and IE. The perturbation vanishes in the fluxtube [F⁺22]. Simulations and measurements of the IE offset dependence are in good agreement [Tro19].

The model of Rydberg-mediated background is based on different cornerstones, that are introduced above, namely low ionization thresholds, electric neutrality an long lifetimes. One more mechanism is still required for an explanation of the remaining background from across the spectrometer volume. This is the ionization mechanism to deliver the low required energies on the range of milli- to electronvolts. One possibility is the ionization via photons from the black-body radiation (BBR) of the MS vessel. At room temperature, the maximum of the spectrum is in the infrared, corresponding to photon energies comparable to the ionization thresholds, i.e. ~(1 meV – 1 eV). The $690\,\mathrm{m}^2$ [A⁺21c] of surface radiate BBR and contribute to the thermal radiation density in the fluxtube volume. The entire BBR-induced Rydberg background mechanism is provided in figure 3.11. However, BBR does not only stimulate ionization but also photo-emission of the excited atoms, de-excitation and excitation to higher levels. Therefore, it affects Rydberg states in several ways. Anyways, it is considered the main mechanism for ionization of states in the sensitive fluxtube volume. [F⁺22]

Apart from room temperature BBR, several other potential ionization mechanisms are proposed and investigated [Har15, Tro19], especially in [Hin18] and [Hin22]. In this thesis, they will not be addressed in detail, but for the sake of completeness, these processes are Penning ionization, field ionization and auto-ionization, due to metastable states and of doubly excited states, so-called planetary atoms. For details, it should be referred to [Hin22].

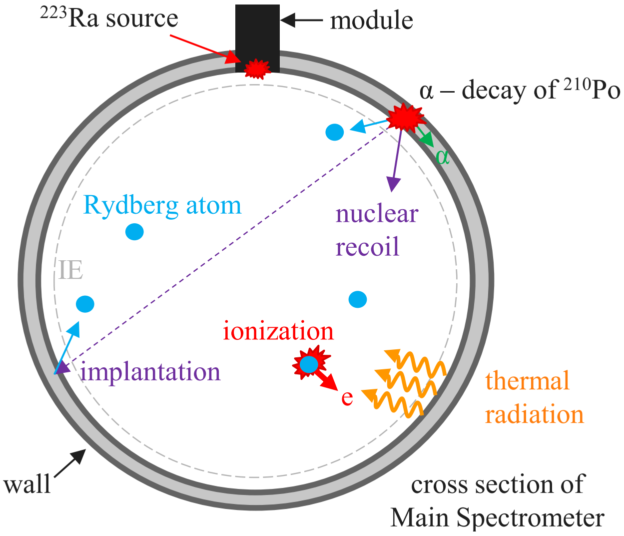

Figure 3.11.: Rydberg state-induced background mechanism (from [F⁺22]): The recoil of ^{206}Pb, progeny of ^{210}Po in the spectrometer wall, sputters atoms or ions into the spectrometer volume. Rydberg states occur due to excitation. Explanted atoms might also traverse the spectrometer and induce Rydberg states elsewhere. The latter are neutral messengers that are ionized by low energy photons from the thermal BBR of the MS walls. These can constitute the remaining background. The ^{223}Ra source from the mentioned radium measurements is also added to the scheme.

4. Transverse Energy Filters (TEFs)

To achieve the design sensitivity, background in the experiment has to be reduced drastically by an order of magnitude, as a level of ~10 mcps is required in the ROI [F^{+}22] (see chap. 3). Reduction of the remaining background is challenging, as it is provided by the same particle like the signal and features similar energies, as explained in section 3.3.3. So far, KATRIN does not provide a procedure or mechanism to distinguish this background fraction from signal immediately. Sensitivity to the electrons' angular distributions is the key to a discrimination of remaining background [G^{+}22]. Transverse energy filters (TEFs) are the current promising approach to realize angular selectivity in the KATRIN experiment. An introduction to background discrimination with angle-selective TEFs is given in section 4.1. In section 4.2, two different main types of them are specified.

4.1. Background Discrimination by angular Selectivity

In section 3.3.3, the remaining background is introduced. For some years already, Rydberg-mediated background is investigated and discussed in numerous works, for example in [Hin18], [Tro19], [Sch20], [G^{+}22], [F^{+}22] and [Hin22]. The small surplus energies of the electrons from Rydberg state ionization of $E \lesssim 150\,\mathrm{meV}$ [Tro19] are an important characteristic. According to ionization due to BBR, the most probable energies are however on the order of $k_\mathrm{B}T \approx 25\,\mathrm{meV} \approx \varepsilon$ at room temperature [G^{+}22], also limiting the transverse energy $E_\perp$ to a small value.
Depending on the region of origin, these electron acquire longitudinal energies up to $E_\parallel = qU_0 + \varepsilon$. Even in a case of fully transverse emission ($E_\perp = \varepsilon$ at the time of ionization), the electrostatic boost of many kiloelectronvolts downstream the AP due to the potential gradient results in $E_\perp \ll E_\parallel$ at the FPD. Consequently, a narrow incidence angle distribution at small angles is expected for Rydberg-mediated electrons. Figure 4.1 displays the incidence angle distributions of each 10^5 simulated electrons from beta decay after propagation along the beamline (orange) as well as from Rydberg state ionization (blue). Indeed, their incidence angle is typically below ~10° and rather even lower in mean, at about 3°. In contrast, the beta electrons' incidence angle distribution increases towards larger angles before dropping above 49° towards θ_max. This behavior is expected from isotropic emission and consideration of the solid angle (nominally, $B_\mathrm{s} \approx B_\mathrm{det} = 2.5\,\mathrm{T}$ [A^{+}21c]). [G^{+}22]
Besides the cyclotron frequency f_g (eq. 2.23), an electron's gyroradius r_g can be obtained via

$$r_g = \gamma r_{g,0} = \gamma \frac{p_\perp}{eB} \tag{4.1}$$

with similar notation as in equation 2.23 and the transverse momentum $p_\perp = p\sin(\theta)$, depending on momentum p and pitch angle θ. Since $p_\perp$ roughly scales with E and $p_\perp \propto \sin(\theta)$ (for small angles $p_\perp \propto \theta$), the trajectories claim larger volumes with increasing energy and, particularly important, large pitch angles. An investigation of the actual trajectories points out how the angular characteristics can be exploited to discriminate Rydberg-mediated background. The

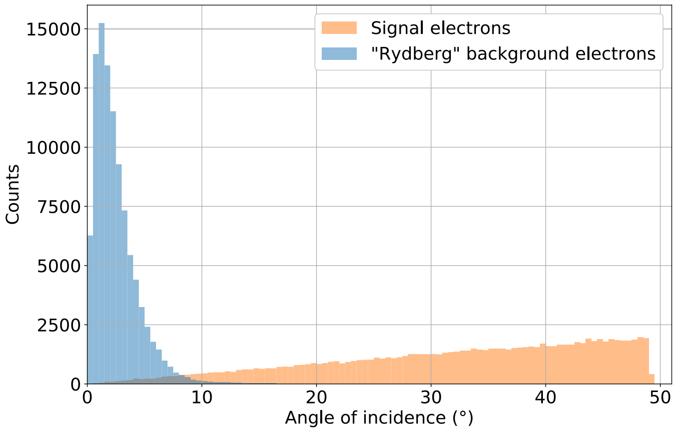

Figure 4.1.: Angular distribution of signal and "Rydberg" background electrons at the FPD (from [G⁺22]): Simulation of 10^5 electrons. Ionization of Rydberg states occurs due to BBR of the MS at room temperature. The surface model is 36 % hydrogen and 64 % oxygen, sputtered into the MS as Rydberg states by ^{210}Po alpha decays within the vessel surface. Binding energies, electron energies and directions and the Doppler shift are taken into account. Input from [Tro19] and [F⁺22].

corresponding principle of a TEF is illustrated in figure 4.2. The angular selectivity manifests itself in the feature of increased transmission for small angles, while electrons with larger pitch angles and gyroradii mainly hit the structure, resulting in particle termination in many cases. Of course, the transmission also depends on the gyroradius. However, even for large radii, a sufficiently low pitch angle can still allow for transmission. Moreover, the gyroradius itself (eq. 4.1) depends on the pitch angle. For an application in KATRIN, which allows for background reduction, the filtering structure (yellow in fig. 4.2) should be the detector at the same time, of course, to obtain large signal fractions.

4.2. Types of Transverse Energy Filters

Active Transverse Energy Filter

An active transverse energy filter (aTEF) detects the fraction of electrons hitting the TEF structure (yellow channels in fig. 4.2). A proof of principle for the aTEF method using a microchannel plate is provided in [G⁺22]. In this case, an electron hit on the channel wall releases several secondary electrons, which do in turn induce an electron cascade along the channel. It is accelerated by an external voltage and allows for detection. For an application in KATRIN, microchannel plates are ruled out due to several reasons, though. [G⁺22]

Alternative designs also require some type of three-dimensional structure, serving as an obstacle for spiraling beta electrons. Basically, various types of microstructured detectors could serve this purpose, as long as they provide an adequate signal detection efficiency. Etching of PIN diodes is currently subject of research and development (R&D) towards a silicon-based active TEF (referred to as Si-aTEF). In case of the Si-aTEF, fabrication of silicon microstructures is achieved via highly anisotropic cryo-etching at the Münster Nanofabrication Facility [G⁺22]. One of the microstructures is shown in figure 4.3, recorded with scanning electron microscopy (SEM). A hexagonal honeycomb structure is chosen, which is a geometry featuring a high open area ratio (OAR) and stability. In the scenario of an etched FPD, the channels' base areas (lower bulk region in fig. 4.3) have to be insensitive to electrons, whereas the walls have to be the sensitive region of

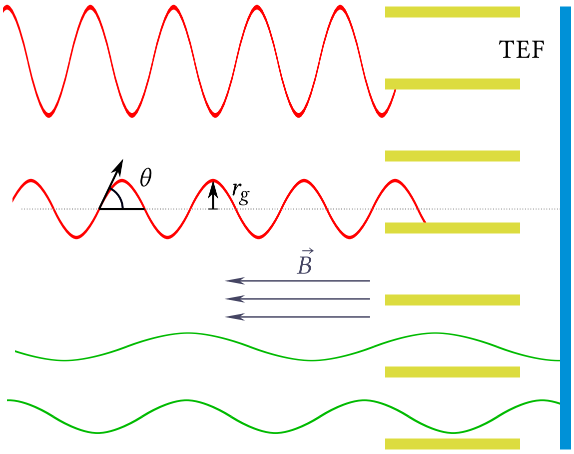

Figure 4.2.: Principle of a TEF: Rydberg-mediated background electrons (green) with low pitch angles are mainly transmitted through TEF channels (yellow), whereas a large fraction of signal electrons (red) hit the structure due to the different angular distribution (fig. 4.1). The channel size is on the order of 100 µm. The magnetic field $\vec{B}$ is indicated and definitions of the pitch angle θ and the gyroradius r_g can also be extracted from the figure.

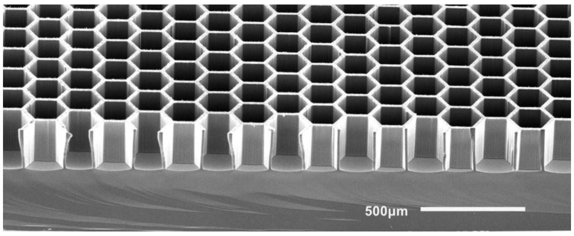

Figure 4.3.: SEM image of Si-aTEF silicon sample structure (from [G$^+$22]): The microstructure is fabricated by etching of silicon at the Münster Nanofabrication Facility. Each hexagon has a side length of 100 µm, depth of 225 µm and wall thickness of 10 µm.

the PIN diode. However, the upper edges of the walls (bright hexagonal grid in upper region of fig. 4.3) are exposed to the full flux of both signal and background equally, giving reason for a large OAR.

Within this work, the alternative idea of a scintillating aTEF (scint-aTEF) is pursued. It relies upon the interaction of electrons with scintillating material, causing an optical signal that can be detected. Hence, in contrast to the Si-aTEF, a scintillator must be microstructured. Furthermore, an appropriate detector has to be designed. In chapter 6, the principle and R&D process of the scint-aTEF are described extensively.

Passive Transverse Energy Filter

Different from the active mode of a TEF, it can also be used in passive mode as a passive TEF (pTEF). This is the case, if the structure itself is not the sensitive part of the configuration. Instead, the transmitted fraction ξ of electrons (green trajectories in fig. 4.2) is detected behind the pTEF (blue bulk in fig. 4.2). In the KATRIN experiment, this corresponds to a rate measurement downstream the pTEF, which can be carried out with the FPD without major difficulties. Recalling figure 4.2 allows for the estimation of a much worse SBR of the measured rate in this case. Accordingly, the pTEF favors detection of the remaining background fractions, whereas beta spectroscopy with background discrimination can potentially be achieved with an aTEF.

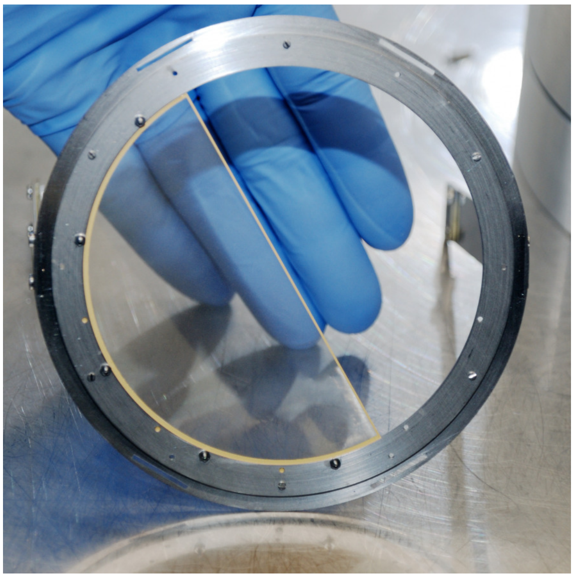

Figure 4.4.: pTEF mounted in dedicated holding structure (stainless steel frame): The left semicircle is covered by the microstructured grid, which appears golden and features transparency at the almost perpendicular viewing angle. Microscopic images of the surface are provided in fig. 5.2.

So far, angular distributions (like fig. 4.1) can not be obtained in the experiment. Offering angular selectivity without the need for additional sophisticated instrumentation, the pTEF represents a promising approach to gain insights into angular characteristics of different rate components in KATRIN. Tuneable parameters are on the one hand fixed, like the pTEF geometry (e.g. channel dimensions), and, on the other hand, adjustable, like the LFCS setting and the retarding potential. Within the past two years, R&D of a pTEF progressed significantly, resulting in the production and integration of the first pTEF into the KATRIN beamline and a dedicated measurement campaign [HHL21]. For an extensive documentation, analysis and discussion of the first pTEF campaign, it should be referred to the thesis of Dominic Hinz [Hin22].

Apparently, geometric permeability is mandatory for the pTEF. This is fulfilled by usage of a grid structure with actual through holes or channels. For similar reasons as for the Si-aTEF, a honeycomb grid is chosen, which is made from gold. A photograph of the pTEF, mounted in a dedicated holding structure, is provided in figure 4.4, featuring high transparency at the almost perpendicular view onto the surface, yet appearing golden. The channel dimensions of the hexagons are optimized to satisfy the requirements from both the feasibility of fabrication and the expectations for the transmission behavior.

Details concerning the pTEF as well as studies of the backgrounds to be investigated with it and geometric aspects in combination with the filtering properties, that have been carried out in the scope of this work, are presented in the subsequent chapter 5. The concept of a double pTEF (2pTEF) with different characteristics is introduced and also a central subject of these investigations.

5. Simulations and Studies of a passive TEF and Background

The first pTEF for the KATRIN experiment is basically a microstructured honeycomb grid from gold, as stated in section 4.2. However, the dimensioning and layout of this TEF are established advisedly throughout the R&D process. The first pTEF will shortly be introduced in section 5.1. Afterwards, as the background to be investigated with the pTEF plays a central role, components of the KATRIN background are investigated regarding their angular distributions in section 5.2. As the integration of the first pTEF into the KATRIN beamline takes place in December 2020, the overall configuration and the filtering properties are an important topic of discussion during the processing period of this work. Hence, studies of geometric aspects and filtering properties and systematics are carried out and the presented in section 5.3

5.1. The first pTEF

A definition of the pTEF's geometric parameters can be found in figure 5.1. There are essentially three parameters: the edge length a, the thickness b of the walls and the structure's height d, representing both the channel length and thickness of the pTEF. These parameters are set to

$$\begin{aligned} a &= 100\,\mu\text{m}, \\ b &= 8\,\mu\text{m}, \\ d &= 250\,\mu\text{m} \end{aligned} \tag{5.1}$$

for the first pTEF [HHL21], based on previous studies on TEFs. It is made by Microworks GmbH in Karlsruhe using a fabrication technique called LIGA (german *Lithographie, Galvanoformung,*

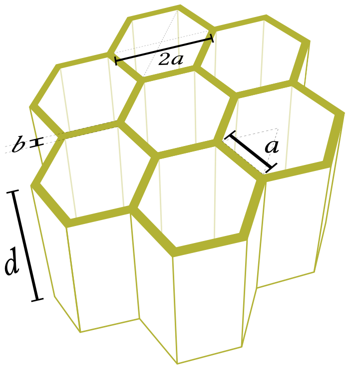

Figure 5.1.: Definition of the pTEF's geometric parameters: The hexagons have an inner side length or edge length of a and diameter $2a$, accordingly. b is the wall thickness and d the height (corresponding to channel length or thickness of the pTEF) of the honeycomb grid.

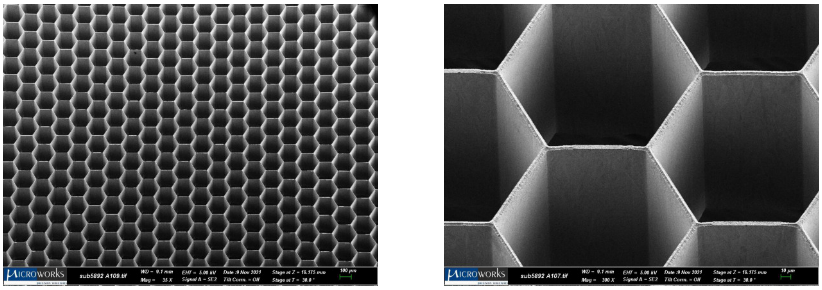

(a) (b)

Figure 5.2.: SEM images (by Microworks GmbH) of the pTEF with dimensions as in eq. 5.1 (material: gold): Figure a: Image of the pTEF structure, taken at 35× power. Figure b: Magnification of surface frame from fig. a to 300× power. A macroscopic photograph can be found in fig. 4.4.

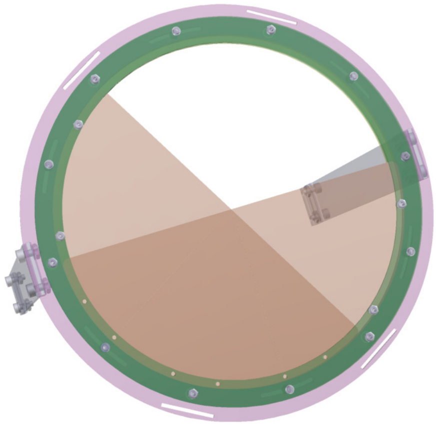

Figure 5.3.: Drawing of the 2pTEF mounted in dedicated holding structure: The setup is similar to fig. 4.4. In addition, a second pTEF grid is employed, rotated by 60° with respect to the first one. Hence, three regions arise: open, covered by one pTEF layer and by two layers (actual 2pTEF region).

Abformung – lithography, electroplating, molding), allowing for the sub-micrometer resolution of three-dimensional structures that is required by equation 5.1. SEM images of the acutal pTEF surface are presented in figure 5.2, demonstrating the high precision of LIGA.
A more macroscopic view is already provided in figure 4.4. The visibly high degree of transparency reflects the large OAR, realized by the geometry (hexagonal grid, eq. 5.1). Also, the pTEF presents itself as a semicircle, covering only half of the magnetic fluxtube which penetrates the surface perpendicularly. This layout of a partially uncovered fluxtube ensures the measurement of a reference rate on the FPD. Two more images of the pTEF installed in front (upstream) of the FPD are provided in appendix B (fig. B.2).
However, installation of a double pTEF (2pTEF) is also a considered scenario. This configuration requires two pTEF layers employed in series, as figure 5.3 illustrates. In total, one layer and two layers of pTEF cover one third of the fluxtube each. The remaining third is uncovered to provide a reference region, again. The intended distance between both layers is

$$\Delta z = 500\,\mu\text{m}. \tag{5.2}$$

Transmitted electrons will propagate undisturbed in the gap between both pTEFs until they reach the second layer, where they might again interact with the pTEF. Therefore, in the actual 2pTEF region, the filtering effect is enhanced. As additionally, a pTEF region of equal size does still exist, no data is lost compared to the normal pTEF, but it just covers a smaller fraction of the fluxtube area, resulting in less rate or statistics per region. It must be taken into account, that the overlapping layout of the pixels of neighboring rings on the FPD enforces rejection of several pixels on the pTEF regions' projected boundaries. This also holds for the normal pTEF, of course, but the effect is half as strong.

To ensure a proper and predictable behavior of the pTEF, knowledge about the magnetic field is a prerequisite. It is desired, that electrons with vanishing pitch angle $\theta = 0$ are transmitted, if they do not hit the channels' front surfaces. This corresponds to the maximum physically achievable transmission

$$\xi_{\max} = \mathrm{OAR}. \tag{5.3}$$

However, this limit only holds, if ${}^{\mathrm{d}B}\!/_{\mathrm{d}z} = 0$, which is motivated as follows: azimuthal independence of the pTEF properties is ensured by installation with surface normal parallel to the z-direction and alignment with the fluxutube center. The nominal magnetic field of the fluxtube neither has an azimuthal dependence but a radial gradient. If the magnetic field exhibits an axial gradient, the field lines $\vec{B}$ will not be aligned with the surface normal or $\vec{z}$, but intersect the channel walls, as $\theta \neq \theta_z$.

Along the beamline downstream the AP, the field increases drastically towards the pinch magnet's center. Afterwards it widens again, just to be narrowed another time by the detector magnet. Each of these three positions correspond to a local extremum of the magnetic field strength B, corresponding to the required condition of vanishing axial gradient. Due to its proximity to the FPD and feasibility of the installation there, the local maximum of $B \approx 2.5\,\mathrm{T}$ with a fluxtube radius of $r_B = 44\,\mathrm{mm}$ at the detector magnet's center is chosen as the pTEF position [HHL21]. Kassiopeia simulations of the STS's and SDS's magnetic fields by Dominic Hinz [HHL21] yield a vanishing gradient at

$$z_0 = 13.783\,75\,\mathrm{m}, \tag{5.4}$$

in global KATRIN coordinates. The fluxtube radius r scales with ${}^{\mathrm{d}r}\!/_{\mathrm{d}z} \leq 2.5\,{}^{\mu\mathrm{m}}\!/_{\mathrm{mm}}$ in the $\pm 2\,\mathrm{cm}$ surrounding of this maximum, corresponding to $\theta_{z,\max} = 0.143°$ [HHL21]. This suffices equation 5.3 approximately. z_0 is chosen as installation position of the pTEF.

5.2. Angular Distribution of specific KATRIN Backgrounds

In order to make statements about the the pTEF's filtering properties, an understanding of the incident electrons' characteristics is a prerequisite. Particularly the angular distributions are essential, as motivated in chapter 4. In the scope of this work, the focus is on Rydberg-mediated and radon-induced background.

Simulations are carried out to acquire these information. For their initialization, primary electrons have to be generated at a certain position $\vec{x}_\mathrm{i}$ with momentum $\vec{p}_\mathrm{i}$ in the considered environment. Both vectors have to be recovered from the corresponding probability distribution or directly via simulation of the underlying creation processes. Afterwards their interactions throughout propagation in the experimental setup determine their state $(\vec{x}_\mathrm{f}, \vec{p}_\mathrm{f})$ as they reach the location of interest (in our case the site where filtering takes place). Only a fraction of them will reach this region, while the remaining share terminates elsewhere. Interactions to be taken into account obviously include electromagnetic interactions with the applied magnetic and the electric field of the spectrometer, but also non-adiabatic processes like scattering with residual gas molecules. It should also be possible to retrieve information about the environment of the electron, for example the prevailing magnetic field and therefore the pitch angle θ in the end (θ_f).

Kassiopeia Simulations

The software package *Kassiopeia* relies upon three libraries of the superordinate C++ framework *KASPER*. Further information is provided in [Gro15, Beh16, F$^+$17b] and [Kas22]. Kassiopeia, originally developed specifically for simulations of the KATRIN experiment, is an object-oriented C++ package for the simulation and tracking of particles in low-energy ($< 100\,\mathrm{keV}$) electro- and magnetostatic environments wherein scattering also occurs. Hence, it perfectly serves for our purposes and is used for the investigations. A Kassiopeia simulation requires a configuration file, which has to be provided in the extended markup language (XML) format and includes the geometry for navigation regions, electromagnetic fields and the conditions for particle creation and termination [Beh16]. In the following, the simulations' setup will be outlined.

The considered regions of the experiment are mainly MS and the surrounding of z_0 (eq. 5.4) between pinch and detector magnet, altogether corresponding to the SDS. Furthermore, the STS's fields will also be included to ensure correct behavior in the upstream direction from the MS. Both Rydberg state- and radon-induced background are generated homogeneously distributed across the fluxtube volume in the MS. This approximates the known behavior (sec. 3.3). Hence, $\vec{x}_\mathrm{i}$ is diced from a uniform distribution in z direction in the range $[-11.5\,\mathrm{m}, +11.5\,\mathrm{m}]$ (axial coordinate) and a uniform circular distribution in the x-y-plane (radial coordinate $\rho = \sqrt{x^2 + y^2}$) with $\rho \leq 3.7\,\mathrm{m}$, resulting in a homogeneous cylindrical distribution. The limits are chosen because of the fluxtube and MS dimensions. An isotropic distribution of the initial direction of $\vec{p}_\mathrm{i}$ is assumed. While the azimuthal angle φ is uniformly distributed, the solid angle scaling has to be taken into account for the polar angle θ_z, thus requiring $\cos(\theta_z)$ uniformly distributed. The position and direction generators, part of a `ksgen_generator_composite`, are provided in XML format below.

```xml
<!-- position creation -->
<position_homogeneous_flux_tube r_max="3.7" z_min="-11.5" z_max="11.5" phi_min="0."
    phi_max="360." magnetic_field_name="field_magnet_global"/>
<!-- direction creation -->
<direction_spherical_composite>
  <theta_spherical angle_min="0." angle_max="180."/>
  <phi_uniform value_min="0." value_max="360."/>
</direction_spherical_composite>
```

The magnetic field `field_magnet_global` includes the contributions from STS and STS. The initial momentum $\vec{p}_\mathrm{i}$ is obtained from initial direction and energy E_i. For the latter, another generator has to be introduced, which will be addressed later.

Because equation 3.2 is approximately satisfied, an adiabatic trajectory model is chosen for the simulations. The included adiabatic stepping size comes along with the advantage of fast computation compared to usage of the exact trajectory. Scattering processes along the trajectory occur due to the inclusion of residual hydrogen:

```xml
<!-- interactions -->
<ksint_scattering name="int_scattering" enhancement="1e7">
  <density_constant temperature="300." pressure="4.e-11"/>
  <calculator_hydrogen elastic="true" excitation="true" ionisation="true"/>
</ksint_scattering>
```

Constant residual gas density at a pressure of $p_\mathrm{res} = 4 \times 10^{-11}\,\mathrm{mbar}$ and room temperature is set. Besides elastic scattering, excitation and ionization can also occur. The enhancement of the scattering probability is set to 10^7, leading to higher cooling rates for stored electrons. A lower enhancement would result in extremely time-consuming simulations in some cases, since the electrons trajectory is tracked until it escapes the trap and terminates. For the termination of electrons, multiple termination conditions are defined, including radial and axial boundaries as well as a maximum number of 10^6 steps to reject trapped electrons after a certain time. A virtual

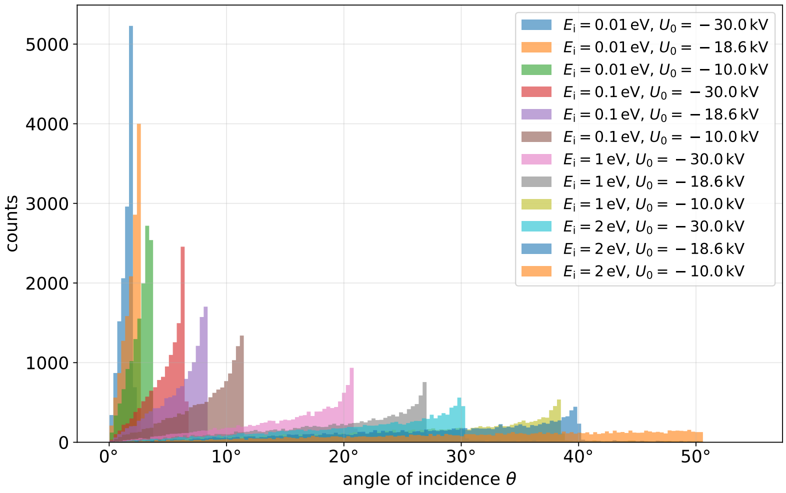

Figure 5.4.: Angular distributions of monoenergetic fluxtube background: The binned number of events is plotted over the angles of incidence θ (pitch angle) they are hitting the reference surface with. Of 3×10^4 generated electrons, each histogram (certain initial electron energy E_i) contains the electrons that are terminated on the virtual pTEF surface at z_0.

pTEF surface is the most important terminator. It consists of a circular disk, representing a virtual pTEF, with a diameter of $D = 12\,\mathrm{cm}$ (whole fluxtube is mapped onto the disk) at $z_0 = 13.783\,75\,\mathrm{m}$. In the output *ROOT* file, a group is defined into which the data of terminated electrons is written. At first, simulations of monoenergetically generated electrons from a uniform spatial profile (vide supra) in the fluxtube are carried out to estimate their angular distributions. This can be understood as a study of artificial monoenergetic "fluxtube backgroud". The 6.0 G LFCS setting is set for each simulation, whereas both retarding voltage U_0 and initial energy E_i are varied over a typical range from rather low to high values of the quantity. The air coil current values for the LFCS setting are listed in the XML configuration in appendix B. Hull voltage and IE offset (`ie_common_potential`, −200 eV) sum up to U_0. The PAE is on ground. Setting the energy to a certain value requires

```xml
<!-- energy creation -->
<energy_composite>
        <energy_fix value="[start_energy]"/>
</energy_composite>
```

Arbitrary values in electronvolt can be set externally for the variable `start_energy`.

3×10^4 electrons are generated for each combination (E_i, U_0). Figure 5.4 shows the angular distributions of the virtual pTEF-terminated electrons. The regarded angle is the angle of incidence θ_z on the virtual pTEF, which can be considered equivalent to the pitch angle θ due to the choice of z_0 (see sec. 5.1). The histograms reveal an overall behavior of increasing angular distributions towards a maximum or cutoff angle θ_{cut}. This behavior and also the energy dependence of θ_{cut} can be understood by recapitulation of equation 3.4 in the limit of $\theta_0 = 90°$ for the corresponding field strengths B and energies $E(\vec{r}_0) = E_i$ and $E(\vec{r}) \approx qU_0$. The electrostatic boost downstream only affects $E_\parallel$ and therefore narrows the pitch angle, shifting the distribution towards smaller angles with increasing energies qU_0.

From these first results, it can be concluded that the retarding potential will directly affect the filtering properties of the pTEF due to its implications for the angular distribution. Hence, it could also be exploited to tune the trajectories regarding their pitch angles and gyroradii to obtain additional data from transmission measurements. Of course, the introduced monoenergetic fluxtube background only serves as a pre-study, because background electrons actually feature broad energy distributions, which are addressed in the following sections 5.2.1 (Rybderg-mediated) and 5.2.2 (radon-induced background).

5.2.1. Characterization of Rydberg-mediated Background

In order to generate Rydberg state-induced background electrons, it satisfies our requirements to make use of a semi-empirical approach which relies upon the findings of [Tro19] to derive the probability density function (PDF) ${}^{\mathrm{d}\mathcal{P}}/_{\mathrm{d}E}(E)$ of the probability $\mathcal{P}$ with respect to the energy E.
At first, it is taken into account that the Rydberg state-induced electrons reaching the detector are most likely produced by atoms which have been excited into states with a large principal quantum number of about $n = 50$ [Tro19]. Although their distribution spreads from $n > 10$ to single events even above $n = 400$, two orders of magnitude separate them from the frequency of states with $n = 50$, thus allowing for the simplified use of the corresponding value $n \approx 50$ for the electrons, corresponding to a binding energy of ~5 meV (eq. 3.10, hydrogen atom). The PDF ${}^{\mathrm{d}\mathcal{P}}/_{\mathrm{d}E}(E)$ is provided in figure B.3 (appendix B) for different principal quantum numbers.
The pre-studies indicate that the angle is not affected to much by variations of the initial energy in the few 10 meV regime, where the power law differs notably for different n. Also, due to the behavior of ${}^{\mathrm{d}\mathcal{P}}/_{\mathrm{d}E}$ under variation of the principal quantum number around $n \approx 50$ the fluctuations should cancel out to significant parts. Therefore, the simulation of Rydberg-mediated background is based on the spectrum at $n = 60$ [Tro19]. This PDF can be – in a simplified version for an easy implementation – approximated by

$$\frac{\mathrm{d}\mathcal{P}}{\mathrm{d}E}(E) = \mathcal{N}\,\frac{\mathrm{e}^{-\lambda E}}{\sqrt{E + \delta E}} \qquad (0 \le E \le 250\,\mathrm{meV} =: E_{\mathrm{max}}), \tag{5.5}$$

where $\lambda^{-1} = 23\,\mathrm{meV}$, $\delta E = 1\,\mathrm{meV}$ and $\mathcal{N}$ in $\mathrm{eV}^{-1/2}$ is a normalization constant for $\int_0^{E_{\mathrm{max}}} \mathrm{d}\mathcal{P}(E) = 1$. The restriction towards higher energies is applied because the probability quickly drops for increasing energies around 100 meV. Typical room temperature BBR energies of $k_{\mathrm{B}}T \approx 25\,\mathrm{meV}$ and surplus energies of the Rydberg state-induced electrons mainly below 150 meV [Tro19] are stated in section 4.1. It is checked thoroughly that equation 5.5 reproduces the actual ratios of different energies well. Hence, the energy distribution 5.5 is used for the Rydberg-mediated background generator. Different from the monoenergetic case in the preceding section, a non-uniform energy distribution is now used in Kassiopeia. In the XML configuration, line 3 of the energy creation (vide supra) has to be replaced:

```xml
<!-- energy creation -->
<energy_composite>
  <energy_formula value_min="0." value_max="0.25" value_formula="TMath::Exp(-x/0.023)/
      TMath::Power((x+0.001), 0.5)"/>
</energy_composite>
```

A normalization is not required. The usage of equation 5.5 in this way results in angular distributions similar to "Rydberg" background electrons in figure 4.1. Doppler-broadening due to the momenta of Rydberg-states in the MS also affects ${}^{\mathrm{d}\mathcal{P}}/_{\mathrm{d}E}$. The impact on the energy distribution is also mentioned in [Sch20]. Equally, the angular distribution would experience a slight broadening. Anyhow, this effect will not be included explicitly in this work: given the requirements and the uncertainties in the basic assumptions, it may be omitted.
Starting with the 6.0 G LFCS magnetic field setting, simulations of 10^5 Rydberg state-induced electrons at different retarding potentials $U_0 = \{-10.0, -18.6, -30.0\}\,\mathrm{kV}$ are executed. These settings match with simulations of monoenergetic fluxtube background, figure 5.4. The resulting

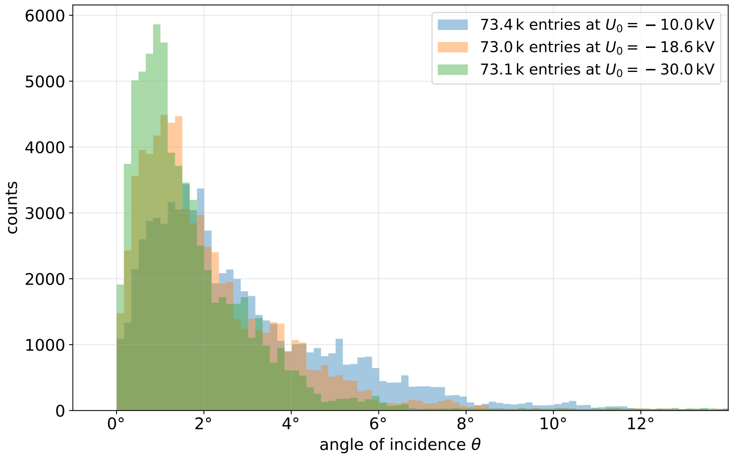

Figure 5.5.: Angular distributions of Rydberg-mediated background at 6.0 G LFCS setting: The binned number of electrons is plotted over the angles of incidence θ (pitch angle) they are hitting the reference surface with. 10^5 Rydberg-mediated electrons are generated for each setting of U_0. Only electrons that terminate on the virtual pTEF surface at z_0 are contained in the histograms.

angular distributions of the virtual pTEF-terminated electrons is provided in figure 5.5, exhibiting comparable behavior as stated in [G+22] with figure 4.1: the distributions show a peak in the low-angle regime, roughly below 2°, and a strong decrease towards large angles $\mathcal{O}(10°)$. For further usage of the findings from such background simulations, it is useful to provide a continuous angular PDF ${}^{\mathrm{d}\mathcal{P}}/_{\mathrm{d}\theta}(\theta)$. This is why many functions with a small number of parameters have been considered for fitting of the angular distributions, of which the gamma distribution turned out to be a proper candidate.

The gamma distribution's PDF [Z+20] is often written as

$$\frac{\mathrm{d}\mathcal{P}}{\mathrm{d}x}(x; a, b) = \frac{b^a}{\Gamma(a)}\, x^{a-1} \mathrm{e}^{-bx}. \tag{5.6}$$

The two parameters are the inverted scale parameter b and the shape parameter a. It can be shown that the expectation value of a gamma-distributed random variable X according to equation 5.6 is $E(X) = {}^{a}/_{b}$. Integration also allows to determine the probability $\mathcal{P}$, that X takes on a value in the range $[x_1, x_2]$:

$$\mathcal{P}(x_1 \leq X \leq x_2) = \frac{b^a}{\Gamma(a)} \left[-\frac{1}{b^a}\Gamma(a, bx)\right]_{x_1}^{x_2} = \left[\frac{\gamma(a, bx)}{\Gamma(a)}\right]_{x_1}^{x_2}, \tag{5.7}$$

where $\Gamma(a, bx)$ is the incomplete gamma distribution of the lower and $\gamma(a, bx)$ of the upper boundary [OMS09]. The rightmost fraction of both functions is also known as regularized incomplete gamma function of the upper boundary, which characterizes the cumulative density of gamma distributed quantities.

For fitting of the angular distributions, an upper cutoff θ_{cut} will be applied to the angles, corresponding to the definition of an angular ROI $[0, \theta_{\mathrm{cut}}]$. This improves the fit, since the number of bins with single counts (or generally low statistics) is drastically reduced in the range of large angles where the gamma distribution will therefore not describe the behavior properly. However, both the actual angular distribution and the gamma distribution only yield very small frequencies in this regime with negligible effect.

For the first pTEF campaign, a larger number of settings is desired. Hence, the simulations are

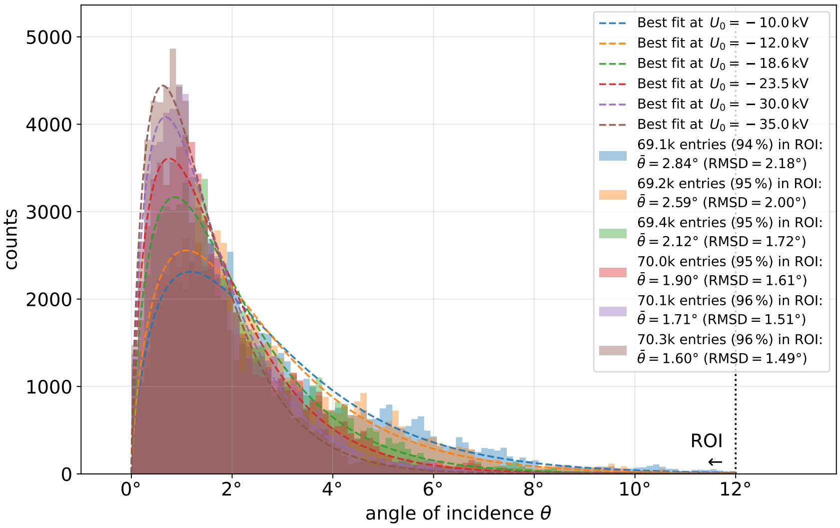

Figure 5.6.: Angular distributions and PDF fits of Rydberg-mediated background at 6.0 G LFCS setting: The binned number of electrons is plotted over their pitch angle θ (similar to fig. 5.5). 10^5 Rydberg state-induced electrons are initialized for each setting. The fits for the PDFs ${}^{\mathrm{d}\mathcal{P}}/_{\mathrm{d}\theta}(\theta)$ with the gamma distribution (eq. 5.6) are also shown (parameters in tab. 5.1).

Table 5.1.: Parameters of the Rydberg-mediated background angular distributions: The parameters a and b are resulting from the fit (ROI ranging up to $\theta_{\text{cut}} = \{16°, 14°, 12°\}$ for increasing B_{min}) of the simulations' results with eq. 5.6.

LFCS setting	2.7 G			4.0 G			6.0 G		
$-U_0$ in kV	10.0	18.6	30.0	10.0	18.6	30.0	10.0	18.6	30.0
a	1.675	1.683	1.667	1.720	1.699	1.722	1.746	1.750	1.757
b	0.428	0.588	0.739	0.505	0.678	0.889	0.637	0.872	1.119
σ_a	0.01214	0.0118	0.0118	0.015	0.014	0.014	0.016	0.016	0.015
σ_b	0.005	0.006	0.008	0.006	0.009	0.010	0.009	0.0107	0.014
$\sqrt{\mathrm{cov}_{ab}}$	0.007	0.008	0.009	0.009	0.010	0.0105	0.0107	0.01217	0.014
LFCS setting	2.7 G			4.0 G			6.0 G		
$-U_0$ in kV	12.0	23.5	35.0	12.0	23.5	35.0	12.0	23.5	35.0
a	1.678	1.666	1.671	1.714	1.700	1.699	1.775	1.732	1.752
b	0.470	0.652	0.800	0.554	0.769	0.940	0.715	0.977	1.209
σ_a	0.012230	0.0110	0.0116	0.015	0.014	0.014	0.017	0.015	0.015
σ_b	0.005	0.007	0.008	0.006	0.009	0.0105	0.009	0.01126	0.014
$\sqrt{\mathrm{cov}_{ab}}$	0.008	0.008	0.009	0.010	0.010	0.01120	0.0115	0.012018	0.014

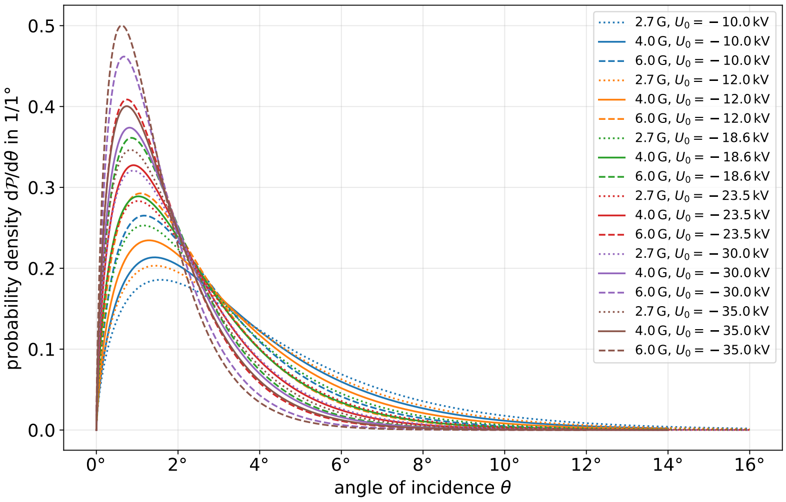

Figure 5.7.: Angular PDF $\mathrm{d}\mathcal{P}/\mathrm{d}\theta(\theta)$ fits of Rydberg-mediated background at various settings: The fits of eq. 5.6 to simulated data for several LFCS and retarding potential U_0 settings are displayed (parameters in tab. 5.1). Note the applied fitting ROI $\theta_\mathrm{cut} = \{16°, 14°, 12°\}$ for increasing B_min.

extended to two more LFCS settings, 4.0 G and 2.7 G. The XML configurations are found in appendix B. To comply with eventual retarding voltages apart from the formerly used ones, $U_0 = \{-12.0, -23.5, -35.0\}$ kV are also included in the simulations. In total, these simulations cover a sufficient configuration space of $3 \times 6 = 18$ settings. The resulting fit parameters are listed in table 5.1. Proper normalization must be ensured when utilizing the parameters for the PDF in the ROI. The angular distributions for all retarding voltages in the 6.0 G setting are displayed in figure 5.6, also containing the fits with equation 5.6 in the ROI. For the two remaining LFCS settings, the results are similarly provided in figure B.4 (appendix B). The mean pitch angles $\bar{\theta}$ and root-mean-square deviations (RMSDs) of the entries are also stated in figure 5.6 and B.4.

For the sake of completeness, the resulting PDFs $\mathrm{d}\mathcal{P}/\mathrm{d}\theta(\theta)$ for all settings are shown in figure 5.7, allowing for a direct normalized comparison of the fields' effect. Also, table 5.1 is consulted to compare the settings. Most noticeable is the dependence of the inverted scale parameter b on the voltage U_0: it increases with stronger electrostatic boosts qU_0, meaning that the distribution is less spread out and compressed towards $\theta = 0$, reflected in decreasing mean pitch angles $\bar{\theta}$ (to be read in figure 5.6 and B.4). This behavior is expected from the formerly explained shift towards lower angles, as $E_\parallel$ grows. There are no significant differences in the shape parameter a for fixed LFCS setting, while a slight increase is found as the minimum magnetic field strength B_min varies from 2.7 G to 6.0 G, causing the mean pitch angle to decrease noticeably. This can be explained with the MAC-E effect: lower B_min corresponds to better energy resolution due to stronger collimation. The pitch angle change scales with the magnetic gradient. This is why electrons with higher final pitch angles are more likely to be found for lower values of the minimum magnetic field (see eq. 3.4).

5.2.2. Characterization of Radon-induced Background

In section 3.3.2, radon is discussed as background source in the KATRIN experiment. Due to its long half-life, ^{222}Rn is ruled out for decays in the sensitive fluxtube volume during vacuum operation, which is not supposed to diminish its relevance in the deposition mechanism of ^{210}Pb. Comparison of typical removal times and the half-lifes of ^{219}Rn and ^{220}Rn allow to focus on the first isotope in the scope of this work. The second information that is required to simulate

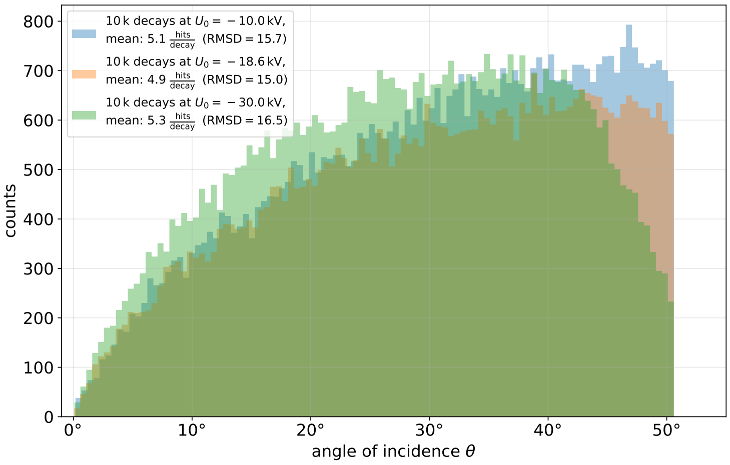

Figure 5.8.: Angular distributions of radon-induced background at 6.0 G LFCS setting: The binned number of events is plotted over the angles of incidence θ (pitch angle) they are hitting the reference surface with. Electrons originating from 10^4 ^{219}Rn decays are contained within each histogram (different retarding potentials U_0), provided a termination on the virtual pTEF surface at z_0.

radon-induced background is an energy distribution. Very different processes and energy scales come into play for subsequent electron emission from radon decays, as figure 3.8 points out. Secondary production due to typical stored electrons in the case of radon-induced background will also occur and contribute to the results.

Kassiopeia offers a dedicated energy generator for radon. It allows to set the atomic mass number for radon-219 and include the complex electron-emitting processes, described in [Wan13, Har15]. In the `ksgen_generator_composite`, the energy creation is adjusted to use this generator:

```
<!-- energy creation -->
<energy_composite>
        <energy_radon_event force_shake_off="false" force_conversion="false" do_shake_off="
            true" do_conversion="true" do_auger="true" isotope_number="219"/>
</energy_composite>
```

This way, shake-off and internal conversion electrons are generated as well as Auger electrons from atomic relaxation and shell reorganization electrons (ref. [Wan13]).

Apart from that, the simulations are similar to the Rydberg state-induced case in the previous section 5.2.1 but far more time-consuming due to the long storage times (sec. 3.3.1). There is an important difference in the events' multiplicity: each radon event can induce many electrons propagating towards the FPD. Consequently, the same statistic level can be reached with a smaller number of initialized events. For the beginning, 10^4 decays for the three retarding potentials $U_0 = \{-10.0, -18.6, -30.0\}$ kV at 6.0 G LFCS setting are simulated. The corresponding angular distributions are provided in figure 5.8. Smaller angles due to the electrostatic boost are again observable. The distribution at −30.0 kV differs significantly from the two other ones, as the high angle flank towards $\theta_{\max}$ is not as steep. Mean values and deviations of the pitch angles for the three settings are stated in figure 5.9.

Figure 5.9 also contains the distributions for the remaining setpoints of $U_0 = \{-12.0, -23.5, -35.0\}$ kV. Due to the computational expense, they are carried out with reduced statistics of 4×10^3 events. In addition, a fit is included for each distribution. Within this work, the relation

$$\frac{\mathrm{d}\mathcal{P}}{\mathrm{d}\theta}(\theta; \alpha, \beta) = \mathcal{N}\,\theta^{\alpha}(\theta_{\max} - \theta)^{\beta} \quad (0 \leq \theta \leq \theta_{\max}) \tag{5.8}$$

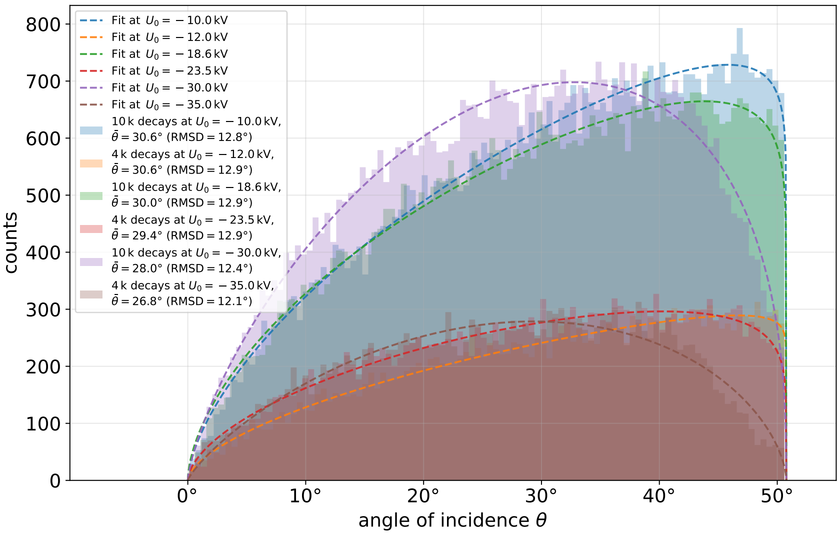

Figure 5.9.: Angular distributions and PDF fits of radon-induced background at 6.0 G LFCS setting: The binned number of electrons is plotted over their pitch angle θ (similar to fig. 5.8). 10^4 (4×10^3) ^{219}Rn decays are initialized for the three upper (lower) curves. The fits with equation 5.8 are also displayed (parameters in tab. 5.2).

Table 5.2.: Parameters of the radon-induced background angular distributions: The parameters α and β are resulting from the fit (ROI ranging up to $\theta_{\text{max}} = 50.77°$) of the simulations' results with eq. 5.8.

LFCS setting	2.7 G			4.0 G			6.0 G		
$-U_0$ in kV	10.0	18.6	30.0	10.0	18.6	30.0	10.0	18.6	30.0
α	0.677	0.684	0.805	0.652	0.668	0.842	0.631	0.591	0.733
β	0.060	0.079	0.287	0.058	0.095	0.390	0.069	0.094	0.402
σ_α	0.016	0.016	0.017	0.016	0.016	0.018	0.012	0.014	0.014
σ_β	0.008	0.008	0.010	0.008	0.008	0.0115	0.007	0.008	0.010
$\sqrt{\text{cov}_{\alpha\beta}}$	0.010	0.010	0.0113	0.010	0.010	0.013	0.008	0.009	0.0104
LFCS setting	2.7 G			4.0 G			6.0 G		
$-U_0$ in kV	12.0	23.5	35.0	12.0	23.5	35.0	12.0	23.5	35.0
α	0.707	0.666	1.01	0.674	0.685	1.01	0.607	0.582	0.81
β	0.086	0.083	0.575	0.075	0.145	0.666	0.053	0.152	0.595
σ_α	0.023	0.024	0.03	0.0221	0.023	0.03	0.0217	0.021	0.03
σ_β	0.011	0.012	0.020	0.011	0.01211	0.022	0.0108	0.0122	0.021
$\sqrt{\text{cov}_{\alpha\beta}}$	0.014	0.015	0.021	0.014	0.015	0.0221	0.014	0.014	0.021

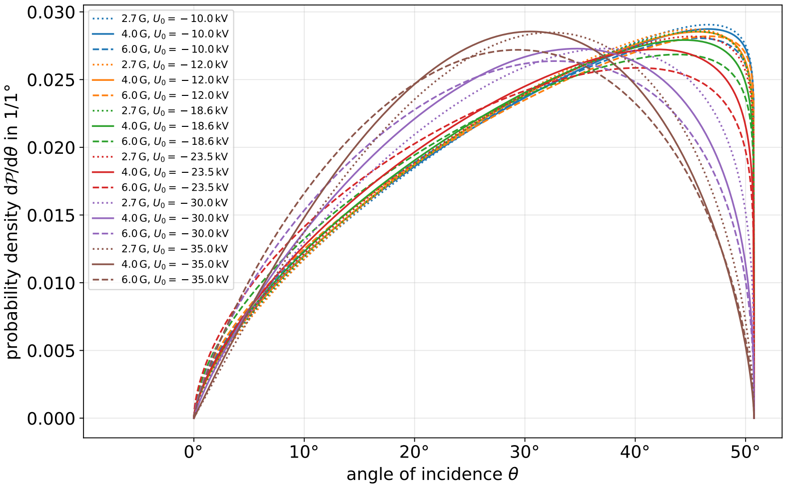

Figure 5.10.: Angular PDF $\mathrm{d}\mathcal{P}/\mathrm{d}\theta(\theta)$ fits of radon-induced background at various settings: The fits of eq. 5.8 to simulated data for several LFCS and retarding potential U_0 settings are displayed (parameters in tab. 5.2).

is proposed as an applicable form for the angular PDF of radon-induced electrons and is used for these fits. The normalization $\mathcal{N}$ depends on the limits of the function's domain (of positivity) $[0, \theta_{\max}]$ and the parameters α and β. These parameters are serving to control the function's curvature in the regime of small ($\theta \sim 0 \longrightarrow \alpha$) and large ($\theta \sim \theta_{\max} \longrightarrow \beta$) angles. Integration of the right-hand side of equation 5.8 right-hand side, omitting the normalization constant, can be achieved by using the Chebyshev integral:

$$\int x^{\alpha}(1-x)^{\beta}\,\mathrm{d}x = \mathrm{B}(x; 1+\alpha, 1+\beta) + \text{const.} \tag{5.9}$$

$\mathrm{B}(x; p, q)$ is the incomplete beta function with the domain $x = [0, 1]$, coinciding with the complete beta function for $x = 1$ [OMS09]. Applying this integral to equation 5.8, the relation

$$\mathcal{P}(\theta_1 \leq \theta \leq \theta_2) \propto \left[\theta_{\max}^{1+\alpha+\beta}\,\mathrm{B}\left(\frac{\theta}{\theta_{\max}}; 1+\alpha, 1+\beta\right)\right]_{\theta_1}^{\theta_2} \tag{5.10}$$

is obtained for the probability $\mathcal{P}$ of the considered interval $[\theta_1, \theta_2]$.

By means of this angular PDF, radon-induced background can also be investigated regarding its interaction with TEFs. Despite their aim is not the characterization of radon-induced background, the fits from simulations allow for the consideration of these contributions in measurements of the remaining background. To also provide the distributions for the two remaining LFCS settings of 2.7 G and 4.0 G from the previous section, these simulations are carried out analogously. The resulting distributions with fits are displayed in figure B.5 (appendix B) for the sake of completeness. The mean pitch angles $\bar{\theta}$ and RMSDs of the entries are also stated in figure 5.9 and B.5. For each of the 18 settings in total, the parameters are listed in table 5.2.

A comparison of the overall behavior is made possible with the display of the normalized PDFs $\mathrm{d}\mathcal{P}/\mathrm{d}\theta(\theta)$ in figure 5.10. The deviation of the large angle flank for $qU_0 \geq 30$ keV is striking. For $qU_0 \lesssim 23.5$ keV the PDFs somewhat resemble the beta electrons' angular distribution (fig. 4.1).

The level of radon can be tuned by warming or cooling of the baffles. This corresponds to changing the composition of background electrons, as the major component of background (electrons of remaining background) will be accompanied by increasing amounts of radon-electrons, the higher the baffle temperature gets. Increasing the spectrometer pressure will shorten the interarrival times of radon-induced secondaries to enable their identification by means of the characteristic non-Poissonian behavior of stored particle background. In [HHL21], achievable investigation of filtering properties for radon-induced electrons with large pitch angles is stated. Consequently, radon-induced electrons provide an approach to the truly high-pass filtering properties of the pTEF without requiring beta electrons in the first place.

5.3. Studies of the pTEF's geometric Systematics and Filtering Properties

Prior to the fabrication and installation of the pTEF, aspects of the geometry are investigated for an estimation of systematic effects (section 5.3.1). Furthermore, its filtering properties have to be studied. These are being simulated in section 5.3.2.

5.3.1. Geometric Aspects and Systematics of the (2)pTEF

For purely geometric investigations without actual propagating electrons like in the previous sections, estimation of the structure's OAR is the main task. Recall the maximum transmission of $\xi_{\text{max}} = \text{OAR}$ for $\theta = 0$ (eq. 5.3), similar to the structures shadow under normally incident parallel lighting. Actually, the OAR depends on the viewing angle onto the structure, which is composed of both polar and azimuthal angle. The first is equal to $\theta_z \simeq \theta$ in KATRIN coordinates, whereas the latter describes the rotation of the honeycomb grid by φ around the z-axis. Taking this dependences into account, we will write $\text{OAR}(\theta, \varphi)$, while just OAR is used for the case of $\theta = 0$.

An analytic approach to $\text{OAR}(\theta, \varphi)$ for small pitch angles θ is pursued but will not be addressed in this work. Instead, the full angular range is covered with numerical evaluation of the OAR based on geometric objects using *Python* code. The periodic structure of the honeycomb grid can be investigated by using one representative hexagonal channel. For the single-layered pTEF, let the surface covered by an entire hexagonal cell with half of the bridge A_{cell}, i.e. the area at a normal viewing angle $\theta = 0$. Independent of φ, the projected area $A_{\text{cell}}(\theta)$ of this hexagon from different viewing or pitch angles is simply $A_{\text{cell}} \cos(\theta)$, whereas the walls come into vision $\propto \sin(\theta)$. The $\text{OAR}(\theta, \varphi)$ is determined by subtraction of the six inner walls' contributions $A_{\text{w},j}(\theta, \varphi)$ ($j = 1, \ldots, 6$) from the open area, the hexagonal channel's deck area ($A_{\text{hex}} \cos(\theta)$) with side length a and normalization to the overall area $A_{\text{cell}}(\theta)$. In total, it is evaluated via

$$\text{OAR}(\theta, \varphi) = \frac{A_{\text{hex}} \cos(\theta) - \sum_j A_{\text{w},j}(\theta, \varphi)}{A_{\text{cell}} \cos(\theta)}. \tag{5.11}$$

It is important that only contributions of the walls that are visibly lying within the channel are considered in $A_{\text{w},j}(\theta, \varphi)$. Otherwise, $A_{\text{w},j}(\theta, \varphi) = 0$. A maximum of three walls contributes at the same time. For an illustration it should be referred to figure B.6 (appendix B), where the setup is illustrated and the contributions of the walls become evident.

The Python package *Shapely* is used to generate a virtual two-dimensional projected version of the pTEF by implementation of the channel edges and walls as `Polygon` objects. Virtual rotation (z-axis) and tilting around the y-axis are also made possible. Shapely contains methods to obtain shape objects that are actually differences or unions of other shapes. Moreover, the surface area of a transformed shape can easily be accessed. In consequence, the terms in equation 5.11 are found by applying the required angular transformations and, for the channel walls, cuts on the `Polygon` objects.

In addition to the single channel of the pTEF grid, a second layer of multiple honeycombs is added in a distance of $\Delta z = 500\,\mu\text{m}$ "below" (z-direction) the single hexagon. This even allows to

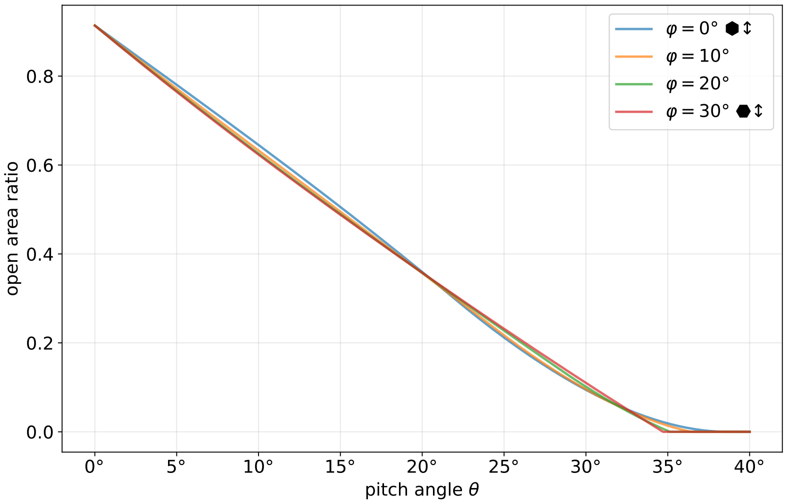

Figure 5.11.: OAR of the pTEF under different angles: The OAR is plotted over the pitch angle θ of the pTEF with parameters from eq. 5.1. The four distinct graphs account for the azimuthal rotation (angle φ) of the structure with respect to the pitch direction, slightly affecting the OAR.

determine OAR(θ, φ) of the 2pTEF. Again, figure B.6 (appendix B) serves to illustrate the setup. In case of the 2pTEF, equation 5.11 would require additional terms for the second layer, of course. The less complex pTEF features an OAR < 1 at $\theta = 0$ already due to the finite wall thickness b (fig. 5.1). The walls do not contribute and equation 5.11 becomes

$$\mathrm{OAR} := \mathrm{OAR}(\theta = 0) = \frac{A_\mathrm{cell}}{A_\mathrm{hex}} = \xi_\mathrm{max}. \tag{5.12}$$

This maximum transmission, the OAR of the pTEF, is

$$\xi_\mathrm{max} = \frac{A_\mathrm{hex}}{A_\mathrm{cell}} = \frac{a^2}{\left(a + \frac{b/2}{\sqrt{3}/2}\right)^2} = \left(1 + \frac{b}{\sqrt{3}a}\right)^{-2} = 91.365\,\%, \tag{5.13}$$

where the side length of the cell (including thickness b of the walls) is employed for A_cell. The evolution of OAR(θ, φ) up to total coverage is provided in figure 5.11 for four azimuthal cases $\varphi = \{0°, 10°, 20°, 30°\}$. Sixfold rotational symmetry of the pTEF allows to limit on this azimuthal domain, where $\varphi = 0$ corresponds to the normal configuration with a hexagon corner pointing upwards (x-direction). The OAR decreases almost linearly with θ, until total coverage is reached at different angles, depending on φ. It is found that the normal configuration has a slightly higher OAR compared to the others in the relevant regime of small pitch angles θ. A rough estimation of the pitch angle-dependent transmission $\xi(\theta)$ for electrons can be made based on OAR(θ) (mean with respect to φ due to random gyration phases). The larger θ, the more is the OAR expected to deviate from the actual value of ξ. For the expected precision of ~1° in the alignment, the OAR is OAR$(\theta = 1°) = \{0.887, 0.885, 0.884, 0.883\}$, corresponding to a relative loss of 3.0 % – 3.4 % compared to the ideal case.

Similar investigations are carried out for the 2pTEF. While the pTEF's OAR might just be reduced by a tilt of the structure, which is characterized completely by (θ, φ), a much broader configuration space comes into play if a 2nd pTEF layer is introduced (like in fig. 5.3) behind the 1st one. On the one hand, translational misalignment of the 2nd grid might occur in both x- and y-direction with respect to the 1st. Also, the distance Δz could be affected. On the other hand, rotational misalignment could be introduced due to a relative tilt or rotation of both layers.

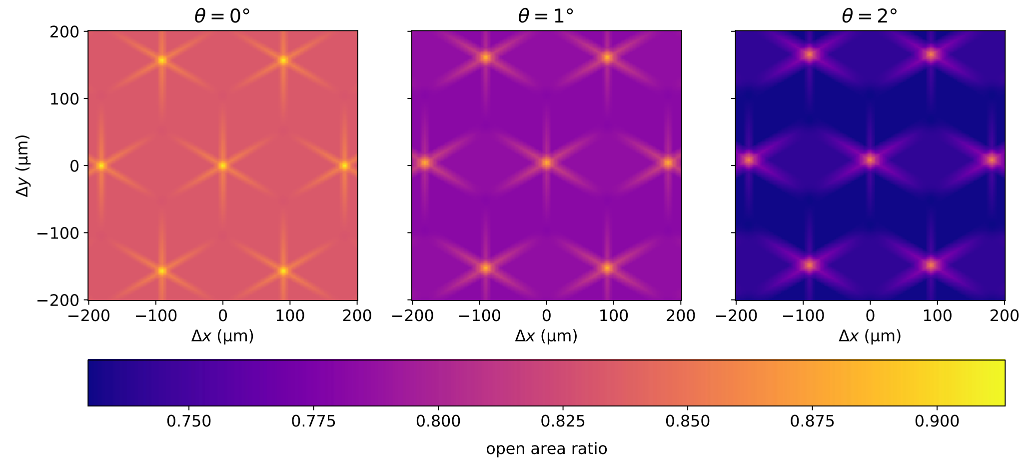

Figure 5.12.: OAR of the 2pTEF under relative shifts of both layers at different pitch angles θ: The OAR is plotted over the shifts Δx and Δy of the 2^{nd} pTEF layer in x- and y-direction. Normal azimuthal orientation $\varphi = 0$ is chosen, 2pTEF dimensions are as in eq. 5.1 and 5.2. Each of the three plots represents another pitch angle $\theta = \{0°, 1°, 2°\}$.

The rotational systematics are not investigated further here. By means of the holding structure, relative tilts are suppressed to a high degree. Moreover, it prohibits Δz to deviate much from its design value. The relative rotation is supposed to be 60° (fig. 5.3). Thanks to the boreholes and an otherwise occuring Moiré pattern, it can be tuned very precisely to this value. However, an implementation for calculations of the OAR as in the former case would not be possible due to the lack of periodicity on the single cell's size scale.

The remaining parameters of translational misalignment Δx and Δy as well as the rotational one, the pitch angle of the entire 2pTEF, are thus varied and studied regarding their effect on the OAR. Normal orientation $\varphi = 0$ is chosen. For x- and y-shifts of ±200 µm that exceed $a = 150\,\mu\text{m}$, the OAR is plotted over the entire configuration space for three small pitch angles $\theta = \{0°, 1°, 2°\}$ in figure 5.12. The analogy of of the grids manifests itself in periodicity of the pattern, caused by repeating matches of the distinct layers' channels. Under shifts that exceed the order of the bridge width b, a continuum of of constant OAR($\Delta x, \Delta y$) takes over, as the entire fork where three neighboring cells of the 2^{nd} grid join lies within the open area $A_{\text{hex}}(\theta)$. Furthermore, the central maximum of the OAR is shifted into positive y-direction, because the lower grid has to be matched perfectly from the tilted viewing angle by a shift of $\Delta y = \{0, 4.4, 8.7\}\,\mu\text{m}$ (for the three pitch angles) upwards. The corresponding maxima of the distinct plots are $\text{OAR}_{\text{max}} = \{0.914, 0.887, 0.860\}$, reduced into the described continuum $\text{OAR}_{\text{min}} = \{0.831, 0.780, 0.730\}$ by roughly 10 %, if the translational misalignment significantly exceeds the order of b in some directions.

5.3.2. Filtering Properties for Rydberg-mediated Background and Beta Electrons

When it comes to the pTEF's filtering properties in terms of the actual transmission ξ, the former geometric studies of the OAR serve as an approach for low-angle particles like the Rydberg state induced electrons. However, the previous section revealed significantly different OARs in case of electrons with $\theta \approx 0$ and such with only a few degrees $\theta < 10°$. Figure 4.2 indicates two important quantities regarding transmission: the pitch angle θ and the gyroradius r_g. The inner radius of a channel is $r_{\text{in}} = \sqrt{3}/2 \cdot a$. However, $r_g > r_{\text{in}}$ is not a necessary condition for termination in the structure: if the electron does not make a full gyration turn in the channel, it could be transmitted anyway. If this is the case depends on the momentum $p_{\parallel}$ (or velocity $v_{\parallel}$) in parallel direction to $\vec{B}$

and the gyration period T_g.
The momentum p of an electron with total energy $\gamma m_e = m_e + E$ is obtained from the relativistic energy relation

$$\gamma m_e = m_e + E = \sqrt{m_e^2 + p^2} \tag{5.14}$$

$$\implies p = \sqrt{2 m_e E + E^2}. \tag{5.15}$$

Setting qU_0 for the kinetic energy E of an electron produced in the MS downstream the AP, the transverse momentum is therefore for example

$$p_\perp = p_\perp(\theta, U_0) = \sqrt{qU_0(qU_0 + 2m_e)}\sin(\theta), \tag{5.16}$$

allowing for a estimation of $r_g = r_g(\theta, U_0; B)$ in equation 4.1. On the other hand, the parallel momentum is just $p_\parallel = p\cos(\theta)$. In analogy to equation 5.14, the relativistic momentum of an electron with velocity v can be written as $p = \gamma m_e v$. Using the energy relation above and $\beta := {}^{v}\!/_{c} = v$,

$$p = \beta \cdot (m_e + E) \implies v = \frac{\sqrt{1 + 2\frac{m_e}{E}}}{1 + \frac{m_e}{E}} \tag{5.17}$$

is obtained. In the non-relativistic case $x := {}^{E}\!/_{m_e} \ll 1$, the kinetic energy $E = {}^{1}\!/_{2} m_e v^2$ can indeed be derived from this form of v (omitting $\mathcal{O}(x^{3/2})$). With equation 2.23, the gyration length ℓ_g of one period $T_g = f_g^{-1}$ is

$$\ell_g(\theta, U_0; B) = \frac{v_\parallel}{f_g} = 2\pi \frac{m_e + E}{eB} \frac{\sqrt{1 + 2\frac{m_e}{E}}}{1 + \frac{m_e}{E}} \cos(\theta) \tag{5.18}$$

$$= 2\pi \sqrt{1 + 2\frac{m_e}{e|U_0|}} \frac{|U_0|}{B} \cos(\theta) =: \ell_{g,0}(U_0; B)\cos(\theta). \tag{5.19}$$

For example, at $U_0 = -18.6\,\mathrm{kV}$ the gyration length is $\ell_{g,0}(B) \cdot B = 2.916\,\mathrm{mm\,T}$. At the pTEF position z_0 in the detector magnet, where $B \approx 2.5\,\mathrm{T}$ [HHL21], electrons with $\theta < 10°$ feature gyration lengths above 1.1 mm, corresponding to a quarter gyration period in the channel, with a gyroradius of $r_g \leq 30\,\mu\mathrm{m}$ (eq. 4.1).
For different energies and pitch angles, both $\ell_g(\theta, qU_0)$ and $r_g(\theta, qU_0)$ are plotted in figure 5.13 for $B = 2.5\,\mathrm{T}$ (pTEF position). In addition, the minimum transmission ξ_{min} of the pTEF is provided in figure 5.13c. This quantity can be evaluated by assuming $\ell_g \leq d$, so that at least one full period fits within the channel length. If r_g exceeds the channels' inner radius r_{in}, the lower boundary for the transmission is of course $\xi_{\mathrm{min}} = 0$, because the spiral intersects the walls. In other cases where $r_g < r_{\mathrm{in}}$, the transmission probability is determined statistically by a homogeneous spatial distribution of the electrons in the x-y-plane from the OAR. However, this lower boundary should be significantly lower than ξ, because ℓ_g is actually much larger than d. A direct approach to the actual transmission and systematic effects are simulations of electrons in the magnetic field, that interact with the structure. These are carried out using Kassiopeia.

The simulations mainly address the 2pTEF, which is originally the candidate for the first pTEF campaign. As in section 5.2, a simulation is configured to generate electrons propagating towards an object at z_0. Different from the planar disk surface in section 5.2 (a virtual pTEF only serving as termination condition), an actual 2pTEF configuration is introduced in the beamline. The geometry of the honeycomb grid, created by Dominic Hinz and Yvonne Schätzle [Sch21], is built iteratively from identical `extruded_poly_loop_space` objects, representing a wall of one cell

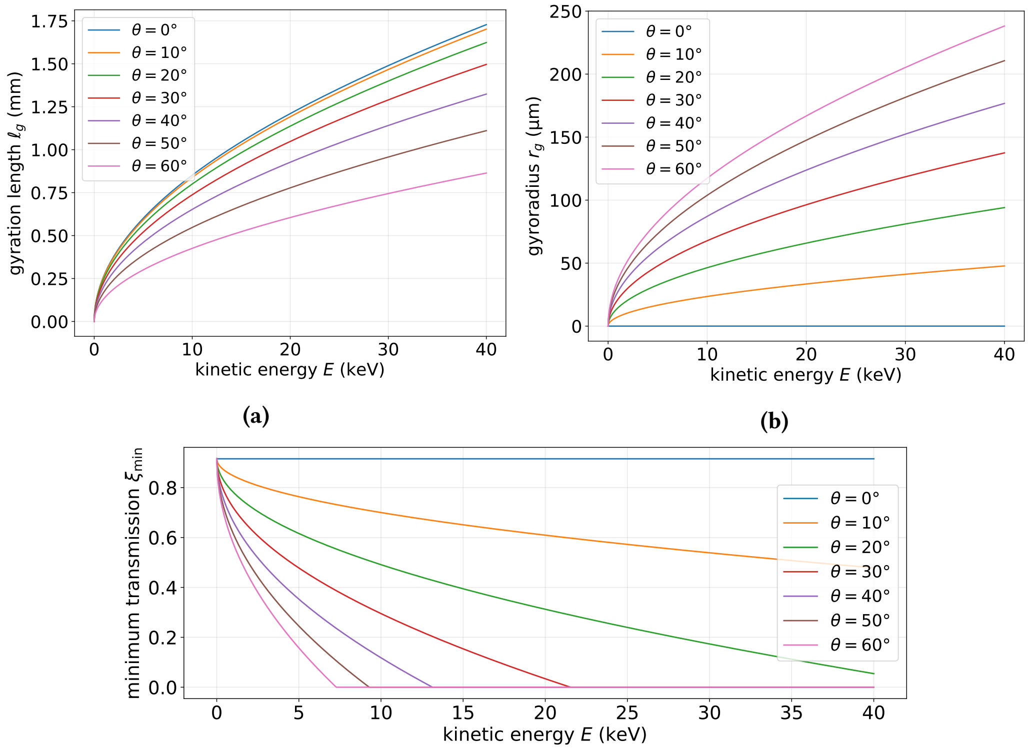

(a) **(b)**

(c)

Figure 5.13.: Gyration parameters of electrons at the pTEF: In the center of the detector magnet, the magnetic field strength is $B \approx 2.5\,\mathrm{T}$ [HHL21]. Parameters of the electrons' motion are determined and displayed. Figure a: The gyration length ℓ_g of one gyration period T_g is plotted over the electron energy E for different pitch angles θ. Figure b: Corresponding gyroradius r_g over E. Figure c: The minimum transmission $\xi_{\min}$ is estimated from the cyclotron trajectory's radius r_g, the inner diameter $\sqrt{3}a$ of the channels and the pTEF's OAR.

each. A rectangular honeycomb mesh with the pTEF parameters from equation 5.1 is built up that way, extending to a defined height and width. However, each channel contributes with six surfaces to the entire object. With $a = 100\,\mu\mathrm{m}$ and $b = 8\,\mu\mathrm{m}$, a channel density of $n_{\mathrm{ch}} \approx {}^{32}/_{\mathrm{mm}^2}$ can be calculated for the pTEF grid, resulting in a rapidly increasing number of tiny surfaces in the simulation even for grid sizes of some square millimeters. In addition, the perforated front and back surfaces of the grid are included for particle tracking.

Because a higher resolution of the trajectories is required to achieve proper behavior on the small size scale of interactions between electrons and pTEF, the adiabatic trajectory can not be used. Instead, an exact trajectory `kstraj_trajectory_exact` is applied with a cyclotron control length of ${}^{\ell_g}/_{30}$ and another independent control length fixed to $1\,\mu\mathrm{m}$:

```
<!-- exact trajectory -->
<kstraj_trajectory_exact name="trajectory_exact_ptef">
  <integrator_rk8 name="integrator_rk8"/>
  <term_propagation name="term_propagation"/>
  <control_cyclotron name="control_cyclotron" fraction="{1. / 30.}"/>
  <control_length name="control_length" length="1.e-6"/>
</kstraj_trajectory_exact>
```

High precision in tracking comes along with computational effort. To allow for sufficient statistics in reasonable computation time, the electrons are not generated homogeneously in the MS's fluxtube volume (like in sec. 5.2). Instead, the angular distributions and energies at z_0 are used to

create electrons close before the grid. Similarly, transmitted electrons are terminated close behind the structure, since they do not provide further useful information.
That way, Rydberg-state induced background electrons and electrons from tritium beta decay (referred to as beta or signal electrons) are studied regarding their transmission. Because the findings from section 5.2.1 are not available yet, a semi-empirical approach based on already established results like in figure 4.1 serves for the angular distribution of Rydberg-mediated background. It is approximated by a Gaussian distribution on the domain $[0°, 10°]$ with a maximum at $\bar{\theta} = 3°$ and a width of $\sigma_\theta = 2°$ [Sch21] which is then introduced in the `direction_spherical_composite`. The electrons are considered monoenergetic at $E = qU_0$ (no PAE voltage) and generated homogeneously within a small cylindrical volume, reaching up to a few millimeters before the 1st pTEF layer. The diameter is set to be smaller than the pTEF's side lengths, to ensure complete mapping onto the filter. 5×10^4 electrons are generated this way. Of course, just a fraction of them terminates on the 1st pTEF, while the major fraction is completely transmitted, but some electrons also terminate on the 2nd grid. They can be distinguished by the termination condition they experienced, which is also written to the ROOT file, or by the z-coordinate of termination. Thus, the background transmissions $\xi(\text{bg})$ of both 2pTEF and pTEF can be established with one common simulation. The obtained values are

$$\xi_{\text{pTEF}}(\text{bg}) = (82.0 \pm 0.4)\,\% \quad \text{and} \quad \xi_{\text{2pTEF}}(\text{bg}) = (73.6 \pm 0.4)\,\% \tag{5.20}$$

with statistic uncertainties of Poisson distributed counts with error $\sigma_N = \sqrt{N}$ [Z+20]. Recalling $\xi_{\text{max}} = 91.4\,\%$ (eq. 5.13) it is found that the few degrees above $\theta = 0$ already account for a reduction to $\xi_{\text{pTEF}}(\text{bg})$ by roughly 10 % compared to the pTEF's OAR. Moreover, the usage of a 2nd grid in the 2pTEF configuration adds about the same reduction again, which is expected in the low angle regime.
The effect of translational misalignment and pitching is investigated similar to the former section. Including the shifts of the 2nd layer in x- and y-direction, the entire configuration is additionally tilted by a certain pitch angle with the following transformation commands in the XML configuration:

```xml
<if condition="{[use_pTEF] eq 1}">
 <space name="pTEF_1" tree="pTEF_space">
 <transformation rotation_euler="0. {-[pitch]} 0."/>
 <transformation displacement="0. 0. [pTEF_z_ref]"/>
 </space>
 <if condition="{[use_2pTEF] eq 1}">
   <space name="pTEF_2" tree="pTEF_space">
   <transformation rotation_euler="0. {-[pitch_angle]} 0."/>
   <transformation displacement="[x_shift] {[y_shift]*cos([pitch])+([length]+[2pTEF_distance])*sin([pitch])} {[pTEF_z_ref]-[y_shift]*sin([pitch])+([length]+[2pTEF_distance])*cos([pitch])}"/>
   </space>
 </if>
</if>
```

Again, a wide range of shifts of the 2nd filter layer in x- and y-direction is covered. The results for the transmission are plotted in figure 5.14, wherein each Δx-Δy-bin corresponds to a simulation of 5×10^4 electrons. In the plot on the right, the resolution is twice as high (translation steps halved). Figure 5.15 provides the simulation results of the transmission for an additionally tilted structure (by pitch angle θ). The translation takes place in independent directions x (left) and y (right).
The results in figure 5.14 reproduce the OAR pattern from figure 5.12 quite well up to an overall reduction (eq. 5.20). The expected precision in alignment is < 10 µm and ~1°. While solely one

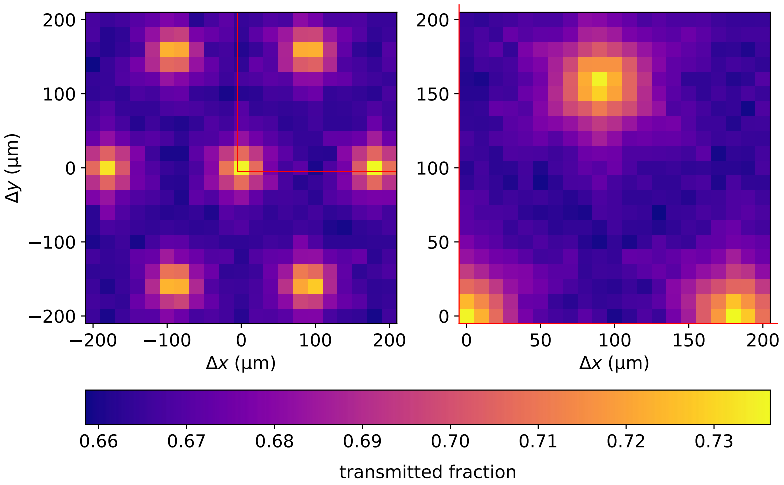

Figure 5.14.: 2pTEF transmission for background electrons with translational misalignment: Transmitted fraction of Rydberg-mediated type background electrons at different shifts of 2nd grid in x- and y-direction. Right: Higher resolution simulations of 1st quadrant (indicated with red line on the left). Each Δx-Δy-bin corresponds to 5×10^4 generated electrons.

systematic would induce an effect of about 1 %, the combination reduces the transmission by 2 % – 3 % (fig. 5.15).

Signal electrons from tritium beta decay are also generated in front of the pTEF with a linearly increasing angular distribution up to $\theta = 50°$ [Sch21], as figure 4.1 suggests. Besides of this different generator in the `direction_spherical_composite`, the simulation is equivalent to the former case. Because the pTEF suppresses high angle transmission, the SBR should be reduced drastically by this filter. This is confirmed with the simulations, yielding signal transmissions $\xi(\text{sig})$ of

$$\xi_{\text{pTEF}}(\text{sig}) = (15.2 \pm 0.2)\,\% \quad \text{and} \quad \xi_{\text{2pTEF}}(\text{sig}) = (6.9 \pm 0.2)\,\%. \tag{5.21}$$

For the pTEF, this corresponds to a reduction or scaling factor s of $s_{\text{pTEF}} = 5.39 \pm 0.10$ compared to the background case, whereas the 2pTEF causes reduction by a factor of $s_{\text{2pTEF}} = 10.7 \pm 0.4$. This shows that the filtering behavior is by no means linear. The effect of the 2nd layer obviously carries much information about the trajectories' shape and thus the pitch angle distribution.

Investigations of systematic effects are carried out identically to the case for background electrons. The corresponding transmission plots are provided in figures 5.16 (only translational misalignment) and 5.17 (with rotational misalignment). It is striking that the pattern for shifts is a somehow inverted version of the OAR pattern or the background case: optimal coverage (maximum OAR) of both layers features the lowest transmission. Instead, shifting the 2nd grid into the "continuum" of OAR_{min} (see sec. 5.3.1) with worst alignment results in a slightly enhanced transmission. However, this cyclotron effect of trajectories curving through the channels of the distinct plates is a geometric phenomenon and induces a change of < 1 % in the overall transmission, but the relative effect is significant (eq. 5.21). In contrast, the rotational alignment has a no relevant effect in the expected ~1° range of achievable precision.

Altogether, the filtering properties of the 2pTEF are found to differ significantly from the pTEF only. As the pitch angles and radii increase, the reduction factor due to the 2nd layer is enhanced compared to the single pTEF setup. This makes the 2pTEF advantageous regarding information about the angular distributions of potentially different contributions to the background electrons

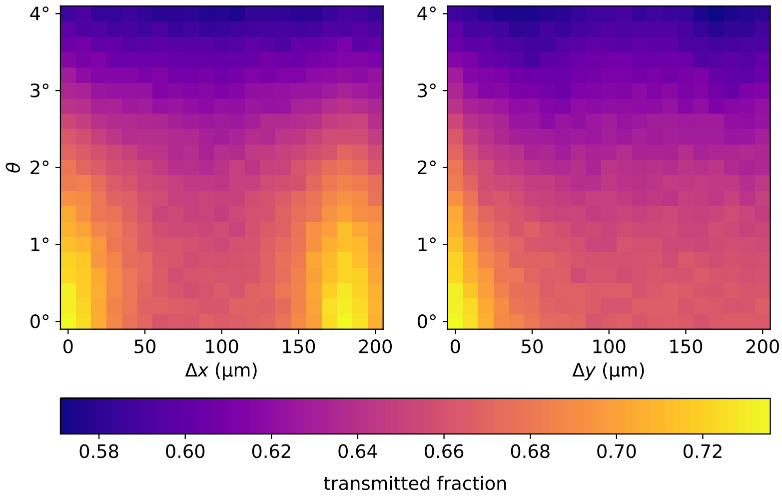

Figure 5.15.: 2pTEF transmission for background electrons with translational and rotational misalignment: Transmitted fraction of Rydberg-mediated type background electrons at different shifts of 2^{nd} grid in x- (left) and y- (right) direction. An additional rotation of the 2pTEF around the x-axis with pitch angle θ is introduced. Each $\Delta x/y$-θ-bin corresponds to 5×10^4 generated electrons.

that are filtered by the configuration. With the findings from section 5.2 and the simulation setup presented here, dedicated investigations for different compositions of the measured background can be carried out for the interpretation of experimentally acquired data (similar to [HHL21, Hin22]). Anyways, it must be taken into account that the 2pTEF requires at least 50 % more measuring time to acquire the same statistic level like the pTEF because of the segmentation. In addition, the rejected area due FPD pixels onto which the boundaries between distinct sections are mapped, increases.

A more general approach to the overall transmission $\tilde{\xi}(\text{dist.}, E)$ of the pTEF structure for arbitrary pitch angle distributions (dist. = $\mathrm{d}\mathcal{P}/\mathrm{d}\theta(\theta)$) at an energy $E = qU_0$ is the simulation of transmission for electrons with fixed initial pitch angles θ and the considered energy through the filter. From these simulations, the pitch angle- and energy-dependent (because of the gyroradius $r_g = r_g(E)$) transmission spectrum $\xi(\theta, E = qU_0)$ is obtained. Then, the transmission $\tilde{\xi}(\text{dist.}, E = qU_0)$ is

$$\tilde{\xi} = \tilde{\xi}\left(\frac{\mathrm{d}\mathcal{P}}{\mathrm{d}\theta}, U_0\right) = \int_\theta \frac{\mathrm{d}\mathcal{P}}{\mathrm{d}\theta'}(\theta')\,\xi(\theta', U_0)\,\mathrm{d}\theta' \tag{5.22}$$

in turn. Further information can be found in [Hin22], where this procedure is chosen and applied for the interpretation of the pTEF campaign.

The simulations do not include scattering of electrons off the gold surface, as an intersection of trajectory and surface directly terminates an electron. Due to the high atomic number $Z = 79$ of gold, scattering is probable. This could include on the one hand backscattering from the front of the pTEF. The electric field will accelerate them onto the structure again and transmission could take place, although originally the electron would have been filtered out. On the other hand, electrons scatter off the channels' inner walls of instead of terminating in the filter, losing an amount of their energy throughout the process. Furthermore, backscattering takes place at the FPD surface [A+21c]. Thereby reflected electrons can easily propagate up to the filter's backside and interact with the structure. The effect of scattering appears as a systematic effect on the filtering properties is subject of ongoing research.

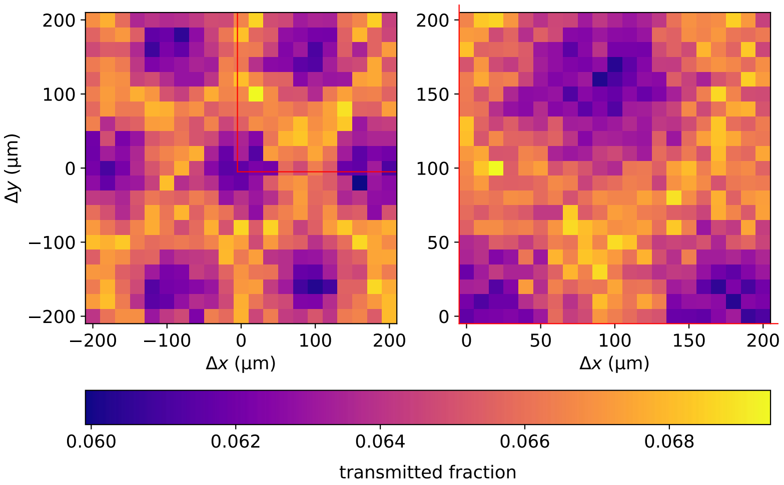

Figure 5.16.: 2pTEF transmission for signal electrons with translational misalignment: Transmitted fraction of signal-like electrons at different shifts of 2nd grid in x- and y-direction. Right: Higher resolution simulations of 1st quadrant (indicated with red line on the left). Each Δx-Δy-bin corresponds to 5×10^4 generated electrons.

The first pTEF (sec. 5.1) serves as a proof of principle for background discrimination by its low transverse energies. It should be referred to [Hin22] for results and discussion of the first campaign. From the acquired data and the simulated angular distributions with their dependence on the initial energy (distribution) of the background electrons, the background model can be reevaluated. One important point is that the surplus energy of electrons from Rydberg state ionization is mostly determined by the energy scale of the ionization mechanism. Processes apart from room temperature BBR photo-ionization can provide higher energies and affect the angular distribution [Hin22]. This clarifies the pTEF's role for a better understanding of the remaining background.

Discrimination of the remaining background to a low level for an improvement of the neutrino mass sensitivity is the ultimate goal of TEFs in the KATRIN experiment. Hence, for an application in actual beta electron measurements, the highest achievable SBR is desired, the opposite of what is achieved with the pTEF. Sensitivity of the inner channel walls to impinging electrons has to be achieved instead. This requires a grid consisting of a material wherein a detectable signal is caused by keV electrons. The etched PIN diode-based Si-aTEF is addressed in section 4.2. A scintillator-based approach, the scint-aTEF, is pursued at the KIT. In the following chapter 6 the focus will be on this potential application of the TEF principle.

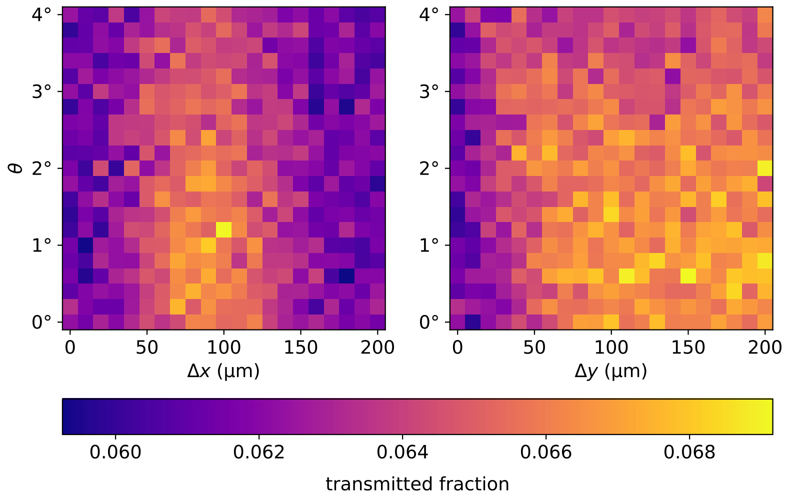

Figure 5.17.: 2pTEF transmission for signal electrons with translational and rotational misalignment: Transmitted fraction of signal-like electrons at different shifts of 2nd grid in x- (left) and y- (right) direction. An additional rotation of the 2pTEF around the x-axis with pitch angle θ is introduced. Each $\Delta x/y$-θ-bin corresponds to 5×10^4 generated electrons.

6. Research and Development of a scintillating active TEF

The novel concept of a scintillating active transverse energy filter (scint-aTEF) differs significantly from the silicon-based Si-aTEF (sec. 4.2). It aims towards electron detection via scintillation in a microstructured quadratic grid, in contrast to a detection by means of the created charged in a honeycomb structure etched into a PIN diode [G$^+$22]. Therefore, it features different geometric properties and also requires a dedicated detector for the scintillation signatures. Moreover, measures to improve the scint-aTEF's SBR and overall efficiency have to be found.
In this chapter, an introduction to scintillators and photon detectors in section 6.1 is followed by a description of the scint-aTEF setup in section 6.2, which addresses both the physical principle (sec. 6.2.1) and the simulation setup (sec. 6.2.2), which is generated using the toolkit *Geant4*. An important aspect within this section are the surface properties which are decisive for the guiding of photons within the scintillator structure. The detector setup is optimized in section 6.4. Finally, the experimental progress is outlined in section 6.5, where a test setup is also presented.

6.1. Scintillators and Photon Detection

Scintillators

Materials that are excited to luminescence by energetic ionizing particles are called scintillators. Basically, the deposited energy is transferred to excited states in the material and emitted in the form of photons afterwards. Scintillators are classified into two groups, anorganic and organic materials [Ham21]. Because various practicable processing techniques apply to (solid non-crystalline) organic scintillators, they are preferred over the frist for an application in the scint-aTEF on the one hand. In addition, backscattering of electrons is strongly favored by high atomic numbers Z of the target material (sec. 6.2). This is why anorganic scintillators are disfavored compared to organic ones, which are almost completely constituted of the low Z species hydrogen and carbon [B$^+$20]. Thus, anorganic scintillators are ruled out for the scint-aTEF and it will always be referred only to solid non-crystalline organic scintillators, i.e. plastic scintillators, in the following.
Key requirements for scintillators include high light yield, fast scintillation, transparency to the own light and long-term stability (usually implies high radiation hardness). To suffice these criteria, plastic scintillators are fabricated from different compatible components to achieve high performance. Plastic scintillators consist of a base matrix polymer, usually aromatic plastics like polystyrene or polyvinyltoluene (PVT). The steps from primary excitation to the final scintillation light are summarized in figure 6.1. An excitation of the base polymer molecules by ionizing particles diffuses through the matrix until eventually being transferred to an activator molecule via dipole-dipole interaction, causing Förster resonance energy transfer (FRET). Although the base emits light itself, it does not serve as useful scintillator in many cases, because it usually

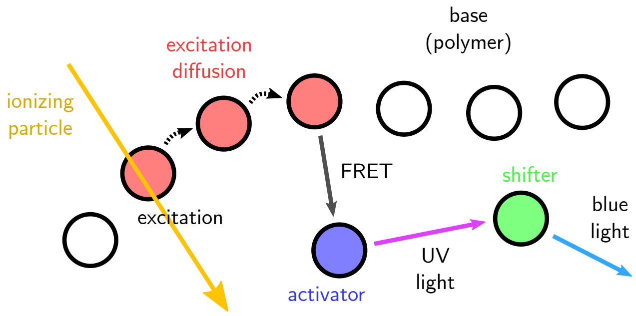

Figure 6.1.: Scintillation process in plastic scintillator (adapted from [B$^+$20]): The primary excitation of the base by an incident ionizing particle diffuses along the polymer until undergoing non-radiative transfer (FRET) to the activator. The emitted UV light is shifted to longer wavelengths (blue light) by the shifter.

has a small light yield and is opaque at its own wavelength (ultraviolet light in 300 nm regime). In these cases, an additional activator is required. Emission and absorption range of base and activator have to overlap in order to enable non-radiative collection of the polymer excitation by FRET via virtual photons. The activator, for example the widely used p-terphenyl, is a fluorescent dopant (also: fluor) added to the base by up to ~2 % of weight and acting as the primary relevant scintillating compound. It has the advantage of an increased luminescence and larger attenuation lengths due to the shifted emission spectrum (350 nm – 400 nm). Another common candidate for the primary fluor is PPO (2,5-diphenyloxazole). Usually, a third component finally shifts the light into an even more beneficial regime of typically blue to blue-green light (400 nm – 500 nm, apart from the base's absorption band), therefore increasing the attenuation length to the order of meters. This wavelength or spectrum shifter is a fluorescent molecule which is added to the plastic scintillator in small concentrations of only around 0.01 % of weight. POPOP (1,4-bis(5-phenyloxazol-2-yl)benzene) is a common agent for this purpose. Sometimes the wavelength shifter is also contained in waveguiding fibers to achieve transport of the light out of the bulk with small losses [Z$^+$18]. [M$^+$93, B$^+$20, Ham21]

For a more precise description of the fundamental mechanism of scintillation in organic scintillators it should be referred to [Bir60] and [Ham21]: In aromatic molecules, like the constituents of the materials mentioned above, the most relevant valence electrons for subsequent scintillation are typically the delocalized electrons of the π systems. These can occupy the singlet ground state S_0 and corresponding higher energy excited singlet states $S_1, S_2, \ldots$ as well as the lowest triplet state T_1 and excited triplets $T_2, T_3, \ldots$ The separation of corresponding singlet and triplet states is on the order order of ~1 eV with the triplet states being of lower energy compared to corresponding singlet states. Additionally, they have fine structures of ~0.1 eV due to the vibrational modes.

The singlet ground state S_0 can only undergo transitions directly into other singlets and vice versa, but not into triplet states. The major part of light observed in scintillation processes is created in the de-excitation of S_1 to the ground state S_0, resulting in a fast or prompt component of scintillation. In contrast, the direct $T_1 - S_0$ transition of T_1 states which are even lower in energy than S_1 is spin-forbidden and can not take place directly. Instead, triplet-triplet annihilation (TTA) provides an indirect de-excitation channel. Throughout TTA, energy transfer between two T_1 states produces a higher energetic S_1 state, while the other one is de-excited to the ground state S_0. The S_1 undergoes radiative transition to the ground state. Because TTA can thus not take place spontaneously like de-excitation of initially created excited singlets, the emitted light from the subsequent $S_1 - S_0$ transitions results in a slow or delayed scintillation component. [Ham21, Bir60, KW16]

Today, a large variety of plastic scintillators is available. They differ in performance for the respective requirements, namely the particles to be detected, their energy range and rate, environmental circumstances and the detector for the scintillation light. A key parameter for all of them is the scintillation light yield L, describing the relation between the number of produced photons and deposited energy from incident ionizing particles. It is typically on a level of $10\,{}^{\gamma}\!/_{\text{keV}}$ [Ham21] (γ will be put for photon in some cases). John Birks notes non-linearity in the scintillation yield per path length due to the non-linear energy loss ${}^{\mathrm{d}E}\!/_{\mathrm{d}x}(E)$. The empirical relation between scintillation yield L and unit path length x is known as Birks' law and reads

$$\frac{\mathrm{d}L}{\mathrm{d}x}(E) = \frac{S\,\frac{\mathrm{d}E}{\mathrm{d}x}(E)}{1 + kB\,\frac{\mathrm{d}E}{\mathrm{d}x}(E)} \tag{6.1}$$

with the scintillation efficiency S and the Birks constant kB [Bir51]. Using this relation, the absolute yield L can be computed from the path length of an ionizing particle in the scintillator and the evolution of its energy. For PVT, estimated values of kB range from $1.23 \times 10^{-2}\,{}^{\text{cm}}\!/_{\text{MeV}}$ to $2.02 \times 10^{-2}\,{}^{\text{cm}}\!/_{\text{MeV}}$, for example [Tor00, Sai21]. Birks' law accounts for quenching of the scintillation due to non-radiative de-excitations along the path that are reducing the yield to less than the expected value of $\mathrm{d}L = S\,\mathrm{d}E$ without quenching effects [Bir51, Tor00]. For charged particles like protons, alpha particles or ions the Bethe formula describes the stopping power, which is the negative mean rate of energy loss [Z⁺20]:

$$-\left\langle \frac{\mathrm{d}E}{\mathrm{d}x} \right\rangle = K\frac{z^2 Z}{A\beta^2}\left(\frac{1}{2}\ln\left(\frac{2m_e\beta^2\gamma^2 T_{\max}}{I^2}\right) - \beta^2 - \frac{\delta(\beta\gamma)}{2}\right) \tag{6.2}$$

The constant prefactor is $K = 0.307\,{}^{\text{MeV cm}^2}\!/_{\text{mol}}$, z is the incident particle's charge number and Z (A) the target's atomic (mass) number. The maximum possible energy transfer to an electron in a single collision occurs as $T_{\max}$. I is the mean excitation energy of the material, which has to be determined with much effort ($\mathcal{O}(\text{eV})$, roughly $\propto Z^{0.85}$). The incident particle's energy appears in the velocity and Lorentz factor β and γ. $\delta(\beta\gamma)$ is the so-called density effect correction. [KW16, Z⁺20] However, in the case of impinging electrons on the scintillator, the situation changes due to some properties of electrons. Also, corrections have to be made to the Bethe formula 6.2. This is required because of different kinematics and the identity of incoming and target electron. Therefore, indistinguishability, relativistic corrections and larger bremsstrahlung losses must be taken into account. From the cross section of Møller scattering (electron-electron scattering), the stopping power for electrons can be derived as

$$-\left\langle \frac{\mathrm{d}E}{\mathrm{d}x} \right\rangle = \frac{K}{2}\frac{Z}{A\beta^2}\left(\ln\left(\frac{m_e\beta^2\gamma^2}{I^2}\frac{m_e(\gamma-1)}{2}\right) + (1-\beta)^2 - \frac{2\gamma-1}{\gamma^2}\ln(2) + \frac{1}{8}\left(\frac{\gamma-1}{\gamma}\right)^2 - \delta(\beta\gamma)\right), \tag{6.3}$$

where $T_{\max}$ is replaced by ${}^{1}\!/_{2}(\gamma-1)m_e$. [Z⁺20]

With these basics of scintillation light production due to energy deposition of ionizing particles, we will move on to the actual detectable output of light. In this context, the emission spectrum and the temporal aspects of the signal are of interest. The first is mainly determined by the emission properties of the last fluor in the energy transfer chain described above, which usually shifts the light to visible wavelengths and thus out of the base's absorption range. An example for general purpose plastic scintillators are the PVT based Saint-Gobain BC-4xx scintillators (five types, identification number xx varies). The types are optimized for different applications. For example, BC-404 is developed for fast counting and excellent beta and alpha particle detection

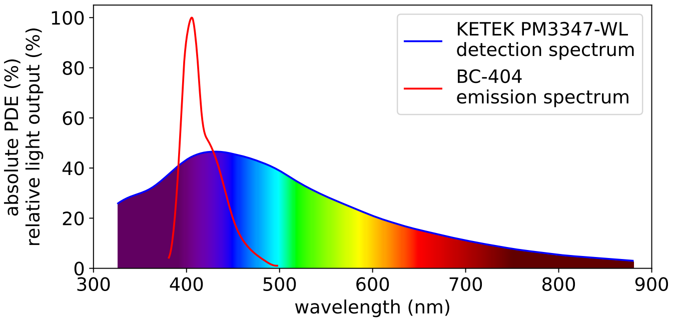

Figure 6.2.: Emission spectrum of plastic scintillator BC-404 (data from [Sai21]) and photon detection efficiency (PDE) of representative silicon photomultiplier (SiPM) (data from [KET21]): The relative light output (normalized on the value at wavelength of maximum emission 408 nm) of BC-404 is plotted over the wavelength of the scintillation light (red). The absolute PDE of the KETEK SiPM PM3347-WL operated at 5 V overvoltage is also shown (blue). Coloring below the blue curve corresponds to the wavelengths.

[Sai21], matching the requirements of the scint-aTEF on first sight. Its light output spectrum is provided in figure 6.2, ranging from the lower bound of blue to the upper limit of visible purple light. It is explained above, that different components appear in the scintillation signal of an ionized particle due to several radiative transition mechanisms. As a general form to represent the time evolution of the intensity I of scintillation light induced by an event at $t = 0$ is

$$I(t) = I_1\, f_{\mathrm{G}}(t; \tau_{\mathrm{r}})\, \mathrm{e}^{-\frac{t}{\tau_{\mathrm{p}}}} + I_2\, \mathrm{e}^{-\frac{t}{\tau_{\mathrm{d}}}} \tag{6.4}$$

with the time constants τ of the prompt (τ_{p}) and delayed (τ_{d}) de-excitations. I_1 and I_2 are the intensity factors for both components and the Gaussian function $f_{\mathrm{G}}(t; \tau_{\mathrm{r}})$ accounts for a finite rise time τ_{r} of the pulse due to the occupation of the excited S states with a duration of up to some 100 ps. Alternatively, another exponential term with τ_{r} could be introduced instead of f_{G}. Pulse shapes from scintillation in stilbene (organic scintillator) caused by three different radiation types are shown in figure 6.3. The normalized pulse shapes undergo different evolution in time. The rise of the pulse and a transition from prompt to delayed decay is visible. The ratio between prompt and delayed component differs, as I_1 and I_2 depend on the incident particle type. Hence, scintillators can be used for pulse shape discrimination of particles. For plastic scintillators, the prompt component dominates (also illustrated for stilbene in fig. 6.3) and typically only one decay time is stated, which describes the behavior sufficiently. [KW16]

In case of BC-404, the decay time is $\tau = 1.8$ ns, whereas the rise time $\tau_{\mathrm{r}} = 0.9$ ns is not negligible because of the very sharp pulse. This is however an advantageous behavior for applications like the scint-aTEF, where single electrons must be detected within short time frames with a high temporal resolution.

Detection of Scintillation Light

In experiments, the light output of scintillators has to be transferred into an electronic signal for further processing. For this purpose, two general devices are available: PMTs or photodiodes.

PMTs exploit the photo effect of scintillation photons on an internal photo cathode and subsequent staged signal amplification. The photons enter through a window, onto which a semi-transparent photocathode is vaporized. Eventually, photoelectrons are released from the cathode. An applied voltage accelerates them towards a dynode in the PMT, launching even more electrons. This process is repeated over some dynode stages, resulting in a cascade with enhancements of up

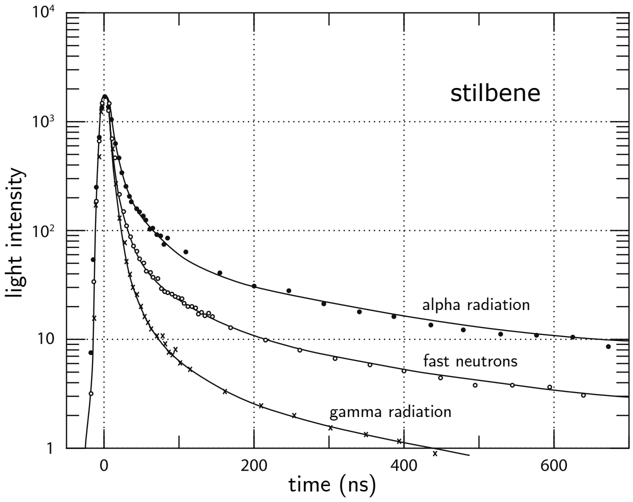

Figure 6.3.: Scintillation pulse shapes in stilbene scintillator (from [KW16]): The light output's evolution over time is provided for three different radiation types (normalized to the same maximum). The pulse shapes can be described by eq. 6.4 with different intensities I_1 and I_2, which depend on the incident particle.

to 10^9 per photoelectron as the avalanche arrives at the anode. Values of 10^5 – 10^7 are common [KW16]. However, the most important fact to rule PMTs out for an application in the scint-aTEF is their macroscopic design and the accompanying, by far insufficient, spatial resolution. [KW16]
In contrast, photodiodes can be manufactured on the micrometer scale, therefore matching the TEF dimensions. They represent a simple semiconductor realization of transformation from incident radiation flux to electrical current. Photodiodes are often PIN diodes, wherein the depletion layer's width extends far into the undoped intrinsic layer when the diode is operated in reversed bias mode. This increases the electric field. Electron-hole pairs created in this zone are accelerated towards the electrodes, causing an electrical current. The signal has to be amplified externally. Because of the reverse bias, leakage current (dark current) is an important feature of photodiodes. Although the corresponding signal-to-noise ratio (SNR) (dominated by the amplification electronics) exceeds the common level of PMTs, photodiodes provide the advantage of higher quantum efficiencies ε_Q up to 70 % (~25 % for PMTs) and coverage of a broader wavelength domain. [KW16]
Avalanche photodiodes (APDs) somehow build the bridge between photodiode and internal gain like in PMTs. They are a special realization of the photodiode with an additional metallurgical pn-junction. It serves as an internal amplification stage, since electrons undergo an avalanche effect in the corresponding high electric field throughout their propagation towards the detection electrode. Their SNR is thus determined mostly by the APD itself, which also features leakage current as mentioned above and an additional excess noise due to statistical fluctuations in the avalanche process. Multiple APDs can be combined to form large photosensitive arrays, which are known as silicon photomultipliers (SiPMs). In contrast to PMTs, they do not require bulky components like vacuum tube and photocathode window [KW16]. To illustrate the wide wavelength domain of photodiodes arranged as a SiPM, the absolute photon detection efficiency (PDE) of a representative SiPM [KET21] is shown in figure 6.2 together with the plastic scintillator emission spectrum. It is sensitive over the entire visible spectrum with a maximum PDE at ~430 nm. The combination yields an overall detection efficiency of ~44 %, which is calculated by Anton Huber.
From the typical scintillation yield of plastic scintillators and typical electron energies in the KATRIN experiment $\mathcal{O}(10\,\mathrm{keV})$, the number of photons per electron-induced event can easily be estimated to be some few hundred, of which only a fraction will possibly reach sensitive regions

of APDs. The case of single photons hitting an APD within a single event is therefore probable. Hence, reliable single photon detection is required for the scint-aTEF. This can be achieved by operation of the APD at 10 % – 20 % above its nominal breakdown voltage, where it switches from linear mode to the so-called Geiger mode. In this state, even a small primary ionization will cause breakdown directly, delivering high discharge currents. Afterwards, a quench process has to be executed to stop the discharge. Internal gains of up to 10^5 with a time resolution below 1 ns are possible for single photons. This is why they are referred to as single-photon avalanche diodes (SPADs).

In contrast to a linearly operated APD, a Geiger driven SPAD is not sensitive to magnetic fields. By arranging SPADs in an array on an integrated circuit chip with complementary metal-oxide-semiconductor (CMOS) electronics for digitization and readout, single photon sensitive digital SiPMs can be realized, whereas conventional SiPMs work analogously. These CMOS-based SPAD arrays also allow to switch off single SPADs, for example due to individual high dark current. Each SPAD is an individual unit or pixel. After a discharge, the signal is transferred to the readout and the SPAD is switched on again. It is important to note that the pixels provide binary information: they are either turned on or stay switched off. This corresponds to the minimum digital information. Due to the area coverage of the CMOS components on the chip, the overall efficiency is reduced. However, the effective quantum efficiency (including the probability of the Geiger process) of the sensitive area of the SPADs is usually $\varepsilon_Q \approx 50\,\%$. [KW16, Kel19]

In any case, light has to be guided from its origin in the scintillator, the sites of primary ionization, towards the detector. To ensure an efficient collection of light on the detector, two aspects have to be taken into account: the propagation within the scintillator and the coupling with the detector. For the first, transparency of the scintillator for the output light is a prerequisite. This is ensured by shifting the light towards larger wavelengths as explained above. For example, the bulk attenuation length of BC-404 is $\lambda_b = 1.60\,\mathrm{m}$ [Sai21]. Hence, attenuation will not result in notable losses on the comparably small length scales of a TEF structure.

On the other hand, light is likely to decouple from the scintillator at the interfaces with other media. In consequence, it is not guided properly towards the detector, which is usually only coupled to the scintillator bulk. As a countermeasure, scintillators are often surrounded by reflective materials to keep the light within. For example, they are covered with white teflon [Z$^+$18] or wrapped in aluminum foil [KW16]. Electrons with an energy of only some kiloelectronvolts will lose significant fractions of their energy in these covering layers or eventually get stopped completely. Thus, it is desired to waive any coatings. In this case, photons will be trapped in the scintillator only if total internal reflection (TIR) occurs. In case of a scintillator with refractive index n_1 in an environment (basically vacuum) with n_2, the relation of a wave's angle of incidence θ_1 and the angle θ_2 (angles w.r.t. the surface normal vector) of the refracted transmitted wave, emanating from the scintillator, are determined by Snell's law $n_1 \sin(\theta_1) = n_2 \sin(\theta_2)$. To comply with the situation, $n_1 > n_2$ is assumed in the following. $\theta_2 = 90^\circ$ corresponds to TIR, allowing for an estimation of the critical angle

$$\theta_{\mathrm{TIR}} = \arcsin\left(\frac{n_2}{n_1}\right). \tag{6.5}$$

For lower angles than θ_{TIR}, the reflection coefficient r and transmission coefficient t determine the behavior at the interface, as the wave is partially reflected in general. This means that a single photon will either be reflected or escape the scintillator. The coefficients are defined by the Fresnel equations, which distinguish between s- (index s) and p-polarized (index p) light [Dem13]:

$$\begin{aligned} r_\mathrm{s} &= \frac{n_1\cos(\theta_1) - n_2\cos(\theta_2)}{n_1\cos(\theta_1) + n_2\cos(\theta_2)}, & t_\mathrm{s} &= \frac{2n_1\cos(\theta_1)}{n_1\cos(\theta_1) + n_2\cos(\theta_2)}, \\ r_\mathrm{p} &= \frac{n_2\cos(\theta_1) - n_1\cos(\theta_2)}{n_2\cos(\theta_1) + n_1\cos(\theta_2)}, & t_\mathrm{p} &= \frac{2n_1\cos(\theta_1)}{n_2\cos(\theta_1) + n_1\cos(\theta_2)}. \end{aligned} \tag{6.6}$$

From these coefficients, reflectance R and transmittance T are obtained as $R_\mathrm{pol} = |r_\mathrm{pol}|^2$ and $T_\mathrm{pol} = 1 - R_\mathrm{pol}$ ($\mathrm{pol} = \{\mathrm{s}, \mathrm{p}\}$) [Dem13]. Scintillation photons are considered unpolarized [TR21]. However, surfaces are not plane in general and further characteristics of the surface, such as roughness, have to be taken into account.

For the coupling between scintillator and detector, equation 6.5 and 6.6 are also fundamental. A junction filled with air or vacuum would result in a bad optical transmission behavior. Instead, materials with corresponding optical properties have to be used for the connection.

6.2. Setup of the scint-aTEF

Fundamental requirement for the scint-aTEF is the possibility to create structures on the micron scale out of a scintillator with high precision, as it is also for the metallic pTEF. However, metals like gold and scintillators have very different properties regarding the processability in microstructuring procedures. Three-dimensional (3D) printing of scintillators has gained applicability and prominence within the last years [K$^+$20, Sga20]. Modern 3D printing techniques like two-photon polymerization (2PP) lithography allow for additive manufacturing of polymer structures with feature sizes on the sub-micrometer scale [P$^+$19].

In combination with a readout by a CMOS-based SPAD array, a scint-aTEF is planned to be assembled, offering spatially resolved single photon sensitivity on a sufficient timescale. In the following sections, the principle and setup are explained as well as the implementation in the Geant4 simulations.

6.2.1. Principle and general Setup of the scint-aTEF

The perspective for the scint-aTEF is the fabrication of a quadratic aTEF structure of plastic scintillator on top of a CMOS-SPAD array by using high precision techniques like 2PP lithography. As mentioned in section 6.1, a scintillator similar to BC-404 is desired for the detection of keV-electrons. CMOS-SPAD arrays are designed at the Institute of Computer Engineering (ZITI) (Heidelberg University) as interpolating digital photosensors (IDPs) and manufactured by the Fraunhofer Institute for Microelectronic Circuits and Systems [Sac16, Kel19, Fis22]. The fourth generation IDP4 [Fis22] is a CMOS-based SPAD detector that has been considered for the scint-aTEF within the scope of this work. However, the chip architecture can also be customized to serve individual requirements.

Figure 6.4 illustrates the overall setup. The quadratic grid sits on top of the plane detector surface. Its channels would provide a direct line of sight for low-angle background electrons to hit a SPAD. An additional layer of non-scintillating material is therefore planned to cover the entire detector surface below the grid. Poly(methyl methacrylate) (PMMA) is a common non-scintillating plastic which can also be deposited by spin-coating [CSS13]. It serves as potential candidate and placeholder for the material to passivate the open area of the aTEF structure. The upper edges of the walls also have to be insensitive for impinging electrons and should thus be covered with a layer of PMMA or a similar material, too. This measure improves the SBR of the structure.

At the KIT Institute of Applied Physics (APH), sample structures are printed from non-scintillating

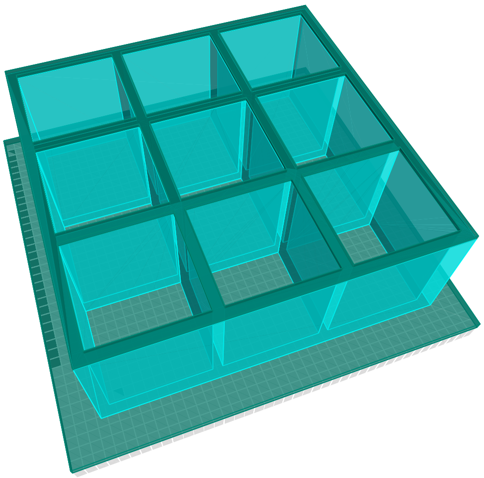

Figure 6.4.: Schematic setup of the scint-aTEF: A quadratic scintillator grid (blue) sits on top of a plane detector (pixelated gray plate below the colored components). In addition, a layer of non-scintillating material (green) is applied on top of both the scintillator grid and the detector (below the scint. grid).

plastic using the Quantum X, a 2PP lithography system of the Nanoscribe GmbH & Co. KG in Karlsruhe. Microscopic images of the 4 × 4 grid samples are shown in figure 6.5. In figure 6.5a, the overall size of roughly $1 \times 1\,\mathrm{mm}^2$ becomes clear. The scint-aTEF's dimensions are set to

$$\begin{aligned} a &= 250\,\mu\mathrm{m}, \\ b &= 25\,\mu\mathrm{m}, \\ d &= 300\,\mu\mathrm{m} \end{aligned} \tag{6.7}$$

using a similar definition as before for the pTEF (fig. 5.1). However, a is the inner edge length of the square now. The dimensions are comparable to the pTEF. d is restricted by the printing range of the Quantum X. The PMMA layer thickness is $20\,\mu\mathrm{m}$ to ensure complete energy deposition without scintillation. For dedicated studies of the layer thickness and its influence, it should be referred to [Gei22].

It should be mentioned that the structure can be printed directly onto a proper surface. The samples in figure 6.5 are printed on glass, but in principle many different substrates can be used. The PMMA layer can be applied efficiently by spin-coating or also printing. These methods will not produce a gap at the junction and ensure guiding of light onto the silicon chip. With 2PP, the grid can then be printed stable on top from the scintillator resin. Finally, the resin has to be exchanged again to print the low-rise top layer with high precision.

Scintillation light from ionizing electrons that hit the inner channel walls will be guided within the walls if it satisfies equation 6.5 or statistically due to the behavior represented by equation 6.6. Also photons with opposite direction to the detector can be reflected in the PMMA top layer and make it to a SPAD pixel, in turn. The energy deposition and light output are investigated in section 6.3. However, if a SPAD is hit by a photon, it will turn on with the probability ε_Q. This detection efficiency holds under the premise of a hit in the sensitive area of a pixel. However, the overall PDE efficiency is

$$\mathrm{PDE} = \varepsilon_\mathrm{guid}\,\varepsilon_\mathrm{loc}\,\varepsilon_\mathrm{Q}\,\varepsilon_\mathrm{trig} \tag{6.8}$$

with contribution of three additional terms: $\varepsilon_\mathrm{guid}$ accounts for the guiding efficiency (transport towards the detector) for a photon, ε_loc introduces the effect of signature localization, fill factor

(a) (b)

Figure 6.5.: Microstructured plastic grid (images by Keyence Corporation): Two microscopic images of a 4 × 4 sample structure, manufactured with 2PP lithography at the APH, are provided. Figure a: Macroscopic view on top of the grid. Figure b: Perspective view at higher magnification. Details of the surface and reflections on the glass substrate are visible.

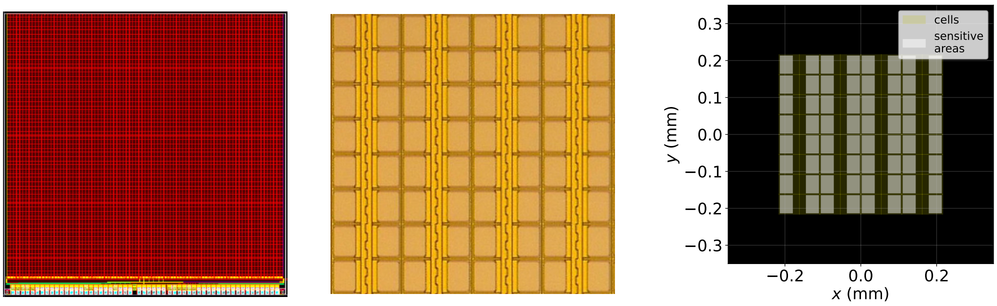

(a) (b) (c)

Figure 6.6.: Layout of the IDP4 (ZITI): Figure a (from [Fis22]): Overall chip design. Each red cell represents a SPAD pixel. Figure b (from [Fis22]): Detail of the pixels. Sensitive SPAD areas (rectangles) and circuitry (vertical bands) are visible. Figure c: Virtual implementation of the layout from fig. 6.6b.

and arrangement of the pixels and $\varepsilon_{\mathrm{trig}}$ is the trigger efficiency. It is introduced because in general, not every SPAD in on-state must be considered as signal-induced photon hit, because it could also be a dark count.

The CMOS-SPAD array of the IDP4 comprises 176 × 166 pixels or cells with an area of $54 \times 54\,\mu\mathrm{m}^2$, constituting a detector of $9.7 \times 9.7\,\mathrm{mm}^2$ in total. The sensitive area of each SPAD accounts for 52 % (corresponding to the fill factor f_{fill}) of the pixel surface thanks to a highly optimized layout. It provides multiplicity output and fast parallel output. The readout is based on shift registers and can thus operate without dead time, because hits accumulate during readout. Each SPAD yields a binary information; activated or not [Fis22]. The overall IDP4 layout is shown in figure 6.6a. Figure 6.6b provides a detailed view of the pixels. A insensitive gap of $d_{\mathrm{dead}} \geq 7\,\mu\mathrm{m}$ is required between neighboring sensitive areas due to the doping procedure. Including this specification, a virtual version of the array is created using the Python package Shapely (introduced in section 5.3). It is depicted in figure 6.6c.

The detector chip architecture is of major importance for the estimation of $\varepsilon_{\mathrm{loc}}$ (eq. 6.8). It is desired that areas onto which most of the scintillation light is guided are highly sensitive This means that insensitive “dead area” should be moved elsewhere in the chip architecture. In cooperation with the ZITI, different dedicated designs for the scint-aTEF application are discussed. The arrangement and size of the pixels can be customized as well as the trigger and readout electronics. For example, it is possible to define groups of pixels onto which a trigger criterion (e.g. trigger threshold) can be imposed (sec. 6.4).

6.2.2. Geant4 Simulation Setup

Geant4 is a comprehensive simulation toolkit for the passage of particles through matter and their interactions. It offers a wide range of physics processes and includes geometry and tracking functionality. Depending on the physics model energy ranges from the eletronvolt to the teraelectronvolt scale are covered. Geant4 is an object-oriented platform and implemented in C++ language. It is developed as the successor of the GEANT (Geometry And Tracking) series (especially GEANT 3, ref. [B$^+$87]). Applications of Geant4 cover nuclear and particle physics, accelerator design, space engineering and also medical physics. In all of these, it impresses with easy adaption to different requirements, handling of complex geometries and management of the utilized physics models. [A$^+$03]

Introduction to Geant4

The following explantions are based on [Gea21] and [A$^+$03].
Starting point of each simulation is the initialization of the desired geometries and materials, the physics processes, participating particles and further parameters. Afterwards, the action takes place, being admininstrated by a run manager. In Geant4, particle tracking is structured in different levels. The corresponding terms are run, event, trajectory, track and step. A run is started by the command `BeamOn`. As soon as the run starts, the initial geometry remains unchanged because it can not be accessed during the action. A predefined number of events is contained within the run, sharing the same environment in consequence, as it is iterated over each event in course of the run. Each event contains generation of a primary track. During tracking, the track represents a snapshot of the current particle state in terms of variables like position, momentum and track ID. However, it does not record data but is instead updated by each step. The complete history of the track is kept in the trajectory, which is therefore superordinate. Two subsequent snapshots, i.e. tracks, of a particle are separated by a step. Variables of the particle usually change throughout one step due to interactions. A step is characterized by two points, the `PreStepPoint` and the `PostStepPoint`. To extract information from the simulation, access to these concepts is possible thanks to several classes that are also used in the scope of this work.
Geant4 finds application in highly complex simulations, but also in very simple setups. Depending on the requirements, many different classes and options can thus be used. On the other hand, there are three classes which are obligatory for any Geant4 application. Apart from that, the toolkit permits extensive freedom tho the user. The three mandatory classes have to be provided to the mentioned run manager and are introduced in the following.

The `G4VUserDetectorConstruction` class allows to define the construction of the simulation environment. In the `Construct` method, a world volume is defined at first. All the action takes place within this volume. This reflects in the fact, that further volumes (daughter volumes) have to be placed within the world volume. A volume is defined by a Geant4 geometry constructor, for example `G4Box` to create a cuboid, which takes the volume name and its dimensions as arguments. The volume is then assigned to a `G4LogicalVolume`, which contains information about the volumes mother volume and its physical properties (e.g. material). With the class

`G4VPhysicalVolume`, the last step of placing and, if desired, rotating the volume to the designated configuration gives the volume a physical manifestation in the simulation.
Physical processes in the simulation take place during the particle passage through defined volumes. In general, only some aspects are of interest for the user, whereas other processes are irrelevant and thus not included. Otherwise, the computation time would exceed any acceptable limit. The purpose of physics lists is to provide a combination of physical models, which serve as a substitute for the whole range of energy and the large variety of particles. Hence, the `G4PhysicsList` is the second mandatory class. A multitude of predefined physics modules is available, each one being applicable for certain energies, interactions and particles of common problems. It is possible to compose multiple physics modules in the sub-class `G4ModularPhysicsList` of `G4PhysicsList`. A modular physics list is used in this work.
The third mandatory class is the `G4VUserActionInitialization`. It should always include a `G4VUserPrimaryGeneratorAction` to generate primaries by calling `BeamOn`. Either the `G4ParticleGun` or the `G4ParticleSource` can be used for primary generation. For the scint-aTEF simulations, we will restrict on the `G4ParticleGun`. Particle type, origin, direction, energy and polarization can be defined at the beginning of an event.

Using these and some other classes, a virtual simulation environment for the scint-aTEF is set up. The application code is found in the repository [LGŠ21]. Many aspects of the Geant4 simulations are also addressed in [Gei22].

The scint-aTEF in Gent4

The scint-aTEF geometry is incorporated in the simulations by means of the `G4VUserDetectorConstruction`. The quadratic grid is produced by usage of the `G4SubtractionSolid` class. $n \times n$ quadratic channels are punched out of a cuboid. The dimensions from equation 6.7 are applied. Afterwards, the logical volume is created by assigning the material BC-404 to the grid geometry in a `G4LogicalVolume` object. Finally, the `G4PhyscialVolume` of the scintillator is declared and placed in the world volume. The PMMA layer on top is created likewise. On the other hand, detector plate and the covering PMMA layer can be defined by means of `G4Box` objects of the corresponding materials PMMA and silicon.
For particle propagation, the composition and physical parameters of the participating materials have to be defined before being assigned to the geometric objects. The applied parameters are listed in table 6.1. The absorption band of PMMA lies about 200 nm below the emission of BC-404 (fig. 6.2) [Ahm09]. Thus, no strong attenuation effect is expected for the scintillation light. No value for the attenuation length of PMMA is found, but due to the small scales and the shifted absorption spectrum, setting the same value of λ like for BC-404 is reasonable for our purposes.
The chosen physics list, a `G4ModularPhysicsList`, reads

```
MyPhysicsList::MyPhysicsList()
{
  RegisterPhysics (new G4EmStandardPhysics()); //electromagnetic standard physics
  RegisterPhysics (new G4OpticalPhysics());
  RegisterPhysics (new G4EmStandardPhysics_option4()); //low energy option
}
```

The inclusion of the standard lists `G4EmStandardPhysics` and `G4OpticalPhysics` (introduces the optical photon) is understandable, while the additional `G4EmStandardPhysics_option4` is required for the low energy processes in the few keV regime. It is addressed in section 6.3.
In addition to the three mandatory classes, `G4VSensitiveDetector` is used to assign specific detector properties to physical volumes of the setup with the `ConstructSDandField` method of the `G4VUserDetectorConstruction`. For example, photons hitting the detector plate are

Table 6.1.: Material parameters in the scint-aTEF simulations (data from [Sai21], [AWP16] and Geant4).

material	density $\rho\ \left(\frac{\mathrm{g}}{\mathrm{cm}^3}\right)$	composition	refractive index n	attenuation length λ (m)
scintillator (BC-404)	1.023	52.4 % H 47.6 % C	1.58	1.60
passive layers (PMMA)	1.19	53.4 % H 33.3 % C 13.3 % O	1.491	(1.60)
detetctor plate (`G4_Si`)	2.33	Si	–	–
vacuum (`G4_galactic`)	10^{-25}	–	–	–

detected this way. The detector can be modified to fill certain variables of the particle in a tuple that is written to an output ROOT file. In case of the photon on the actual detector, the particle is terminated afterwards. Detector properties are also assigned to the scintillator grid, where the particles keep propagating in contrast, while information is continuously stored until a termination criterion is met. [LGŠ21]

Surface Properties of the Microstructure

2PP 3D printing is a very precise fabrication process. Nevertheless, manufactured surfaces might exhibit unevenness and roughness that differ from surfaces of the same material, that are produced otherwise or treated afterwards. Ridges on the sample surface can for example already be discovered in figure 6.5b. These are artifacts of the printing strategy. When it comes to the surface roughness (which does not follow a structure like the slices), a value of ≥ 10 nm is achievable according to the producer of the grid samples.

The surface plays an important role for the guiding efficiency. Therefore, it is investigated for the first rather low quality samples (fig. 6.5) to establish a "worst case" estimation. Higher quality samples with much smoother surfaces are also produced, but no comparably precise data of these is available for this work. The results of confocal microscopic investigations (performed at the APH) and atomic force microscopy (AFM) at the KIT Center for Functional Nanostructures (CFN) are provided in appendix C. Confocal microscopy (fig. C.7) reveals a bent structure. This can be explained by the former peeling of the grid off the glass substrate, resulting in deformation. Shrinkage throughout fabrication could also play a role. Additionally, potential optical artifacts might disturb the picture. Ridges are already visible, but a better resolution is desired. AFM in contrast can not be affected by optical effects due to the grid's transparency while the surface profile can be resolved on a nanometer scale (fig. C.8). Because ridges are dominating the surface, they will be modeled and incorporated in the surface properties. Each ridge is assumed to be a bulge with semi-cylindroid shape due to the printing process. For a ridge with height h and width w, the aspect ratio is defined as

$$\mathcal{R} = \frac{h}{\frac{1}{2}w}. \tag{6.9}$$

In the truly cylindrical (radius r) case, $h = r$ and $w = 2r$, the aspect ratio is $\mathcal{R} = 1$. In contrast, measurements of the most uneven regions (largest $\mathcal{R}$) at the CFN indicate an aspect ratio of $\mathcal{R} \approx 0.1$ (fig. C.8b).

For the statistic refraction behavior, the angular PDF of the local surface normal vector's polar angle α must be included in the simulations. The basic concept is a local deviation of the surface normal vector from the overall surface orientation by an angle α. This corresponds to a tilted local microfacet [Gea21]. Because of periodicity, only one ridge has to be regarded. Depending on the orientation of the incident light's intersecting plane of incidence, the ridges occur stretched, resulting in a different surface normal vector angular PDF, which is obtained by simple geometric considerations. Therefore, the overall PDF is averaged over equal contributions (isotropic scintillation) from every direction. For $\mathcal{R} = 0.1$, this results in a sharp spike distribution around $\alpha = 0^\circ$ with a mean or expectation value of $\mu_{|\alpha|} = 3.64^\circ$ (although $\mu_\alpha = 0^\circ$ because of two-dimensional reference plane and symmetry on the domain $\alpha = [-90^\circ, +90^\circ]$). An analytic relation for the PDF of α is not required: At such low values of $\mu_{|\alpha|}$ it exhibits an almost Gaussian shape. Hence, $|\alpha|$ is approximated as half-normal distributed with a standard deviation $\sigma_{|\alpha|} = \sqrt{\pi/2} \cdot \mu_{|\alpha|} \approx 4.6^\circ$.

In the simulations, a ground surface of the unified surface model is used for the `G4OpticalSurface` object. In this model, the surface normal vector α is randomly chosen from a Gaussian distribution with $\mu_\alpha = 0^\circ$ and standard deviation σ_α and a uniform azimuthal distribution [JM10]. Based on the results above, $\sigma_\alpha = 5^\circ$ is set and only the specular spike component occurs in the reflectance of the local microfacet to control the behavior. The relatively large value of σ_α introduces behavior similar to other possible contributions anyway. In the simulation, the surface properties of the transition between scintillator and vacuum are set the following way, for example:

```
G4OpticalSurface * OptScintVacSurface = new G4OpticalSurface("OptScintVacSurface");

OptScintVacSurface->SetType(dielectric_dielectric);
OptScintVacSurface->SetModel(unified);
OptScintVacSurface->SetFinish(ground);
OptScintVacSurface->SetSigmaAlpha(sigmaAlpha);

G4MaterialPropertiesTable * mptScintVac = new G4MaterialPropertiesTable();
mptScintVac->AddProperty("SPECULARSPIKECONSTANT", energy, specularSpike, nEntries);
OptScintVacSurface->SetMaterialPropertiesTable(mptScintVac);

G4LogicalBorderSurface * ScintVacSurface = new G4LogicalBorderSurface("ScintVacSurface",
    physScintillator, physWorld, OptScintVacSurface);
```

with `sigmaAlpha = 5.*degree`. The result of this procedure is visualized in figure 6.7 (sec. 6.3). Of course, the surface model is extendable and adjustable to the actual finish (see [JM10]).

6.3. Light Output and Energy Deposition

For the development of a suitable detector and tuning of the configuration design, the potential light output in terms of the photon guiding efficiency of the whole setup and the expected spatial distribution on the detector are considered. Also, the energy deposition of impinging electrons on the scint-aTEF and thereby arising scintillation light have to be investigated.

Trapping of Light and Guiding Efficiency

The propagation of scintillation light within the setup is investigated statistically by simulation of many scintillation photons with a common location of origin $\vec{r}_0$. The light pattern that evolves throughout propagation towards the detector is expected to depend strongly on the origin $\vec{r}_0$ because of the setup geometry. It should be noted that an incident electron will create photons

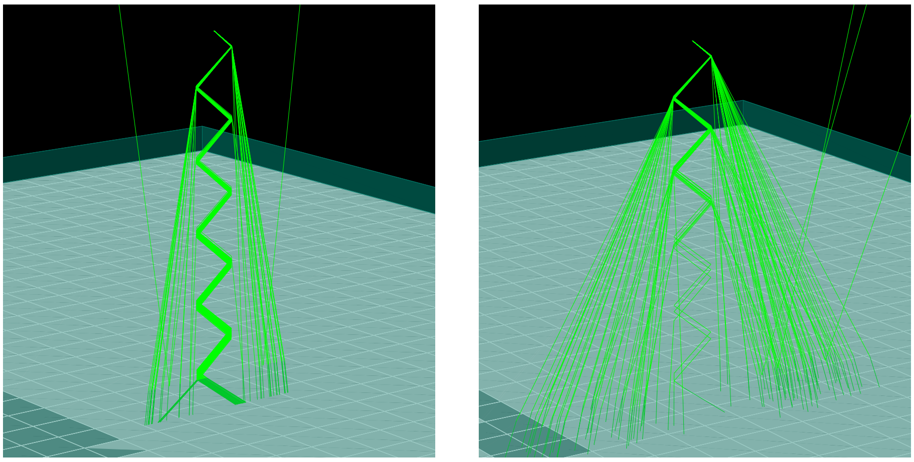

(a) **(b)**

Figure 6.7.: Refraction of optical photons at different surfaces in Geant4: The parameter σ_α of the scintillator surface is varied. The figures show refraction of an unpolarized band of 100 photons (green trajectories) in the range $\theta_{\mathrm{TIR}} \pm 1^\circ$ of TIR. The photons are emitted in the center of a wall of the BC-404 grid (the scintillator structure is invisible in the display). The centered origin of any trajectory is visible close to the upper figure edge. The initial plane of the generated directions is perpendicular to the scintillator surface and to the PMMA (transparent green) and detector plate (pixelated). Figure a: Perfect surface with $\sigma_\alpha = 0^\circ$. The behavior is only governed by eq. 6.5 and 6.6. and photons remain in the plane of incidence. Figure b: Rough surface with $\sigma_\alpha = 5^\circ$. The surface normal vector is estimated statistically (Gaussian distribution with σ_α around $\alpha = 0^\circ$) as a photon gets refracted at a surface. The refraction according to eq. 6.5 and 6.6 takes place at the corresponding microfacet, resulting in a lower trapping efficiency and additional spatial spread around the plane of incidence.

along its track, which is different from a single point.
The photon generator in Geant4 creates optical photons that are subject to Snell's law and the Fresnel equations (eq. 6.5 and 6.6). This is also the case for a ground surface with microfacets, which become the surfaces of reference then [Gea21]. The implications of this surface roughness for the refraction of light are visualized in figure 6.7 (note the subtext). Isotropic generation with random linear polarization [TR21] is assigned to the `G4ParticleGun`. Scintillation photons do not cover a very broad energy spectrum (fig. 6.2). Hence, the material properties are chosen to apply for visible to ultraviolet light and implemented without wavelength dependence, which allows to set a rather arbitrary value for the photon energy (in fact a few eV).
As soon as a photon strikes the detector plate surface, it is terminated and its position is written to a ROOT file. Alternatively, photons are terminated when they cross the world's boundaries or, very unlikely, become attenuated in the transparent components.

For the PVT-based BC-4xx scintillators ($n = 1.58$ [Sai21]), $\theta_{\mathrm{TIR}} \approx 39.3^\circ$ at the transition to vacuum with equation 6.5. This means that at least $\int_{\theta_{\mathrm{TIR}}}^{90^\circ} \sin(\theta) \mathrm{d}\theta = 77.4\,\%$ would be reflected at a perfect plane surface. This fraction is even increased by the effect of equation 6.6. Of course, the geometric and optical situation is different in the scint-aTEF setup.
Simulations of the 3×3 BC-404 grid are carried out for scintillation light from the middle of a channel wall at a height $z = (150 + 20)\,\mu\mathrm{m}$ above the detector surface. This includes $20\,\mu\mathrm{m}$ of PMMA below the structure. The important quantity is the fraction of photons that are guided all the way onto the sensitive detector. This fraction is, per definition, the guiding efficiency $\varepsilon_{\mathrm{guid}}$ in equation 6.8. For a grid with perfect surface properties ($\sigma_\alpha = 0$, fig. 6.7a) the determined efficiency,

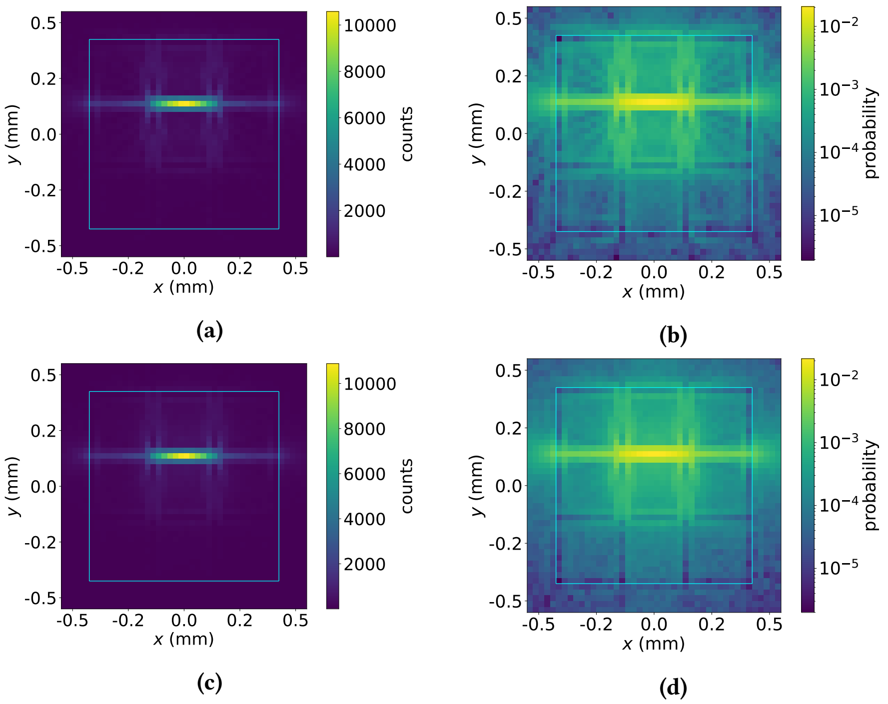

(a) (b) (c) (d)

Figure 6.8.: Photon distributions on detector surface for different scintillator surface qualities: The distributions of 10^6 simulated photons across the detector surface are provided in $25 \times 25\,\mu\text{m}^2$ bins. The outer edges of the 3×3 scintillator grid on top of the 20 µm PMMA layer are indicated in light blue. Figure a and b: Distribution (fig. a) and logarithmic probability map (fig. b) of perfect surface case ($\sigma_\alpha = 0$). Figure c and d: The same plots for a rough surface with $\sigma_\alpha = 5°$.

estimated from $N = 10^6$ photons, is at (57.7 ± 0.1) % (statistic uncertainty: normalized error $1/\sqrt{N}$ of Poisson process with error $\sigma_N = \sqrt{N}$ [Z+20]). However, this also includes photons that hit the detector apart from the grid. The systematic error due to photons terminating at the world boundaries is negligible because of the utilized $5 \times 5\text{mm}^2$ detector plate, as it is also shown in [Gei22]. In figure 6.8 (fig. 6.8a and 6.8b), the corresponding photon distribution and probability map are provided. These reveal a high guiding efficiency towards the pixels directly below $\vec{r}_0$. The binning of $25 \times 25\,\mu\text{m}^2$ is chosen to provisionally simulate a pixelated detector array with the same periodicity like the grid and to provide direct insight on the spatial correlation of grid and produced pattern.

As the surface roughness is introduced with $\sigma_\alpha = 5°$ (fig. 6.7b), the overall guiding efficiency is slightly reduced to (57.4 ± 0.1) %. Figure 6.8c and 6.8d show the corresponding distributions. The major difference is an increased spread of light away from the structure due to worse trapping. The roughness does not affect the overall guiding efficiency much, but its effect shows up in the individual efficiencies per bin, accordingly. It should affect the localization contribution ε_{loc} of the PDE (eq. 6.8).

In all distributions of figure 6.8 it is striking that the photons seem to spread away from the pixels below the walls as soon as they passed a corner in the structure. This effect is related to the PMMA layer and the corresponding “free” (no reflections) propagation between grid and detector. In addition, the refraction angle in PMMA is larger than the incidence angle on the BC-404 side because of the decreasing refractive index. Without the PMMA layer this effect is not observed, as identical simulations with rough surface but no such layers in the scint-aTEF setup reveal. The photon distributions can be found in figure C.9 (appendix C). At this point it is important

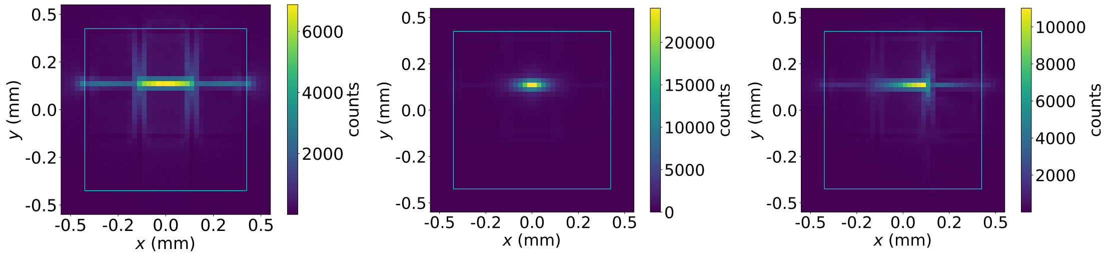

(a) (b) (c)

Figure 6.9.: Photon distributions on detector surface for different origins of scintillation light: The distributions of 10^6 simulated photons across the detector surface are provided in $25 \times 25\,\mu\text{m}^2$ bins. The outer edges of the 3 × 3 scintillator grid on top of the 20 µm PMMA layer are indicated in light blue. Figure a: High origin at $z = (250 + 20)\,\mu\text{m}$. Figure b: Low origin $z = (50 + 20)\,\mu\text{m}$. Figure c: Origin at medium height $z = (150 + 20)\,\mu\text{m}$, but shifted by $\Delta x = \ \mu\text{m}$ in x-direction w.r.t. the previous cases.

to mention the quantitative effect of the PMMA layer in the scint-aTEF: without this measure, the overall guiding efficiency would reach (59.7 ± 0.1) %, which is the corresponding value for the plots in figure C.9. The reduction of the overall effect is independent of the layer's thickness [Gei22] and can be explained completely with optical laws at the transition of both regimes. Even values of more than 60 % are possible in case of perfect plane surfaces are found in [Gei22]. In consequence, the thickness has to be tuned by means of its electron stopping power and the effect on the spatial distribution.

The spatial distribution changes as the origin $\vec{r}_0$ of the light is shifted to different locations. Simulations for three additional origins are displayed in figure 6.9. Compared to the otherwise similar setup resulting in the distribution from figure 6.8c, the overall guiding efficiencies also differ For example, changing the distance from the detector to larger (smaller) values of $z = (250 + 20)\,\mu\text{m}$ ($z = (50 + 20)\,\mu\text{m}$) yields a increase to (62.4 ± 0.1) % (decrease to (52.2 ± 0.1) %). As expected, the spread of the photons changes, which is clearly visible in the corresponding photon distribution in figure 6.9a (6.9b). On the other hand, a translation of $\vec{r}_0$ by 100 µm in the x-direction results in the distribution in figure 6.9c (overall $\varepsilon_{\text{guid}}$ is (57.5 ± 0.1) %).
As a consequence, the scintillation process at various interaction positions due to incoming electrons would always require different probability maps to establish the potential final photon distribution statistically. An approach could be to generate the number of photons which is created by an electron of a certain energy based on the light yield of ~10 γ/keV [Ham21] for plastic scintillators. Expected electron energies in the 20 keV regime result in ~200 photons. $\varepsilon_{\text{guid}}$ determines the final number of photons on the detector (Poisson statistics and corresponding fluctuations should be imposed) which are then distributed according to the probability map. While this procedure is poorly applicable for an arbitrary large number of distinct $\vec{r}_0$, direct simulation of electrons and induced scintillation with subsequent light propagation as in the preceding paragraphs is the more efficient way.
Nevertheless, the studies indicate a sufficient guiding performance and photon transport properties that result in a distribution which is correlated with the scintillator grid despite the lack of a covering layer to improve the surface reflectance.

Energy Deposition and Scintillation

Electrons dissipate kinetic energy in the scintillator material. This process is characterized by the stopping power (eq. 6.3). In turn, scintillation occurs according to Birks' law (eq. 6.1).

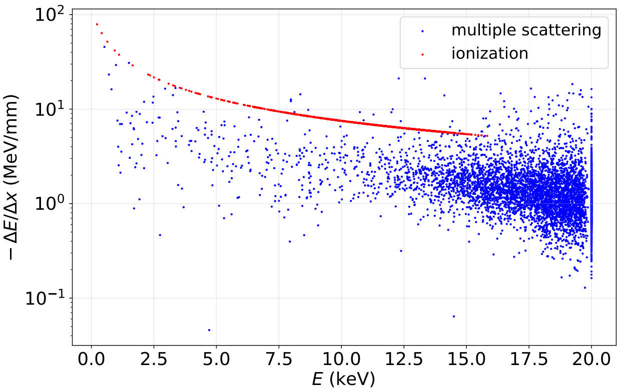

Figure 6.10.: Simulated electron stopping power in BC-404: The stopping power $-\Delta E/\Delta x(E)$ of 10^3 simulated electrons in BC-404 is plotted over the energy before the tracking steps. Each point corresponds to a step. The corresponding process to each step is indicated by colors.

The low energy electromagnetic physics constructor `G4EmStandardPhysics_option4` is used in the simulations because of its good agreement (within 15 %) with reference data from 5 keV to 200 keV, thus matching the required energy range. For lower energies, the deviation increases to about 40 % [A$^+$20d]. The stopping power in `G4EmStandardPhysics_option4` is in fact not calculated as in equation 6.3, but using models of the contributing processes. The same holds for backscattering of electrons off the structure surfaces, which includes a Mott correction for example. A more detailed discussion of the models and included processes can be found in [Gei22], where `G4EmStandardPhysicsSS` is found to be another possible model with increased agreement. However, the advantage is overcome by much longer and expensive computations.

The first simulations address the stopping power and range of incident electrons in the scintillator material. Exemplarily, a perpendicular beam of 20 keV electrons in x-direction is generated directly in front of a BC-404 tile (thickness of 25 µm, representing a scint-aTEF wall). Reflected electrons terminate on the surface of a detector volume surrounding the tile, which allows for a quick estimation of the backscattering probability $\mathcal{P}_{\text{back}}$.
The penetration depth d_{pen} is of major importance. It is defined as an electron's maximum distance from the incidence surface (inside the material). On the other hand, the stopping power relates the initial energy to a track length l. The latter can also be extracted by electron tracking within the tile. [Gei22] provides resulting values for a broad electron energy range: from 10^5 20 keV electrons, a mean value of $\bar{d}_{\text{pen}} = (4.881 \pm 0.007)$ µm (maximum depth $d_{\text{pen,max}} = 8.778$ µm) is obtained. The extracted mean track length is of course longer with $\bar{l} = (8.329 \pm 0.009)$ µm (maximum length $l_{\text{max}} = 12.447$ µm). In case of PMMA, these values does not change much. For higher energies the ranges increase, but a thickness of 10 µm is concluded to be sufficient to absorb most of the electrons completely. [Gei22]
Throughout particle propagation, the occuring physical processes are assigned to the `G4StepPoint` objects of each tracking step. Also, the energy and position are tracked. This allows for the estimation of the effective stopping power $-\Delta E/\Delta x(E)$. ΔE is the step's energy loss, Δx the spatial length of the step and E the energy at the `PreStepPoint` prior to the actual step. Figure 6.10 reveals the stopping power experienced by 10^3 electrons included in the plot. It is clearly visible that every electron at first undergoes a scattering (`G4eMultipleScattering`) process. As some energy is deposited, ionization processes (`G4eIonisation`) come into play, accounting for enhanced stopping powers. In contrast to multiple scattering, these steps follow a discrete law [Gea21].
However, not all electrons end up in the tile, as they might also experience backscattering off the

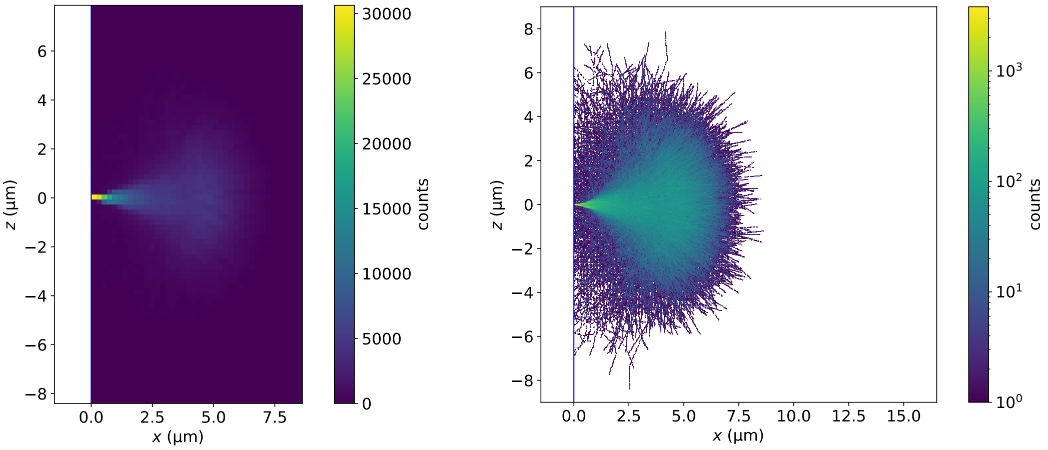

(a) **(b)**

Figure 6.11.: Simulated creation of scintillation photons from incident 20 keV electrons in BC-404: 10^4 incident (from the left) electrons are created. 4.17 % experience backscattering. The blue line indicates the scintillator surface. Figure a: Distribution of photon creation points within the scintillator. Figure b: Logarithmic version of fig. a. Individual electron tracks are visible, being lined with created photons. The maximum penetration depth can be estimated.

surface. In the simulation setup for the estimation of the stopping power with 10^4 20 keV electrons, it is determined to $\mathcal{P}_{\text{back}} = (4 \pm 1)\,\%$. Backscattering is thoroughly investigated in [Gei22] for variation of both energy and incidence angle of the electrons. Low-angle background electrons are very likely to scatter off the surface. They will presumably end up in the insensitive PMMA layer or elsewhere in the grid. The timescale of these transits is on the picosecond scale. Anyways, they deposit a significant amount of energy in the material, which is the further reduced the lower the incidence angle becomes (ref. [Gei22]).

Scintillation is introduced by adding the required properties to the `G4MaterialingPropertiesTable` of BC-404. The parameters are the following: rise time $\tau_r = 0.7\,\text{ns}$, decay time $\tau = 1.8\,\text{ns}$ [Sai21] and the Birks constant (of comparable BC-408) $kB = 0.155\,\text{mm/MeV}$ [P⁺21]. A delayed component can also be set in principle, but is not provided for the prompt scintillator BC-404. The created photons are tracked and their origin positions $\vec{r}_0$ are investigated for the same setup as above. Figure 6.11 shows the two-dimensional projection of the $\vec{r}_0$ on the x-z-plane intersection of the scintillator tile. While figure 6.11a exposes the overall distribution, with a strongly pronounced maximum directly behind the point of impact, the logarithmic plot in figure 6.11b reveals individual electron tracks and single photons which are created along their paths. Recalling $\bar{l} > 8\,\mu\text{m}$ clarifies that the paths are far from being straight due to numerous scattering events. The pronounced maximum can be understood by noting the fact, that the paths do start to spread strongly due to statistics not before having covered a certain range in the material. This results in a high local density.

6.4. Signature, Detector Response and Trigger Investigations

Potential detector signatures are obtained by simulation of incident electrons, subsequent scintillation (see fig. 6.11) and optical transport of the photons (see e.g. fig. 6.8).

In case of an application in the KATRIN experiment, the electrons follow cyclotron trajectories. These are already discussed thoroughly in the chapters 4 and 5. To allow for cyclotron motion in the Geant4 simulations, a magnetic field is introduced in the `G4VUserDetectorConstruction`:

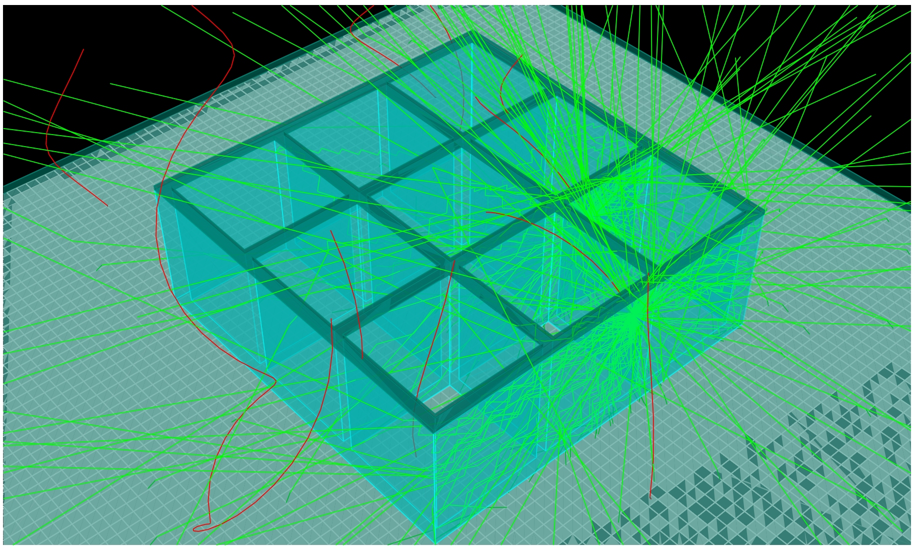

Figure 6.12.: Geant4 simulation of the scint-aTEF: The setup is known from fig. 6.4. PMMA layers are transparent green, the scintillator is represented by the light blue structure. The setup sits on top of the (pixelated) detector surface. Incident electrons ($E = 20\,\mathrm{keV}$) in the magnetic field at $B = 2.5\,\mathrm{T}$ are shown in red. Two of them hit the scintillator material, inducing emission of optical photons (green lines). These are partially guided within the scintillator. Some trapped photons decouple after multiple TIRs due to the surface properties.

```
G4MagneticField * magField = new G4UniformMagField(G4ThreeVector(0., 0., 2.5*tesla));
G4FieldManager * globalFieldMgr = G4TransportationManager::GetTransportationManager()->
    GetFieldManager();
```

The `globalFieldMgr` is declared to access member functions for field management afterwards. A uniform magnetic field in simulation z-direction (corresponding to negative z-direction in KATRIN coordinates) is chosen (sec. 5.1). Electrons are created uniformly in on a x-y-plane above the scint-aTEF construction with isotropic momenta but oriented towards the detector half-space. As before, the energy is set to 20 keV.

Figure 6.12 gives an impression of the resulting processes in Geant4. 10 electrons are included, of which only two hit the scintillator grid. This causes many decoupling photons (green trajoectories) but also a large amount of trapped light (within the transparent blue structure). The green intransparent components represent PMMA. A single electron event is investigated. The photon pattern on the detector surface (gray layer in the lower corners of fig. 6.12) is provided in figure 6.13. It is split into two sections. In figure 6.13a, the quadratic bins are chosen to be on the same scale of $25 \times 25\,\mu\mathrm{m}^2$ as in section 6.3. It is increased to an arbitrary value of $68 \times 68\,\mu\mathrm{m}^2$ in figure 6.13b. This is meant to represent different designs of a SPAD array, where the pixel size is varied. A potential detector can be estimated (right plots of both figures) by assuming a quantum efficiency of $\varepsilon_\mathrm{Q} = 40\,\%$. Based on this probability, it is randomly decided for each photon whether it tuns the pixel on or not. Therefore, the same photon pattern will create independent and, very likely, different simulated responses every time the response is computed. A shaded area surrounding the scintillator grid (blue) indicates the ROI pixels. It is chosen to extend beyond the grid borders in any case based on the knowledge from section 6.3 where a spread of the light is found.

2×10^3 electrons are generated and the responses are computed in the same way as above. About 64 % of them cause scintillation in the grid and are thus potentially detectable. This number should not yet be confused with any kind of efficiency, because the generator is not adjusted properly in terms of flux mapping onto the grid and furthermore the angular distribution does not match

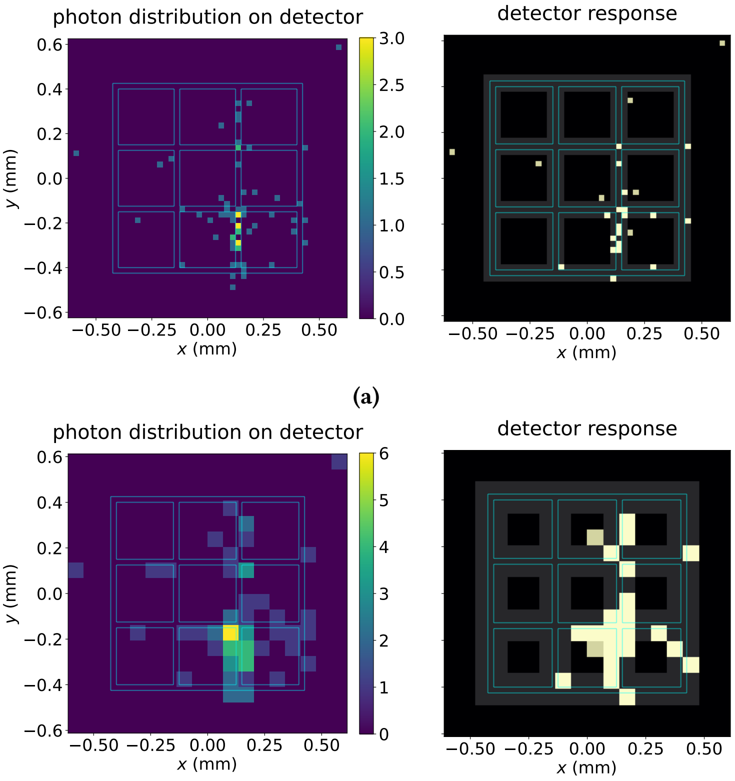

(a)

(b)

Figure 6.13.: Photon pattern and simplified detector responses: The detector is simplified by quadratic cells of 25 × 25 μm^2 (fig. a) and 68 × 68 μm^2 (fig. b). The left plots both show the same photon pattern as it is binned in these virtual detector pixels of different size. The photons are produced by scintillation of a single incident 20 keV electron. By imposing a quantum efficiency $\varepsilon_Q = 40\,\%$ on every photon, a potential binary detector response (plots on the right) is obtained. Pixels below the scintillator grid (indicated in blue) that are expected to be particularly illuminated due to the guiding efficiency are marked in gray.

perfectly. Nevertheless, it serves well for investigations of the photon patterns. Variations of the pixel size over a range from $20^2\,\mu m^2$ to $120^2\,\mu m^2$ are carried out. The overall number of switched on pixels decreases slightly with their size, which is just an effect of the pixel density. In turn, the fraction of illuminated ROI pixels of the overall ROI pixel number increases due to the worse "resolution". However, the spatial resolution gets the worse, the larger the pixels are chosen to be. This would imply a loss of information in the experiment.

In addition, it should now be taken into account that the sensitive area of the pixels that actually exhibits an efficiency $\varepsilon_Q = 40\,\%$ is not the entire detector surface but a fraction f_{fill} of the chip. For example, the fill factor of the IDP4 is $f_{\text{fill}} = 52\,\%$ [Fis22]. This will reduce the PDE of the setup due to spatial effects, corresponding to the efficiency ε_{loc}. Using the Python package Shapely, a script is created to allow for arbitrary pixel arrays to be built up and implemented for the signatures' processing. Two layouts will be investigated: the IDP4 layout in figure 6.14a (also in fig. 6.6c) with rather uniform coverage and a dedicated detector layout for the scint-aTEF application, which relies upon the previous findings. This layout is represented by figure 6.14b. It is designed to keep 7 μm distance between the pixels while maximizing the corresponding active area in the highly illuminated regions below the grid and established in cooperation with the ZITI.

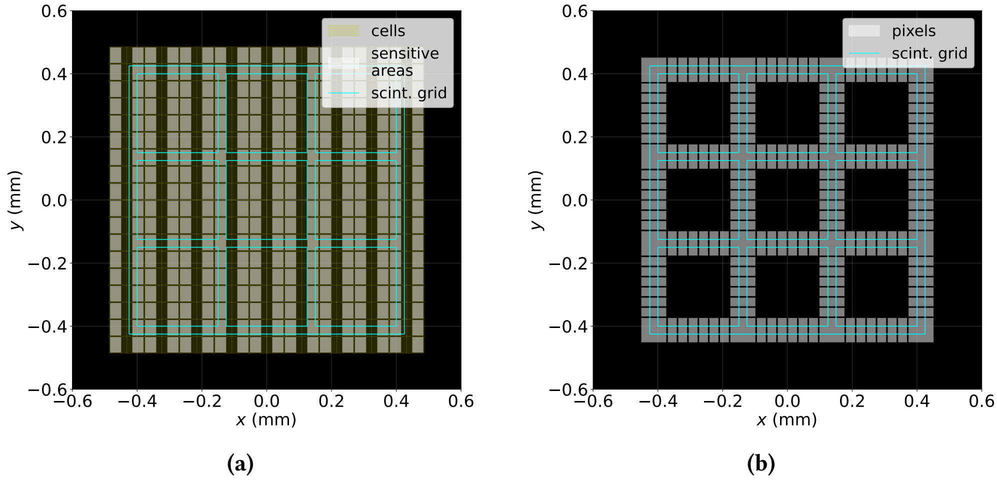

(a) (b)

Figure 6.14.: SPAD array layouts for the scint-aTEF: The scintillator grid is indicated in blue. Figure a: The layout of theIDP4 (cf. fig. 6.6) is a collection of identical (mirrored) cells ($54\times54\,\mu\mathrm{m}^2$). These consist of a sensitive SPAD area (f_{fill} = 52 %) and circuitry. Sensitive areas are separated by d_{dead} = 7 µm. Figure b: Dedicated detector layout for the scint-aTEF. Only sensitive areas are displayed. They are arranged below the scintillator grid to minimize the dead area (due to d_{dead} in particularly illuminated regions. Two types of pixel shapes occur, rectangular ($75.0\times25.2\,\mu\mathrm{m}^2$) and quadratic (in the corners, $75\times75\,\mu\mathrm{m}^2$). Further components of the chip are not indicated but find plenty of space in the channel centers.

Given these models, the detector response can be estimated directly: using the `contains` method it is checked whether a detectable photon hit (by means of ε_Q) on the detector is contained within the entirety of active areas, represented by a `MultiPolygon` object. If this is the case, the individual `Polygon` object of the pixel is obtained the same way. Eventually, the pixel is switched on. It would also be possible to impose the statistic selection due to the quantum efficiency after the spatial selection. However, from the copmutational point of view, the spatial selection is far more expensive than rolling a dice, making the implemented order superior.

Altogether, the photon hits are classified as detectable or invisible (ε_Q). Every detectable photon that lies within a pixel ($\varepsilon_{\mathrm{loc}}$) results in it being switched it on (“activated”). The output of a single electron event is shown in figure 6.15. Both invisible and detectable photons are displayed. In the displayed case, 23 photons that are preselected as potentially detectable activate 11 pixels. This means that at least roughly 7 % of the initial light (~200 γ) is detected.

Generation of the detector response for each scintillation-inducing electron allows to determine a mean number of $\bar{N} = (10.9 \pm 0.2)$ activated pixels. The corresponding distribution with $\sigma_N \approx 4$ is provided in figure C.10 (appendix C). Because of localization effects and the dead area between neighboring pixels, this number depends on the number n of pixels below the walls and the pixel size, characterized by their width w and height h. The height is laid down by n, w and the gap of d_{dead} = 7 µm (but $h = w$ for square-shaped corner pixels). For example, a pixel size of about $75.0\times25.2\,\mu\mathrm{m}^2$ ($w = 75\,\mu\mathrm{m}$, $n = 6$) is applied in figure 6.14b, 6.15 and C.10.

Both n and the size can be adjusted to ensure good performance of the system. It has to be taken into account that the remaining components besides the active areas take up some space on the detector. This is indicated in figure 6.14a, where the yellowish space surrounding the sensitive areas represents d_{dead} and also the pixel circuitry. In this layout of the IDP4, these components are distributed over the detector in columns. In case of the dedicted layout (fig. 6.14b) the readout circuitry is planned to be arranged in the center of the scintillator grid channels, where the illumination is lower anyways. Without going into detail on this, it should be mentioned that the

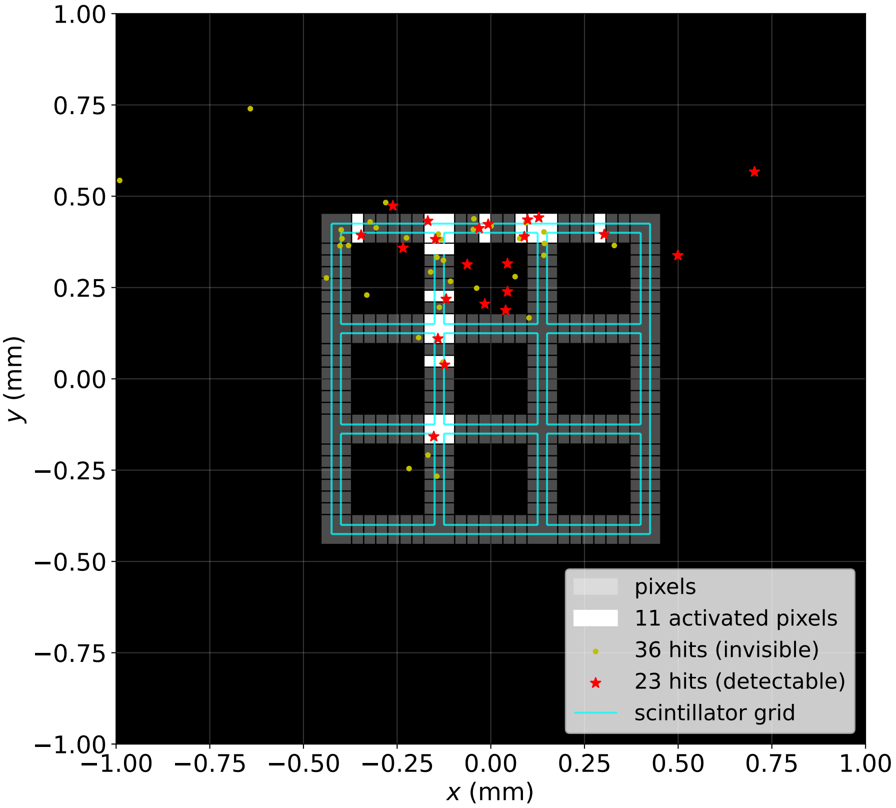

Figure 6.15.: Simulated detector response of the scint-aTEF: Scintllator grid and pixels of the dedicated detector layout are displayed similar to fig. 6.14b. The photon pattern on the detector created by scintillation of an incident 20 keV electron is shown. The quantum efficiency $\varepsilon_Q = 40\,\%$ determines whether they are potentially detectable (red asterisks) or not ("invisible", yellow dots). Pixel that are struck by at least one detectable photon are switched on.

number of pixels per area is limited by the size of the readout.

The resulting frequency of events at certain pixel sizes $w \times h$ is provided in figure 6.16 for a number of $n = 6$ as in the previous cases. The distribution is shifted towards higher numbers N of activated pixels and mean numbers $\bar{N}$, accordingly. However, the corresponding shifts gets smaller, the larger w is set. This is why larger values are favored. On the other hand, the number n can also be varied. The effect of tuning n in a practicable regime does not imply a strong effect. This circumstance is clarified with the distributions in figure C.11 (appendix C).

With larger values of w, the fraction of corner pixel and rectangular "wall pixel" size increases significantly until the latter basically become thin strips. This would be far from a desirable design because of the imbalance in spatial coverage and pixel sizes. Therefore, the beneficial combination $w = 75\,\mu\text{m}$ at $n = 6$ is for the time being chosen for the dedicated scint-aTEF detector layout, since it does not exhaust the limits while performing comparable to larger w configurations, but with an appropriate spatial coverage. The IDP4 setup layout (fig. 6.14a) is investigated similarly, indicating a mean value of $\bar{N} \approx 13$, thus surpassing the dedicated layout in numbers. But in contrast, the layout has a preferred direction and does not offer enough space for a more sophisticated readout, like dedicated one does. Instead, it is associated with the usual readout of the IDP4.

The final part for this work is the trigger efficiency $\varepsilon_{\text{trig}}$ in equation 6.8. Trigger groups are a concept that can be applied to CMOS-SPAD arrays. Basic principle is the connection (wired OR) of

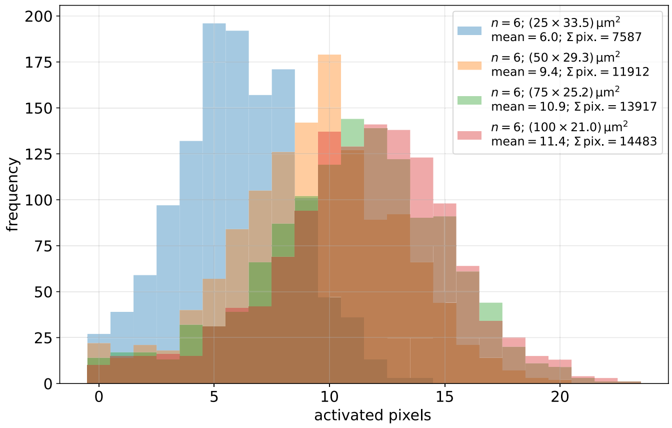

Figure 6.16.: Activated pixel numbers under variation of SPAD array pixel size: The number of activated pixels in events that result in photons on the detector is shown. The number of pixels between the channel corners in the dedicated layout (fig. 6.14b) is fixed to $n = 6$. The pixel dimensions are varied, while preserving the required dead space d_{dead} between neighboring SPADs.

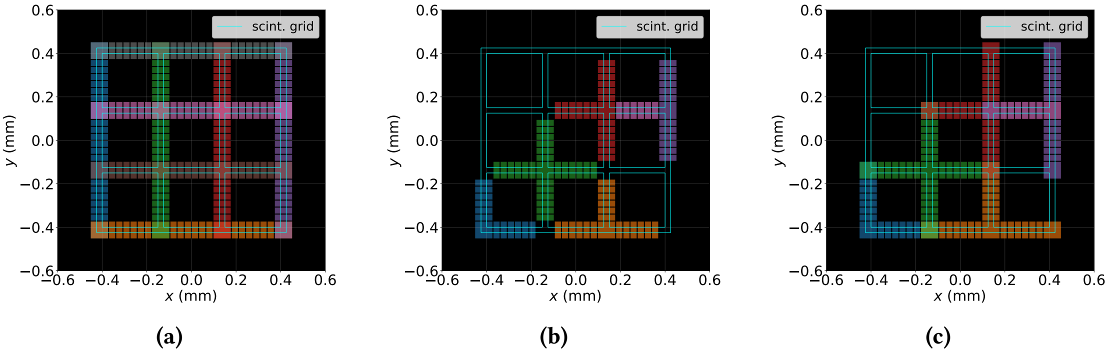

(a)

(b)

(c)

Figure 6.17.: Trigger group layouts: The definition of trigger groups in the 3×3 case is illustrated. Pixels that are assigned to the same trigger group have the same color. Overlapping naturally occurs. Figure a: Rows & columns (mode I). Figure b: Small crosses (mode II). Figure c: Large crosses (mode III).

multiple SPADs to sum up their signals. Enough space on the detector surface must be granted to the required CMOS components. In simple terms, it is achieved that groups acquiring a minimum number of entries result in a trigger and readout of the group. One single SPAD can in principle be assigned to many different groups. Originally, the motivation to the implementation of trigger groups in the chip architecture is to exclude, dark counts on the array: besides a macroscopic low gradient and single noisy SPADs, the dark counts are approximately uniformly distributed across the detector [Fis22]. The advantage of disengageable SPADs pays out when it comes to dark count reduction due to noisy ones, whereas a baseline of dark current remains. By requiring an unlikely (for dark count events) high number of entries within a group, false triggers can be suppressed efficiently. The emerging task is to define both a suitable shape of the group and an appropriate trigger criterion.

Three different shapes are investigated: rows & columns (mode I), small crosses (II) and large crosses (III). Their definitions (for the 3 × 3 grid) are given in figure 6.17. To allow for a comparison of the shapes, the number of activated pixels in the "brightest group" is consulted as a useful quantity. The brightest group is the one with the highest count of activated pixels for a single

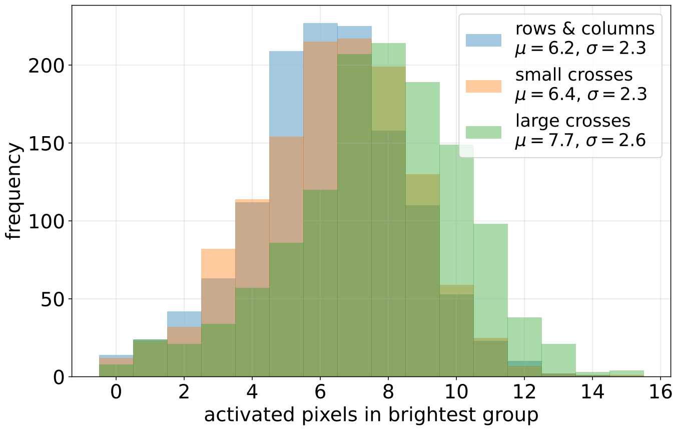

Figure 6.18.: Activated pixel numbers in the brightest trigger group for different group layouts: For every event that illuminates the detector plate, the number $N^{\bigstar}_{\text{group}}$ of activated pixels in the brightest trigger group(s) (i.e. the decisive group(s) with maximum number of counts) is extracted. The resulting distribution is shown for the three diferrent trigger group layouts (fig. 6.17). Mean values μ and RMSDs σ of the distributions are provided.

scintillation shower. This number is labelled $N^{\bigstar}_{\text{group}}$. Of course, two or more groups with the same number can claim this title as well as all groups at once, in case no SPAD is activated at all. With the simulation results, the distribution of $N^{\bigstar}_{\text{group}}$ is computed from the detector response for each group layout and is displayed in figure 6.18.

The overall distributions with mean $\bar{N}^{\bigstar}_{\text{group}}$ are compared: modes I and II perform very similar with $\bar{N}^{\bigstar}_{\text{group}}(\text{I}) = 6.2 \pm 0.1$ and $\bar{N}^{\bigstar}_{\text{group}}(\text{II}) = 6.4 \pm 0.1$ with equal spread. Including additional corner pixels in mode III enhances the brightness noticeably to $\bar{N}^{\bigstar}_{\text{group}}(\text{I}) = 7.7 \pm 0.1$ with slightly increasing spread. This has direct implications on the trigger efficiency $\varepsilon_{\text{trig}}$. Because a minimum number of activated pixels is considered as trigger criterion (trigger threshold) here, the efficiency can be determined directly from the distributions of $N^{\bigstar}_{\text{group}}$, because at least the brightest group has to reach the threshold. $\varepsilon_{\text{trig}}$ is obtained as the ratio of these primary events actually resulting in a trigger and the total (potentially detectable) event number. In figure 6.19 the tigger efficiency is plotted over the applied threshold for each mode. As expected, I and II behave basically the same. The large crosses are clearly superior above a threshold of 4 pixels. However, a notable reduction ($\gtrsim 10\,\%$) of the detection efficiency and loss of signal would be accepted by setting the threshold that high. Anyhow, a low threshold (but obviously above 1) is desired. Hence, a minimum of 2 to 3 pixels would provide acceptable efficiency, regardless of the trigger group layout (I, II or III). Nevertheless, a decision in favor of the large crosses can be justified with the higher degree of correspondence between signature and group shape as well as the possibility of higher thresholds, if still desired.

The dark count (coincidence) rate per group has to be established to check for reasonability of the threshold. For the CMOS-SPAD array, the dark count rate is stated normalized to the sensitive area A as R_{dark}. At room temperature, $R_{\text{dark}} \approx 50\,{}^{\text{kHz}}\!/_{\text{mm}^2}$ can be assumed as usual noise. The second important quantity is the "coincidence window" Δt for the trigger criterion to be met. Because of typically short decay times for plastic scintillators and photon transport on the picosecond scale, $\Delta t \approx 50\,\text{ns}$ would already be sufficient to collect basically every photon. This is reproduced in the simulations. However, two time components and the rise time (decay according to eq. 6.4) can be set manually in the simulations.

Such short times ($\Delta t \approx 50\,\text{ns}$) are technically possible for the coincidence window. Assuming

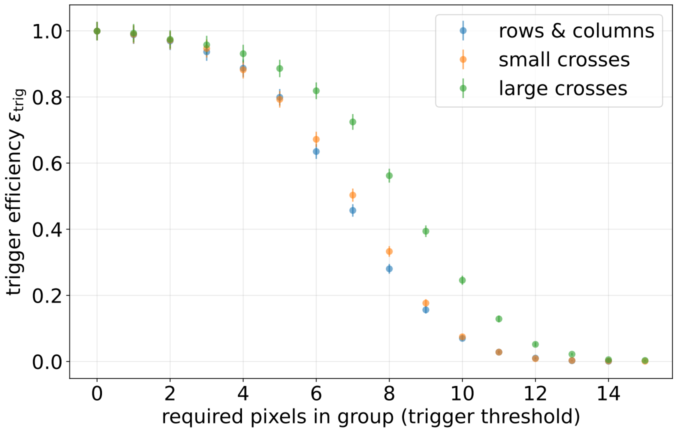

Figure 6.19.: Trigger efficiency and its threshold dependence: For the different trigger group layouts (fig. 6.17), the trigger efficiency $\varepsilon_{\mathrm{trig}}$ is plotted over the trigger threshold. The data points can be obtained directly from figure 6.18, since the efficiency describes the fraction of events with $N^{\star}_{\mathrm{group}}$ above the threshold and of the total number.

an exponential PDF ${}^{\mathrm{d}\mathcal{P}}\!/\!_{\mathrm{d}t}(t) = \eta\,\mathrm{e}^{-\eta t}$ [Z⁺20] of the times t between two subsequent dark counts (Poissonian process) with $\eta = A \cdot R_{\mathrm{dark}}$, the probability $\mathcal{P}^{\mathrm{co}}$ of a coincidence is approximated as the probability of two counts within Δt and can therefore be written as

$$\mathcal{P}^{\mathrm{co}} \approx \mathcal{P}(t < \Delta t) = 1 - \mathrm{e}^{-AR_{\mathrm{dark}}\Delta t}. \tag{6.10}$$

For the large cross configuration (assuming a large array without border effects), the sensitive area of the groups' pixels adds up to $7.35 \times 10^{-2}\,\mathrm{mm}^2$, associated with a dark count rate of $R_{\mathrm{group}} = 3.68\,{}^{\mathrm{kHz}}\!/\!_{\mathrm{group}}$ that can be set for AR_{dark}. In consequence, $\mathcal{P}^{\mathrm{co}} \approx 1.8 \times 10^{-4}$ and the dark coincidence rate is roughly $R^{\mathrm{co}}_{\mathrm{dark}} \approx \mathcal{P}^{\mathrm{co}} AR_{\mathrm{dark}} = 0.7\,\mathrm{Hz}$ in each group. A trigger threshold of 2 would thus still result in significant contributions of dark counts. In addition, the actual number of groups has to be very high: a fluxtube area of $\sim 6 \times 10^3\,\mathrm{mm}^2$ [HHL21] must be mapped on the scint-aTEF. The corresponding scintillator grid (eq. 6.7) would require $g{\sim}80 \times 10^3$ channels and about the same number of trigger groups. The probability for none of these groups to produce a dark coincidence within Δt is $(1-\mathcal{P}^{\mathrm{co}})^g$ on the order of 10^{-7}. Of course, for a trigger threshold of 3 and thus two-fold dark coincidences (i.e. three dark counts within Δt), this probability decreases significantly, which will not be discussed in detail.

Cooling of the setup is an efficient way to dramatically reduces dark counts. At an operating point of 220 K, $R_{\mathrm{dark}} < 1\,{}^{\mathrm{Hz}}\!/\!_{\mathrm{mm}^2}$ can be achieved [Fis22]. The probability to have no coincidence on the entire setup increases from formerly 10^{-7} to about 99.97 %. If this should not yet suffice the requirements, the threshold can be elevated to 3.

6.5. Experimental Setup

An experimental test setup is developed for measurements with a CMOS-based SPAD detector at low temperatures. The detector, currently the IDP4, is located inside a vacuum cross with four CF flanges of size DN200. The setup is displayed in figure 6.20. Inside the stainless steel chamber, a pressure of about 10^{-4} mbar is maintained with a suitable vacuum pumping device (port on the right in fig. 6.20a). In addition, the detector can be cooled down to about −60 °C. This is achieved by mounting the printed circuit board (PCB) of the detector on a coolable holding structure (fig. 6.20b). The structure consists of a copper block with internal pipelines for the

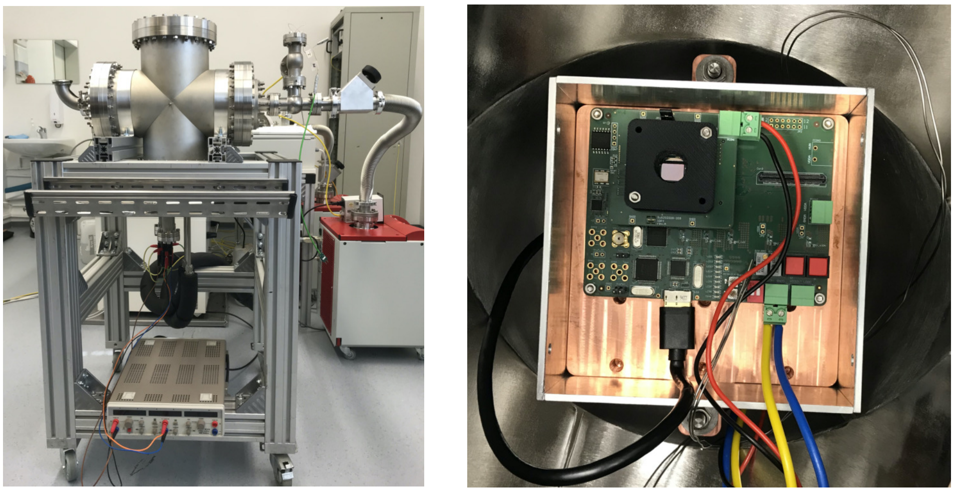

(a) (b)

Figure 6.20.: Test setup for the scint-aTEF: Figure a: The vacuum cross is placed on a rack, where the power supply is also located (lower device). Cabling towards the feedthroughs is visible, as well as the coolant pipes (black). On the right, the chamber is connected to the vacuum pump. The connection is equipped with a pressure gauge and a PT100 temperature sensor. Figure b: PCBs of IDP4 and FPGA inside the vacuum chamber, top view. The lower PCB is mounted on top of the coolable holding structure (copper block). Voltage supplies for the FPGA (yellow, blue) and the detector (black, red) and the USB Micro-B connection are displayed. The detector surface can be seen in the hole of the custom-made black cover's hole, where a thin cover bar protects the wire bonds on the chip's upper edge.

coolant which is provided by an external cooling device. Operation in vacuum is necessary, because otherwise harmful condensation of liquids on the detector could occur. Also, it ensures a sufficient thermal insulation. The windowless sealed vacuum system is beneficial for operation of the SPAD array, since it is naturally a very light-proof environment. This is mandatory due to single photon sensitivity.

The cooling pipes are welded into the bottom flange cap of the cross (lower flange in fig. 6.20a, only the pipes are visible). Two pipes guide the cables from the detector towards different feedthroughs. The SPAD array itself needs a voltage of about 23 V – 25 V for the reverse bias. Another feedthrough serves the data transfer between an external computer and the device with a USB 3.0 connection. A second voltage supply feedthrough is required for operation of the field programmable gate array (FPGA) at 3.3 V. The FPGA builds the bridge between SPAD array and the computer. It is programmed to take care of data processing and enable communication with the computer, where the device can be accessed with a user interface (UI).

The UI is provided by the ZITI together with the IDP4 and gives the operator flexible control of many parameters. Only some of them will be addressed here. The readout can be driven in continuous mode or in automatic accumulation for the triggered mode. For our purposes, the latter is of specific interest, as the previous section clarified. A multiplicity trigger for a certain number of triggered SPADs in one column (fig. 6.6b) can be set to a minimum required number (up to 4). The length of the integration window after a trigger occurs is also adjustable from effectively about 100 ns to some microseconds. An important feature of the UI is the possibility to access the count rate of each pixel. All noisy pixels (also: bits) above a certain frequency can be turned of, i.e. they are set as "kill bits". This procedure is meant to exclude noisy or faulty bits and can be executed during operation.

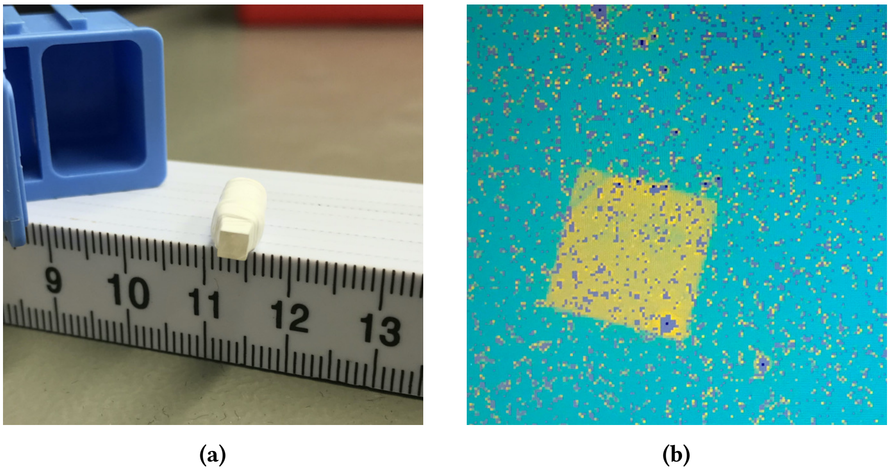

(a) (b)

Figure 6.21.: LYSO crystal and image taken with the IDP4: Figure a: The small LYSO crystal of about 3 × 3 × 10 mm^3 is put on a meter rule for scale. The transparent anorganic scintillator is wrapped in teflon tape (white). Figure b: Recorded image of the bare crystal base area, created by scintillation light. The image is a detail of the IDP4UI and represents an accumulation of more than 2000 frames. Yellow regions correspond to high count numbers. Kill bits (gray) surrounded by high rate regions due to dark counts are uniformly distributed across the detector which is operated at room temperature.

Some measurements with the IDP4 are already carried out with lutetium-yttrium oxyorthosilicate (LYSO), an anorganic scintillator. A LYSO crystal is placed directly on the surface of the detector chip (shiny surface in the black cover's hole, fig. 6.20b). It is shown in figure 6.21a, wrapped in teflon tape. Its open base area measures about 3 × 3 mm^2. LYSO is intrinsically weakly radioactive due to beta decays of the isotope ^{176}Lu, which accounts for 2.6 % of natural lutetium, to excited states of ^{176}Hf. In consequence, self-detection of the primary beta particles and subsequent gamma quanta of the hafnium de-excitations gives rise to constant scintillation events [A$^+$18]. This makes the small crystal a suitable light source for a first proof of the CMOS-SPAD detector's potential. With the multiplicity trigger at 4 and an integration time of about 200 ns, an image of the crystal is taken. The accumulated image from more than 2000 individual frames is displayed in figure 6.21b, a detail of the IDP4UI. In spite of uniformly distributed noisy regions, the square-shaped base area is clearly visible. An interesting detail of the pronounced structure is the splintered upper right corner of the mapped crystal in figure 6.21b. It is barely visible on the lower right corner of the bare surface in figure 6.21a at the 11.5 cm mark. The grayed kill bits are set to exclude large fractions of dark counts that are enhanced by the high overvoltage while recording, but are anyways on a high level because of the operation at room temperature.

This short measurement points out the potential of CMOS-based SPAD arrays for the detection of scintillation photons on the few 10 µm scale. Even at room temperature, mapping of the small LYSO sample with the IDP4 is possible. Although problems with leakage of the cooling system have to be resolved, it is expected that another image with less noise can be taken soon, taking advantage of cooling and optimized readout settings. The perspective is to test different samples on the detector chip. For this purpose, sources of ionizing particles are planned to be installed within the chamber above the detector. Single scintillation event detection would be a next step for the proof of principle and towards the scint-aTEF.

For the sake of completeness, it should be mentioned that two further setups are under development. The first setup is planned to allow for a standardized characterization of fabricated scintillator samples in course of the development of suitable 2PP resins for the scint-aTEF scintillator grid. It is based on a PMT inside a black box. A holding structure for standardized scintillator samples is already manufactured. The sample can be placed directly on the window of the PMT, where it is optically coupled with optical grease. Properties like the light yield can be quantified and compared to commercial reference scintillators with well-known properties.

Another setup addresses the radiation hardness of the material. The prospective setup consists of an electron gun, a sample holding structure and a Faraday cup for reference current measurement of the electron gun. The components have to be operated in vacuum. Defined doses of electrons at certain energies are planned to be emitted onto the target (scintillator sample). This procedure allows for an estimation of potential long-term effects of the impinging electron flux on the material; the samples can be investigated with the PMT-based setup.

7. Conclusion and Outlook

The current background level of in the KATRIN experiment, exceeding the design value by more than a magnitude, is identified as the major barrier in achieving the design sensitivity on the neutrino mass. Based on numerous works, characteristics of the responsible remaining background have been worked out and allow for the elaboration of responsible processes and potential mitigation and discrimination techniques, but also further ways to investigate its properties.
From the Rydberg model of neutral messenger particle-induced background, it follows that such background electrons have small gyroradii (and small pitch angles) at the FPD. This is in contrast to tritium beta decay electrons with large pitch angles and radii. Hence, the principle of transverse energy-dependent filtering is proposed as a method of discrimination. With both versions, the p- and aTEF, it opens up the possibility to investigate the guided electron flux in terms of its angular distribution on the one hand, and to even increase the SBR by active background rejection on the other hand.

In this work, both applications are investigated. At first, the central subject of transverse energy filtering, the angular distributions of background electrons, are studied in detail. The relation of starting energy and final angle is worked out as well as the dependence on the retarding voltage. For both Rydberg-mediated and radon-induced background, simulations are carried out and applicable angular PDFs are established. Both background contributions show somewhat complementary angular distributions: while electrons generated according to the common Rydberg state-induced mechanism feature pitch angles in the few degree regime, electrons from radon decays are more likely to be found with large angles towards the acceptance angle θ_{max}, resembling beta electrons in doing so. This could be exploited in the first pTEF measurement campaign by tuning the radon contributions. Moreover, the effect of retarding potential and LFCS setting (in terms of the minimum magnetic field) is presented and also serves as a more easy way to tune the assumed angular distributions, thus directly affecting the interaction with a TEF structure.
The obtained distributions can be used for transmission studies or the interpretation of acquired data. Therefore, the generators can be equipped with more precise spatial and different energetic distributions, similar to what is performed in this work. However, systematic effects like scattering and the uncertainties in the basic assumptions and Kassiopeia simulations of the background electrons have to be taken into account.
For the first pTEF, purely geometric systematics (mainly addressing the OAR) are found to be controllable on the few percent scale. After characterization of the actual first pTEF's dents, their OAR-related effect can also be estimated based on the findings presented here. In case of the 2pTEF, a more complex configuration space is discussed for similar systematics. Translational misalignment can cause the OAR to decrease by about 10 %. Moiré-related systematics due to azimuthal misalignment are not considered but might introduce macroscopic inhomogeneities. For the actual transmission, the simulations reveal a strong pTEF effect to distinguish between

model background and signal electrons, manifesting itself in a reduction by a factor of 5.39 ± 0.10. Behind the 2pTEF an even stronger effect of 10.7 ± 0.4 is observed. The "cyclotron effect" of trajectories curving around the 2nd grid points towards further systematic effects.
For an extensive analysis of the data from the first pTEF campaign, it should be referred to [Hin22], where details on the transmission behavior and the implications for the KATRIN background model are discussed.

In the aTEF application case, the novel concept of a scint-aTEF is introduced and a simulation environment is set up, wherein BC-404 and PMMA serve as example plastics for the scintillator and passive layer. The parameters can be adjusted to the prospective material used which is expected to have similar properties. The underlying technique of 2PP lithography already allows for the production of microstructured plastic grids and is planned to find application in the production of the required scintillator grids. Samples (fabricated at the APH) indicate surface properties that do practically not affect the overall light collection on the detector surface in the simulations. However, the trapping efficiency gets worse and a slightly increasing spread of light is observed. To also account for the presented dependence of the collection efficiency and detectable pattern on the origin position of the photons as well, the actual scintillation process is incorporated in the simulations. In case of 20 keV kinetic energy, incident electrons with large pitch angles (like beta electrons) experience backscattering on the few percent level. The intruding major fraction deposits its entire energy on tracks penetrating less than 10 µm deep. Thus, the foreseen scint-aTEF dimensions are sufficient.
CMOS-based SPAD arrays are introduced as an appropriate detector system. Potential detector responses are established, including the actual layout of the SPAD array and its quantum efficiency. The obtained signatures of incident electrons are investigated and show the expected correlation with the scintillator grid on top, indeed. For the dedicated detector layout with enhanced sensitivity below the grid, the architecture is optimized to a preliminary configuration of 6 sensitive pixels with $75 \times 25.2\,\mu\mathrm{m}^2$ below each wall and $75 \times 75\,\mu\mathrm{m}^2$ pixels in the corners. In addition, trigger groups are proposed to discriminate common dark counts of the detector array. The required circuitry is located in the less illuminated free space in the channel centers. It is supposed to trigger on events with at least 2 (or 3) activated SPADs within a time frame of $\Delta t \lesssim 100\,\mathrm{ns}$, giving rise to a trigger efficiency $\varepsilon_{\mathrm{trig}}$ of 0.98 ± 0.03 (0.96 ± 0.03). This efficiency is just one of the discussed contribution to the overall PDE.
For further studies of the discrimination performance in an actual aTEF application, the Geant4 simulation code can be extended and adjusted. This is also true for the separate script for the evaluation of the detector response. Anyways, experimental examination of the components and a proof of principle have yet to be provided.
The current efforts to arrange a cooled setup for the IDP4 (ZITI) and future detectors is supposed to reduce the dark counts by 4 orders of magnitude (from room temperature to about −60 °C). Accumulative mapping of an intrinsically radioactive LYSO crystal onto the IDP4 at room temperature is achieved. Single-event detection would be a next step in proving the concept. The test setup is also planned to serve for testing scint-aTEF samples with sources of ionizing radiation.
A key subject to R&D is the scintillator grid. Resins with sufficient properties for 2PP 3D printing will be investigated in cooperation with the APH. Their light yield, guiding properties and radiation hardness are planned to be investigated in two dedicated experimental setups.

Appendix

A. Chapter 3

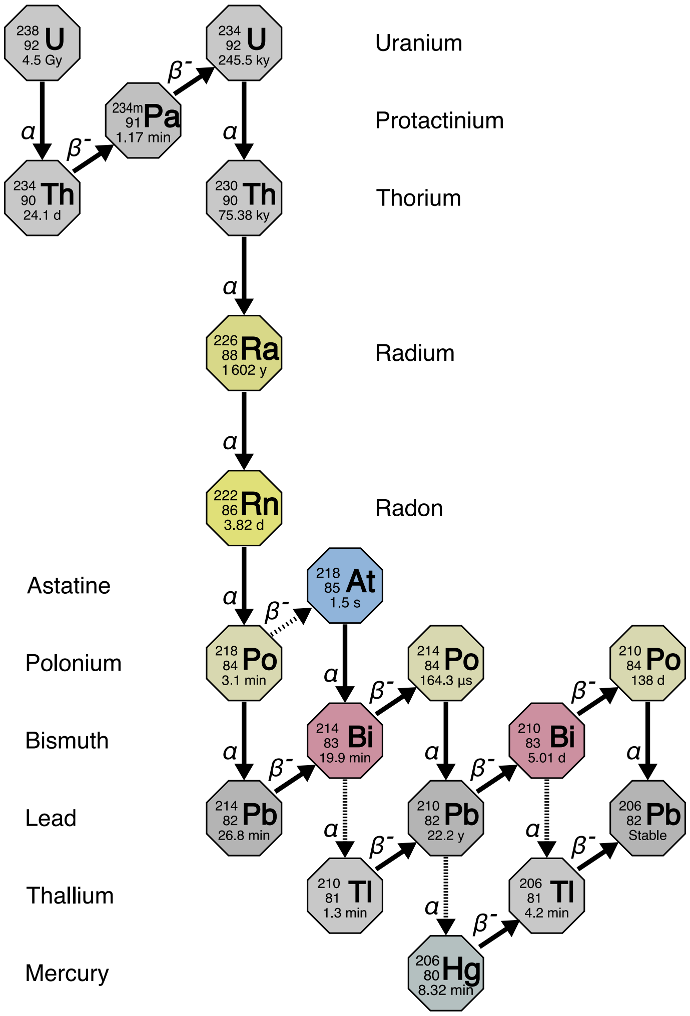

Figure A.1.: Uranium-238 decay chain (from [Wik15]): The half-life is provided in the lowermost line of each octagon. Dashed arrows indicate less probable decay channels.

B. Chapter 5

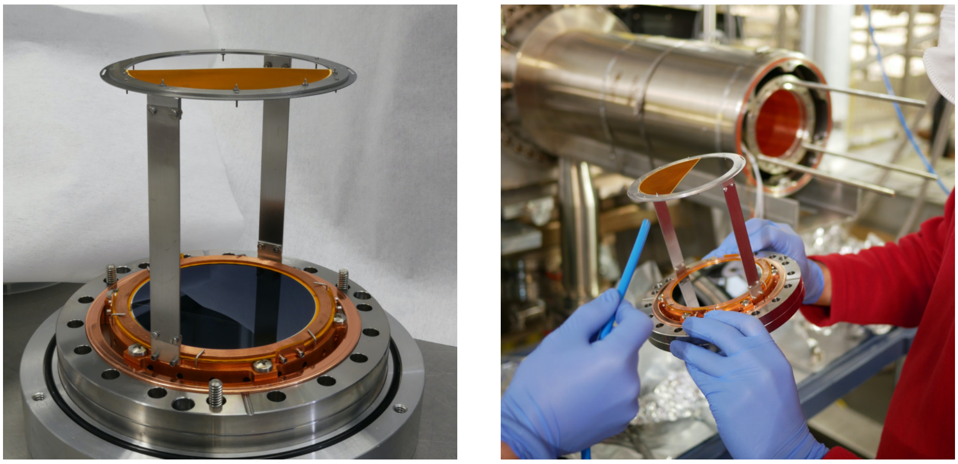

(a)

(b)

Figure B.2.: Installation of the first pTEF: Figure a: pTEF in the holding structure above the FPD wafer. Figure b: Another view of the FPD wafer and the pTEF. In the background, the detector flange at the end of the KATRIN beamline can be seen, where the detector is installed again after recording of the picture.

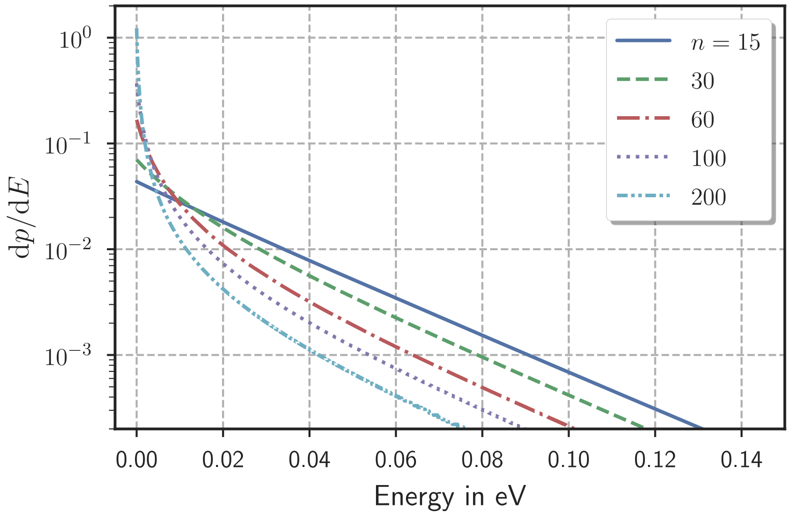

Figure B.3.: Energy distributions of electrons from BBR photo-ionization of Rydberg states (from [Tro19]): The differential energy spectrum is provided for states with varying principal quantum number n (and $\ell = 1$). Photo-ionization occurs due to photons of 293 K BBR.

The XML configuration of the LFCS air coil currents for the three LFCS settings (6.0 G, 4.0 G and 2.7 G) used in this work is provided in the following:

```xml
<if condition="{[ac_setting] eq 6.0}"><!-- 6.0G for 70% w/ eLFCS -->
    <warning value="Using scaled KNM2 air-coil setting for 6.0G"/>
    <external_define name="elfcs_1_current" value="50.8"/> <!-- ac_1 -->
    <external_define name="elfcs_2_current" value="0.0"/>
    <external_define name="elfcs_3_current" value="44.6"/> <!-- ac_2 -->
    <external_define name="elfcs_4_current" value="{79.5*(8.0/14.0)}"/> <!-- ac_3 -->
    <external_define name="elfcs_5_current" value="{43.0*(8.0/14.0)}"/> <!-- ac_4 -->
    <external_define name="elfcs_6_current" value="{64.8*(8.0/14.0)}"/> <!-- ac_5 -->
```

```
    <external_define name="elfcs_7_current" value="{25.7*(8.0/14.0)}"/> <!-- ac_6 -->
    <external_define name="elfcs_8_current" value="52.8"/> <!-- ac_7 -->
    <external_define name="elfcs_9_current" value="34.9"/> <!-- ac_8 -->
    <external_define name="elfcs_10_current" value="38.7"/> <!-- ac_9 -->
    <external_define name="elfcs_11_current" value="9.2"/> <!-- ac_10 -->
    <external_define name="elfcs_12_current" value="35.9"/> <!-- ac_11 -->
    <external_define name="elfcs_13_current" value="92.7"/> <!-- ac_12 -->
    <external_define name="elfcs_14_current" value="13.2"/> <!-- ac_13 -->
    <external_define name="elfcs_15_current" value="0.0"/>
    <external_define name="elfcs_16_current" value="0.0"/> <!-- ac_14 -->
    <external_define name="elfcs_17_current" value="0.0"/> <!-- ac_15 == ac_14 -->
    <external_define name="elfcs_18_current" value="0.0"/>
    <external_define name="elfcs_19_current" value="0.0"/>
    <external_define name="elfcs_20_current" value="0.0"/>
</if>

<if condition="{[ac_setting] eq 4.0}"><!-- 4.0G for 70% w/ eLFCS -->
    <external_define name="elfcs_1_current" value="0.0"/> <!-- ac_1 -->
    <external_define name="elfcs_2_current" value="0.0"/>
    <external_define name="elfcs_3_current" value="5.0"/> <!-- ac_2 -->
    <external_define name="elfcs_4_current" value="15.0"/> <!-- ac_3 -->
    <external_define name="elfcs_5_current" value="18.0"/> <!-- ac_4 -->
    <external_define name="elfcs_6_current" value="21.0"/> <!-- ac_5 -->
    <external_define name="elfcs_7_current" value="25.0"/> <!-- ac_6 -->
    <external_define name="elfcs_8_current" value="28.0"/> <!-- ac_7 -->
    <external_define name="elfcs_9_current" value="28.0"/> <!-- ac_8 -->
    <external_define name="elfcs_10_current" value="26.0"/> <!-- ac_9 -->
    <external_define name="elfcs_11_current" value="18.0"/> <!-- ac_10 -->
    <external_define name="elfcs_12_current" value="16.0"/> <!-- ac_11 -->
    <external_define name="elfcs_13_current" value="13.0"/> <!-- ac_12 -->
    <external_define name="elfcs_14_current" value="0.0"/> <!-- ac_13 -->
    <external_define name="elfcs_15_current" value="0.0"/>
    <external_define name="elfcs_16_current" value="0.0"/> <!-- ac_14 -->
    <external_define name="elfcs_17_current" value="0.0"/> <!-- ac_15 == ac_14 -->
    <external_define name="elfcs_18_current" value="0.0"/>
    <external_define name="elfcs_19_current" value="0.0"/>
    <external_define name="elfcs_20_current" value="0.0"/>
    <external_define name="emcs_x_offset" value="-4.8"/> <!-- reference 4.8 A | optimized 0.0 A | offset -4.8A -->
    <external_define name="emcs_y_offset" value="-7.4"/> <!-- reference 52.4 A | optimized 45.0 A | offset -7.4A -->
    <redefine name="has_ac_setting" value="1"/>
</if>

<if condition="{[ac_setting] eq 2.7}"><!-- 2.7G for 70% w/ eLFCS -->
    <warning value="Using scaled KNM2 air-coil setting for 2.7G"/>
    <external_define name="elfcs_1_current" value="0.0"/> <!-- ac_1 -->
    <external_define name="elfcs_2_current" value="0.0"/>
    <external_define name="elfcs_3_current" value="5.0"/> <!-- ac_2 -->
    <external_define name="elfcs_4_current" value="{0.0}"/> <!-- ac_3 -->
    <external_define name="elfcs_5_current" value="{0.0}"/> <!-- ac_4 -->
    <external_define name="elfcs_6_current" value="{10.0*(8.0/14.0)}"/> <!-- ac_5 -->
    <external_define name="elfcs_7_current" value="{17.0*(8.0/14.0)}"/> <!-- ac_6 -->
    <external_define name="elfcs_8_current" value="27.0"/> <!-- ac_7 -->
    <external_define name="elfcs_9_current" value="30.0"/> <!-- ac_8 -->
    <external_define name="elfcs_10_current" value="3.0"/> <!-- ac_9 -->
    <external_define name="elfcs_11_current" value="9.0"/> <!-- ac_10 -->
    <external_define name="elfcs_12_current" value="5.3"/> <!-- ac_11 -->
    <external_define name="elfcs_13_current" value="10.7"/> <!-- ac_12 -->
```

```
    <external_define name="elfcs_14_current" value="-22.0"/> <!-- ac_13 -->
    <external_define name="elfcs_15_current" value="0.0"/>
    <external_define name="elfcs_16_current" value="0.0"/> <!-- ac_14 -->
    <external_define name="elfcs_17_current" value="0.0"/> <!-- ac_15 == ac_14 -->
    <external_define name="elfcs_18_current" value="0.0"/>
    <external_define name="elfcs_19_current" value="0.0"/>
    <external_define name="elfcs_20_current" value="0.0"/>
    <external_define name="emcs_x_offset" value="-5.1"/> <!-- reference 5.1 A | optimized
        0.0 A | offset -5.1A -->
    <external_define name="emcs_y_offset" value="-6.5"/> <!-- reference 51.5 A | optimized
         45.0 A | offset -6.5A -->
    <redefine name="has_ac_setting" value="1"/>
</if>
```

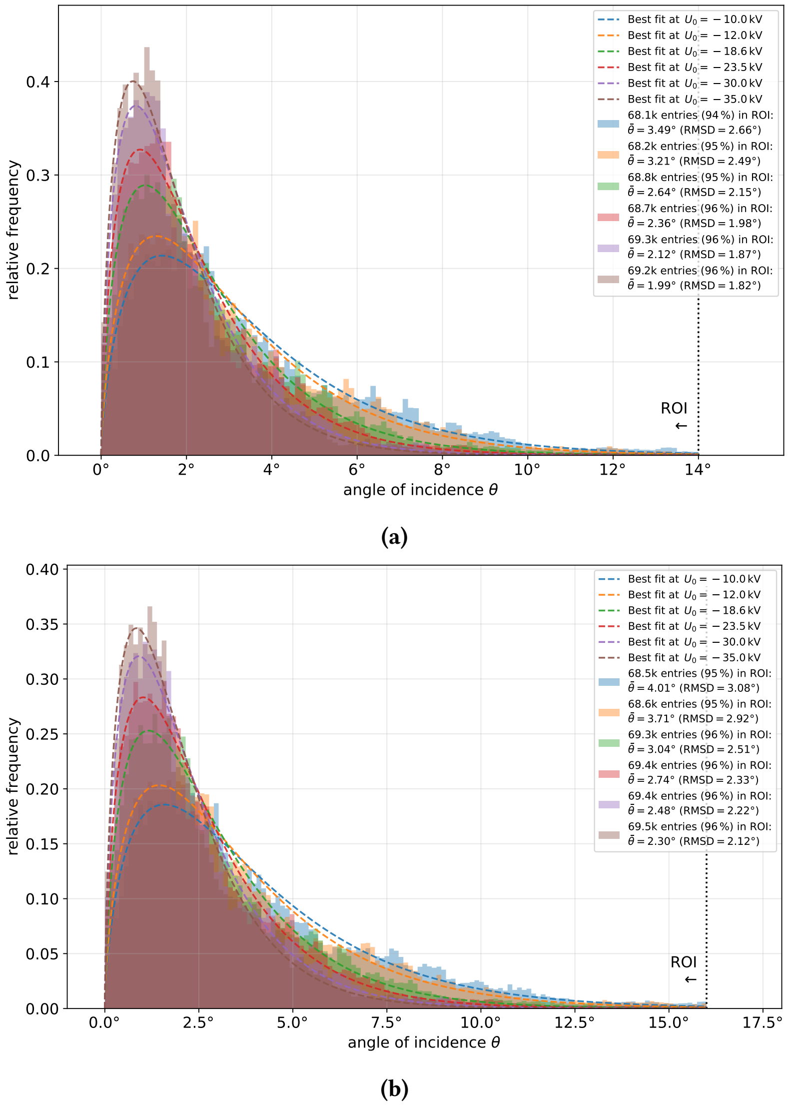

(a)

(b)

Figure B.4.: Angular distributions and PDF fits of Rydberg-mediated background at 4.0 G and 2.7 G LFCS setting: The binned relative number of electrons is plotted over their pitch angle θ (similar to fig. 5.5). 10^5 Rydberg state-induced electrons are initialized for each setting. The fits for the PDFs $\mathrm{d}\mathcal{P}/\mathrm{d}\theta(\theta)$ with the gamma distribution (eq. 5.6) are also shown (parameters in tab. 5.1). Figure a: 4.0 G setting. Figure b: 2.7 G setting.

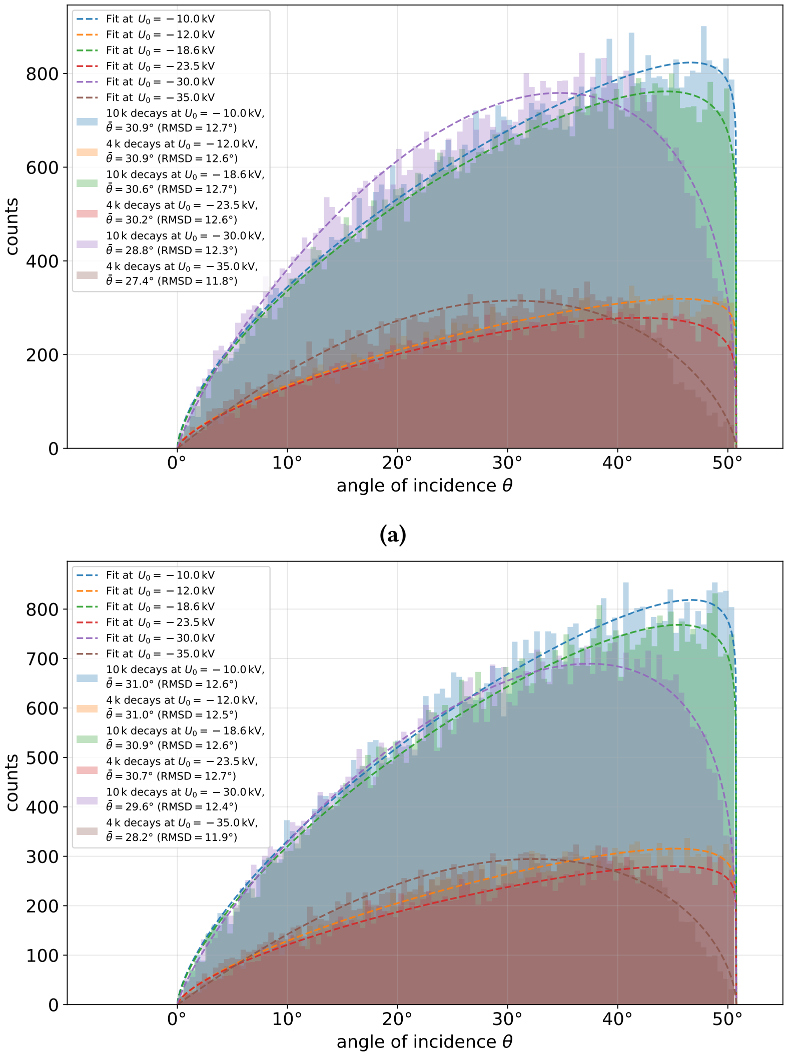

(a)

(b)

Figure B.5.: Angular distributions and PDF fits of radon-induced background at 4.0 G and 2.7 G LFCS setting: The binned number of electrons is plotted over their pitch angle θ (similar to fig. 5.8). 10^4 (4×10^3) ^{219}Rn decays are initialized for the three upper (lower) curves. The fits with eq. 5.8 are also displayed (parameters in tab. 5.2) Figure a: 4.0 G setting. Figure b: 2.7 G setting.

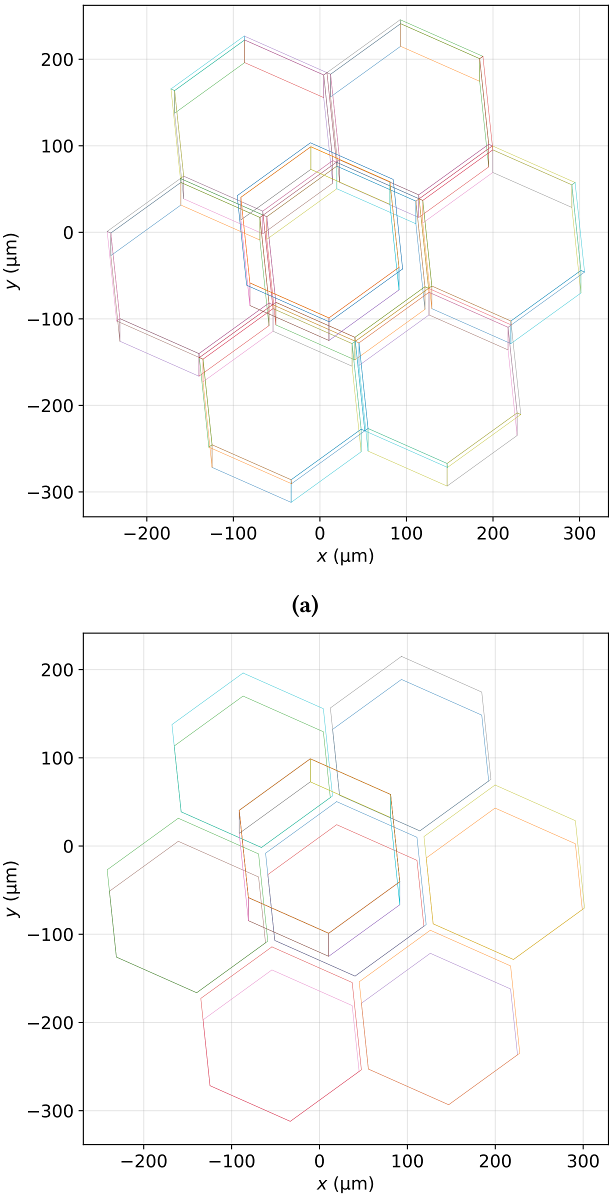

(a)

(b)

Figure B.6.: (2)pTEF model for geometric studies: A hexagonal cell of the 1st pTEF grid is located in the distance $\Delta z = 500\,\mu\text{m}$ in front of the 2nd grid, consisting of seven cells (number can be set arbitrarily). Both layers are tilted by $\theta = 6°$ and rotated by $\varphi = 6°$ for better visualization. Additionally, the 2nd layer is shifted 30 µm in both the x- and y-direction. While all of the geometry's relevant aspects are depicted in figure a, the shadows which are created by the 2nd pTEF are displayed in figure b, allowing for a precise study of the structure's OAR.

C. Chapter 6

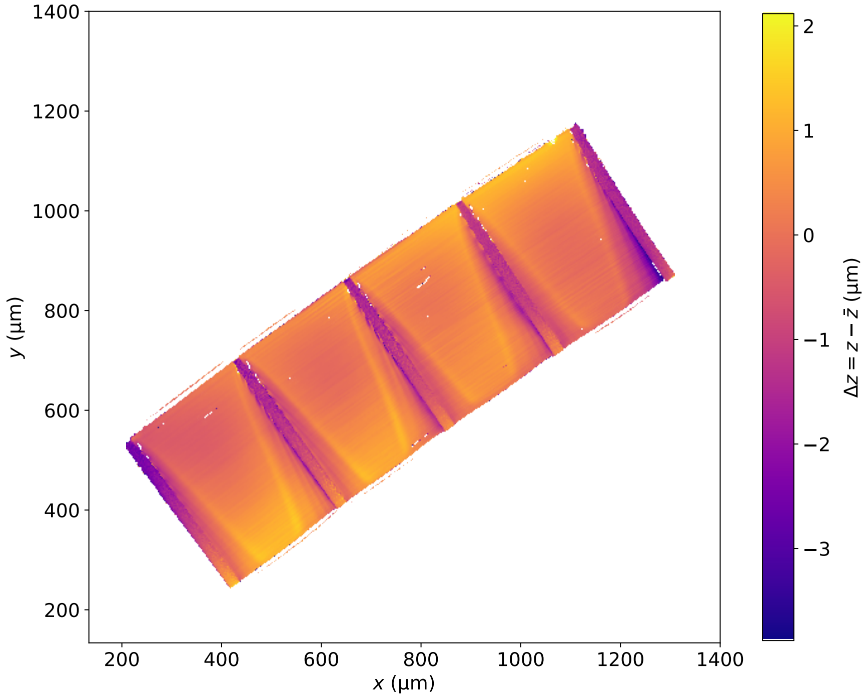

Figure C.7.: Confocal microscopy of a microstructured sample grid (data from the APH): Microscopic data from the outer wall surface of a plastic sample 4 × 4 grid from non-scintillating plastic (cf. fig. 6.5), produced by 2PP lithography at the APH, are plotted to reveal the surface height (z) profile. The profile is provided in terms of the local deviation Δz from the average height $\bar{z}$.

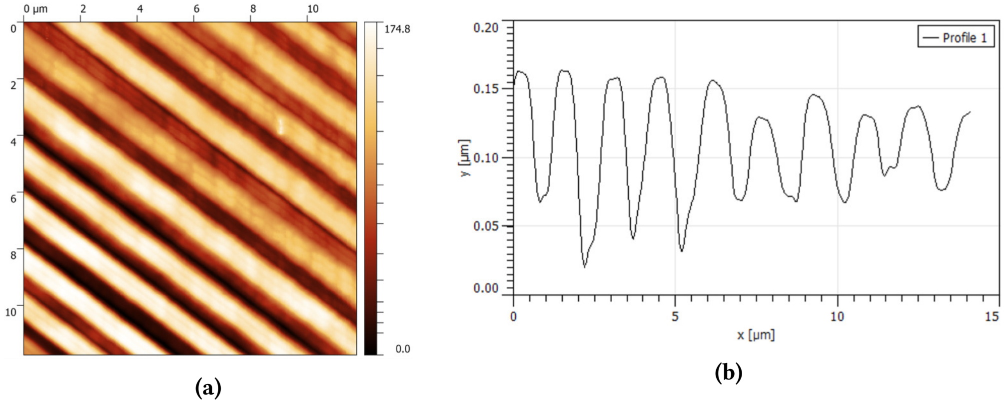

(a)

(b)

Figure C.8.: AFM investigation of a microstructured sample grid (recorded by the CFN): Figure a: This image is to be read similar to fig. C.7. It shows a high resolution detail of a surface region which exhibits very irregular surface properties. Figure b: The surface height (y) profile along a line (coordinate x) perpendicular to the ridges in fig. a is displayed.

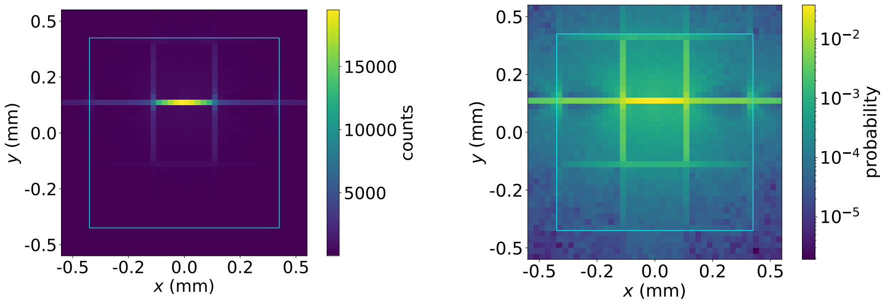

(a) **(b)**

Figure C.9.: Photon distribution on detector surface without PMMA layers: The distribution of 10^6 simulated photons across the detector surface is provided in $25 \times 25\,\mu\text{m}^2$ bins. The outer edges of the 3 × 3 scintillator grid (with rough surface, $\sigma_\alpha = 5°$) on the detector surface are indicated in light blue. Figure a: Photon distribution. Figure b: Logarithmic probability map.

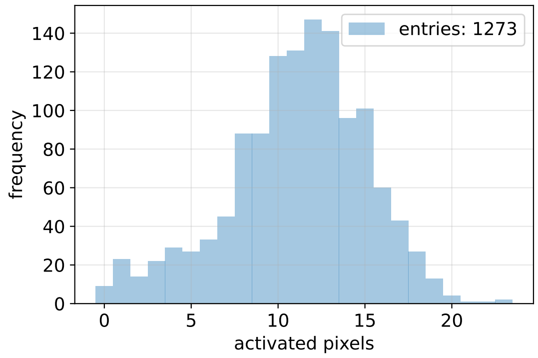

Figure C.10.: Activated pixel numbers for scintillation events: The histogram contains the numbers of activated pixels in events, where incident electrons with $E = 20\,\text{keV}$ hit the structure, inducing scintillation photons which are actually guided onto the detector, in addition. Detector layout is the dedicated scint-aTEF layout (fig. 6.14b).

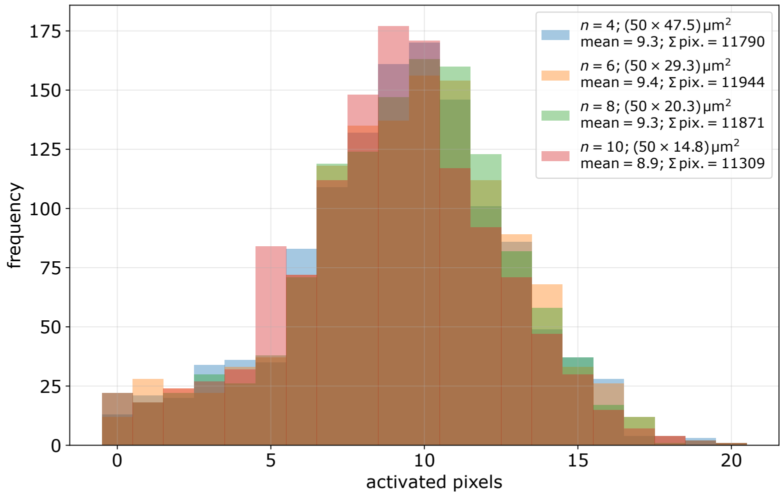

Figure C.11.: Activated pixel numbers under variation of SPAD array pixel number: The number of activated pixels in events that result in photons on the detector is shown. The pixel width in the dedicated layout (fig. 6.14b) is fixed to $75\,\mu\text{m}$. The pixel number n and therefore their height is varied, while preserving the required dead space d_{dead} between neighboring SPADs (corners remain at $75 \times 75\,\mu\text{m}^2$).

Bibliography

[A$^+$01] SNO Collaboration: Q. R. Ahmad *et al.*: *Measurement of the Rate of $\nu_e + d \longrightarrow p + p + e^-$ Interactions Produced by ^8B Solar Neutrinos at the Sudbury Neutrino Observatory.* Physical Review Letters, 87(7):071301, July 2001. `https://doi.org/10.1103/PhysRevLett.87.071301`.

[A$^+$03] S. Agostinelli *et al.*: *Geant4 – a simulation toolkit.* Nuclear Instruments and Methods in Physics Research Section A: Accelerators, Spectrometers, Detectors and Associated Equipment, 506:250–303, July 2003. `https://doi.org/10.1016/S0168-9002(03)01368-8`.

[A$^+$06] ALEPH, DELPHI, L3 and OPAL Collaboration *et al.*: *Precision Electroweak Measurements on the Z Resonance.* Physics Reports, 427:257–454, May 2006. `https://doi.org/10.1016/j.physrep.2005.12.006`.

[A$^+$11] V. N. Aseev *et al.*: *Upper limit on the electron antineutrino mass from the Troitsk experiment.* Physical Review D, 84:112003, December 2011. `https://doi.org/10.1103/PhysRevD.84.112003`.

[A$^+$17] N. Abgrall *et al.*: *The large enriched germanium experiment for neutrinoless double beta decay (LEGEND).* AIP Conference Proceedings, 1894:020027, October 2017. `https://doi.org/10.1063/1.5007652`.

[A$^+$18] H. Alva-Sánchez *et al.*: *Understanding the intrinsic radioactivity energy spectrum from ^{176}Lu in LYSO/LSO scintillation crystals.* Scientific Reports, 8:17310, November 2018. `https://doi.org/10.1038/s41598-018-35684-x`.

[A$^+$19a] K. Altenmüller *et al.*: *Muon-induced background in the KATRIN main spectrometer.* Astroparticle Physics, 108:40–49, March 2019. `https://doi.org/10.1016/j.astropartphys.2019.01.003`.

[A$^+$19b] MAJORANA Collaboration: S. I. Alvis *et al.*: *Search for neutrinoless double-β decay in ^{76}Ge with 26 kg yr of exposure from the Majorana Demonstrator.* Physical Review C, 100:025501, August 2019. `https://doi.org/10.1103/PhysRevC.100.025501`.

[A$^+$20a] Planck Collaboration: N. Aghanim *et al.*: *Planck 2018 results.* Astronomy & Astrophysics, 641(A6):1–67, September 2020. `https://doi.org/10.1051/0004-6361/201833910`.

[A$^+$20b] GERDA Collaboration: M. Agostini *et al.*: *Final Results of GERDA on the Search for Neutrinoless Double-β Decay.* Physical Review Letters, 125:252502, December 2020. `https://doi.org/10.1103/PhysRevLett.125.252502`.

[A$^+$20c] M. Aker *et al.*: *Suppression of Penning discharges between the KATRIN spectrometers.* The European Physical Journal C, 80:821, September 2020. `https://doi.org/10.1140/epjc/s10052-020-8278-y`.

[A$^+$20d] P. Arce *et al.*: *Report on G4-Med, a Geant4 benchmarking system for medical physics applications developed by the Geant4 Medical Simulation Benchmarking Group.* Medical Physics, 48(1):19–56, May 2020. `https://doi.org/10.1002/mp.14226`.

[A$^+$21a] LEGEND Collaboration: N. Abgrall *et al.*: *LEGEND-1000 Preconceptual Design Report*, July 2021. `https://doi.org/10.48550/arXiv.2107.11462`.

[A$^+$21b] The KATRIN Collaboration: M. Aker *et al.*: *Analysis methods for the first KATRIN neutrino-mass measurement.* Physical Review D, 104:012005, July 2021. `https://doi.org/10.1103/PhysRevD.104.012005`.

[A$^+$21c] The KATRIN Collaboration: M. Aker *et al.*: *The design, construction, and commissioning of the KATRIN experiment.* Journal of Instrumentation, 16(8):T08015, August 2021. `https://doi.org/10.1088/1748-0221/16/08/T08015`.

[A$^+$22] The KATRIN Collaboration: M. Aker *et al.*: *Direct neutrino-mass measurement with sub-electronvolt sensitivity.* Nature Physics, 18:160–166, February 2022. `https://doi.org/10.1038/s41567-021-01463-1`.

[Ahm09] R. Ahmed: *Optical Study on Poly(methyl methacrylate)/Poly(vinyl acetate) Blends.* International Journal of Photoenergy, 2009:50389, January 2009. `https://doi.org/10.1155/2009/150389`.

[AWP16] AWP – Rohstoff GmbH: *Datenblatt – PMMA Acryrex*, February 2016. `https://awp-rohstoffe.de/wp-content/uploads/2018/08/dat_pmma_acryrex_uebersicht.pdf`, visited on July 5th, 2022.

[B$^+$63] J. N. Bahcall *et al.*: *Solar Neutrino Flux.* Astrophysical Journal, 137(1):344–346, January 1963. `https://doi.org/10.1086/147513`.

[B$^+$87] R. Burn *et al.*: *GEANT 3: user's guide Geant 3.10, Geant 3.11.* CERN, Geneva, September 1987. `https://cds.cern.ch/record/1119728`.

[B$^+$20] S. Berns *et al.*: *A novel polystyrene-based scintillator production process involving additive manufacturing.* Journal of Instrumentation, 15(10):P10019, October 2020. `https://doi.org/10.1088/1748-0221/15/10/p10019`.

[Bah64] J. N. Bahcall: *Solar Neutrinos. I. Theoretical.* Physical Review Letters, 12(11):300–302, March 964. `https://doi.org/10.1103/PhysRevLett.12.300`.

[Bar17] J. P. Barrett: *A spatially resolved study of the KATRIN main spectrometer using a novel fast multipole method.* PhD thesis, Massachusetts Institute of Technology (MIT), 2017. `http://hdl.handle.net/1721.1/114314`.

[BB90] J. N. Bahcall and H. A. Bethe: *A Solution of the Solar-Neutrino Problem.* Physical Review Letters, 65(18):2233–2235, October 1990. `https://doi.org/10.1103/PhysRevLett.65.2233`.

[Bec96] A. H. Becquerel: *Sur les radiations invisibles émises par les corps phosphorescents.* Comptes rendus de l'Académie des sciences, 122, February & March 1896. `http://www.bibnum.education.fr/physique/radioactivite/sur-les-radiations-invisibles-emises-par-les-corps-phosphorescents`.

[Beh16] J. D. Behrens: *Design and commissioning of a monoenergetic photoelectron source and active background reduction by magnetic pulse at the KATRIN experiment.* PhD thesis, Westfälische Wilhelms-Universität Münster (WWU), 2016. `https://www.katrin.kit.edu/publikationen/phd_behrens.pdf`.

[Bir51] J. B. Birks: *Scintillations from Organic Crystals: Specific Fluorescence and Relative Response to Different Radiations.* Proceedings of the Physical Society. Section A, 64(10):874–877, October 1951. `https://doi.org/10.1088/0370-1298/64/10/303`.

[Bir60] J. B. Birks: *The Scintillation Process in Organic Systems.* IRE Transactions on Nuclear Science, 7:2–11, June 1960. `https://doi.org/10.1109/TNS2.1960.4315726`.

[Blo17] F. Block: *Characterisation of the Background in the KATRIN Experiment.* Master's thesis, Karlsruher Institut für Technologie (KIT), April 2017. `https://www.katrin.kit.edu/publikationen/mth_fblock.pdf`.

[BP34] H. A. Bethe and R. Peierls: *The "Neutrino".* Nature, 133:532, April 1934. `https://doi.org/10.1038/133532a0`.

[Cha14] J. Chadwick: *Intensitätsverteilung im magnetischen Spektren der β-Strahlen von Radium $B + C$.* Verhandlungen der Deutschen Physikalischen Gesellschaft, 16:383–391, 1914. `http://cds.cern.ch/record/262756?ln=de`.

[CR+56] C. L. Cowan, Jr., F. Reines, *et al.*: *Detection of the Free Neutrino: a Confirmation.* Science, 124(3212):103–104, July 1956. `https://doi.org/10.1126/science.124.3212.103`.

[CSS13] B. Chandar Shekar, S. Sathish, and R. Sengoden: *Spin Coated Nano Scale PMMA Films for Organic Thin Film Transistors.* Physics Procedia, 49:145–157, 2013. `https://doi.org/10.1016/j.phpro.2013.10.021`, BRNS, AICTE, DST, CSIR and ISRO sponsored National Conference on Spintronic Materials: Nanostructures and Devices (SMND-2011).

[D+62] G. Danby *et al.*: *Observation of High-Energy Neutrino Reactions and the Existence of Two Kinds of Neutrinos.* Physical Review Letters, 9(36):36–44, July 1962. `https://doi.org/10.1103/PhysRevLett.9.36`.

[D+90] ALEPH Collaboration: D. Decamp *et al.*: *A precise determination of the number of families with light neutrinos and of the Z boson partial widths.* Physical Letters B, 235:399–411, February 1990. `https://doi.org/10.1016/0370-2693(90)91984-J`.

[D+98] R. Davis, Jr. *et al.*: *Measurement of the Solar Electron Neutrino Flux with the Homestake Chlorine Detector.* The Astrophysical Journal, 496(1):505–526, March 1998. `https://doi.org/10.1086/305343`.

[Dav94] R. Davis: *A review of the Homestake solar neutrino experiment.* Progress in Particle and Nuclear Physics, 32:13–32, 1994. `https://doi.org/10.1016/0146-6410(94)90004-3`.

[Dem13] W. Demtröder: *Experimentalphysik 2 – Elektrizität und Optik.* Springer-Lehrbuch. Springer Berlin, Heidelberg, 2013, ISBN 978-3-642-29944-5. `https://doi.org/10.1007/978-3-642-29944-5`.

[E+20] I. Esteban *et al.*: *The fate of hints: updated global analysis of three-flavor neutrino oscillations.* Journal of High Energy Physics, 2020(178), September 2020. `https://doi.org/10.1007/JHEP09(2020)178`.

[E⁺22] Project 8 Collaboration: A. Esfahani *et al.*: *The Project 8 Neutrino Mass Experiment*, March 2022. `https://doi.org/10.48550/arXiv.2203.07349`.

[EHM87] S. R. Elliott, A. A. Hahn, and M. K. Moe: *Direct evidence for two-neutrino double-beta decay in ^{82}Se.* Physical Review Letters, 59:2020–2023, November 1987. `https://doi.org/10.1103/PhysRevLett.59.2020`.

[F⁺98] Super-Kamiokande Collaboration: Y. Fukada *et al.*: *Evidence for Oscillation of Atmospheric Neutrinos.* Physical Review Letters, 81:1562–1567, August 1998. `https://doi.org/10.1103/PhysRevLett.81.1562`.

[F⁺14] F. M. Fränkle *et al.*: *Penning discharge in the KATRIN pre-spectrometer.* Journal of Instrumentation, 9(7):P07028, July 2014. `https://doi.org/10.1088/1748-0221/9/07/P07028`.

[F⁺15] E. Ferri *et al.*: *The Status of the MARE Experiment with ^{187}Re and ^{163}Ho Isotopes.* Physics Procedia, 61:227–231, 2015. `https://doi.org/10.1016/j.phpro.2014.12.037`, 13th International Conference on Topics in Astroparticle and Underground Physics, TAUP 2013.

[F⁺17a] The KATRIN Collaboration: F. M. Fränkle *et al.*: *Background processes in the KATRIN main spectrometer.* Journal of Physics: Conference Series, 888:012070, September 2017. `https://doi.org/10.1088/1742-6596/888/1/012070`.

[F⁺17b] D. Furse *et al.*: *Kassiopeia: a modern, extensible C++ particle tracking package.* New Journal of Physics, 19(053012), May 2017. `https://doi.org/10.1088/1367-2630/aa6950`.

[F⁺22] F. M. Fränkle *et al.*: *KATRIN background due to surface radioimpurities.* Astroparticle Physics, 138:102686, May 2022. `https://doi.org/10.1016/j.astropartphys.2022.102686`.

[Faj13] K. Fajans: *Die radioaktiven Umwandlungen und das periodische System der Elemente.* Berichte der Deutschen Chemischen Gesellschaft, 46(1):422–439, January 1913. `https://doi.org/10.1002/cber.19130460162`.

[Fer33] E. Fermi: *Tentativo di una teoria dell'emissione dei raggi "beta".* La Ricerca Scientifica, II(12):491–495, December 1933. `https://www.phys.uniroma1.it/DipWeb/museo/collezione%20Fermi/documento1.htm`.

[Fer34] E. Fermi: *Tentativo di una Teoria dei Raggi β.* Nuovo Cimento, 11(1):1924–1942, 1934. `https://doi.org/10.1007/BF02959820`.

[Fis22] P. Fischer: *ASICs for Photon Detection Integrating Avalanche Diodes and CMOS Readout.* In *14th Terascale Detector Workshop 2022.* Institute of Computer Engineering (ZITI), Heidelberg University, February 2022. `https://indico.desy.de/event/32537/contributions/114362/attachments/71831/91764/2022_TeraScale_Fischer.pdf`.

[Frä10] F. M. Fränkle: *Background Investigations of the KATRIN Pre-Spectrometer.* PhD thesis, Karlsruher Institut für Technologie (KIT), 2010. `https://doi.org/10.5445/IR/1000019392`.

[Frä22] F. M. Fränkle: *Background Report*, March 2022. `https://indico.scc.kit.edu/event/2530/contributions/9951/attachments/4866/7344/Background_Fraenkle_CM42.pdf`, visited on July 5th, 2022, In *42nd KATRIN Collaboration Meeting.*

[G+17] L. Gastaldo *et al.*: *The electron capture in ^{163}Ho experiment – ECHo.* The European Physical Journal Special Topics, 226:1623–1694, June 2017. `https://doi.org/10.1140/epjst/e2017-70071-y`.

[G+18] S. Görhardt *et al.*: *Impact of a cryogenic baffle system on the suppression of radon-induced background in the KATRIN Pre-Spectrometer.* Journal of Instrumentation, 13(10):T10004, October 2018. `https://doi.org/10.1088/1748-0221/13/10/t10004`.

[G+22] K. Gauda *et al.*: *An active transverse energy filter to differentiate low energy particles with large pitch angles in a strong magnetic field*, March 2022. `https://doi.org/10.48550/ARXIV.2203.06085`.

[Gal94] T. F. Gallagher: *Rydberg Atoms.* Cambridge Monographs on Atomic, Molecular and Chemical Physics. Cambridge University Press, 1994, ISBN 9780511524530. `https://doi.org/10.1017/CBO9780511524530`.

[Gea21] The Geant4 Collaboration: *Book For Application Developers*, December 2021. `https://geant4-userdoc.web.cern.ch/UsersGuides/ForApplicationDeveloper/html/index.html`, visited on July 5th, 2022.

[Gei22] T. Geigle: *Geant4 simulation studies for scintillating transverse energy filters for KATRIN.* Bachelor's thesis, Karlsruher Institut für Technologie (KIT), May 2022. `https://fuzzy.fzk.de/bscw/bscw.cgi/1390086?op=preview&back_url=831858`, unpublished.

[GL18] M. Gerbino and M. Lattanzi: *Status of Neutrino Properties and Future Prospects – Cosmological and Astrophysical Constraints.* Frontiers in Physics, 5(70), February 2018. `https://doi.org/10.3389/fphy.2017.00070`.

[Gri01] P. K. F. Grieder: *Cosmic Rays at Earth.* Elsevier Science, Juli 2001, ISBN 9780444507105. `https://www.elsevier.com/books/cosmic-rays-at-earth/grieder/978-0-444-50710-5`.

[Gro15] S. Groh: *Modeling of the response function and measurement of transmission properties of the KATRIN experiment.* PhD thesis, Karlsruher Institut für Technologie (KIT), 2015. `https://doi.org/10.5445/IR/1000046546`.

[H+91] K. S. Hirata *et al.*: *Real-time, directional measurement of ^{8}B solar neutrinos in the Kamiokande II detector.* Physical Review D, 44:2241–2260, October 1991. `https://doi.org/10.1103/PhysRevD.44.2241`.

[Ham21] M. Hamel: *Plastic Scintillators - Chemistry and Applications.* Topics in Applied Physics. Springer Cham, Singapore, 2021, ISBN 978-3-030-73488-6. `https://doi.org/10.1007/978-3-030-73488-6`.

[Har15] F. T. Harms: *Characterization and Minimization of Background Processes in the KATRIN Main Spectrometer.* PhD thesis, Karlsruher Institut für Technologie (KIT), 2015. `https://doi.org/10.5445/IR/1000050027`.

[HHL21] D. Hinz, A. Huber, and J. N. Lauer: *pTEF Measurement Proposal.* Measurement proposal, Karlsruher Institut für Technologie (KIT), December 2021. Internal document.

[Hin18] D. Hinz: *Ionisation mechanisms of ^{206}Pb induced Rydberg atoms.* Master's thesis, Karlsruher Institut für Technologie (KIT), October 2018. `https://www.katrin.kit.edu/publikationen/mth-hinz.pdf`.

[Hin22] D. Hinz: *Background systematics and extensions to the KATRIN background model.* PhD thesis, Karlsruher Institut für Technologie (KIT), July 2022.

[Int22] International Atomic Energy Agency: *LiveChart of Nuclides – Advanced version*, April 2022. `https://www.iaea.org/resources/databases/livechart-of-nuclides-advanced-version`, visited on July 5th, 2022.

[JM10] M. Janecek and W. W. Moses: *Simulating Scintillator Light Collection Using Measured Optical Reflectance.* IEEE Transactions on Nuclear Science, 57(3):964–970, June 2010. `https://doi.org/10.1109/TNS.2010.2042731`.

[K⁺01] DONUT Collaboration: K. Kodama *et al.*: *Observation of tau neutrino interactions.* Physics Letters B, 504(3):218–224, April 2001. `https://doi.org/10.1016/S0370-2693(01)00307-0`.

[K⁺05] C. Kraus *et al.*: *Final results from phase II of the Mainz neutrino mass search in tritium β decay.* The European Physical Journal C, 40:447–468, April 2005. `https://doi.org/10.1140/epjc/s2005-02139-7`.

[K⁺19] M. Kleesiek *et al.*: *β-Decay spectrum, response function and statistical model for neutrino mass measurements with the KATRIN experiment.* The European Physical Journal C, 79(204), March 2019. `https://doi.org/10.1140/epjc/s10052-019-6686-7`.

[K⁺20] D.-G. Kim *et al.*: *Performance of 3D printed plastic scintillators for gamma-ray detection.* Nuclear Engineering and Technology, 52(12):2910–2917, December 2020. `https://doi.org/10.1016/j.net.2020.05.030`.

[Kas22] The Kassiopeia developers: *Kassiopeia 3.8 documentation*, July 2022. `http://katrin-experiment.github.io/Kassiopeia/index.html`, visited on July 5th, 2022.

[Kel19] M. Keller: *Development and Application of CMOS based SPAD Arrays.* In *HighRR Review – Poster Contribution.* Institute of Computer Engineering (ZITI), Heidelberg University, June 2019. `https://indico.cern.ch/event/827947/contributions/3476494/attachments/1868245/3088528/MKeller_PosterV3.pdf`.

[KET21] KETEK GmbH: *Product Data Sheet. SiPM – Silicon Photomultiplier*, 2021. `https://www.ketek.net/wp-content/uploads/KETEK-PM33xx-WL-A0-Datasheet.pdf`, visited on July 5th, 2022.

[KIT15] KIT: *Studien- und Prüfungsordnung des Karlsruher Instituts für Technologie (KIT) für den Masterstudiengang Physik*, August 2015. `http://www.physik.kit.edu/Studium/Studienplaene/PrfOrd_phys_msc_2015.pdf`, visited on July 5th, 2022.

[KW16] H. Kolanoski and N. Wermes: *Teilchendetektoren. Grundlagen und Anwendung.* Springer Berlin Heidelberg, 2016, ISBN 9783662453490. `https://www.springer.com/de/book/9783662453490`.

[L⁺22] A. Lokhov *et al.*: *Background reduction at the KATRIN experiment by the shifted analysing plane configuration.* The European Physical Journal C, 82(258), March 2022. `https://doi.org/10.1140/epjc/s10052-022-10220-4`.

[Lei14] B. Leiber: *Investigations of background due to secondary electron emission in the KATRIN-experiment.* PhD thesis, Karlsruher Institut für Technologie (KIT), 2014. `https://doi.org/10.5445/IR/1000042415`.

[LGŠ21] J. N. Lauer, T. Geigle, and M. Šefčík: *asTEF*, November 2021. `https://nuserv.uni-muenster.de:8443/joscha_lauer/astef.git`, visited on July 5th, 2022, Git repository of the scint-aTEF simulations.

[Lin15] J. Linek: *Investigation of the muon induced background at the KATRIN main spectrometer.* Master's thesis, Karlsruher Institut für Technologie (KIT), June 2015. `https://www.katrin.kit.edu/publikationen/mth-Linek.pdf`.

[LL02] T. J. Loredo and D. Q. Lamb: *Bayesian analysis of neutrinos observed from supernova SN 1987A.* Physical Review D, 65:063002, February 2002. `https://doi.org/10.1103/PhysRevD.65.063002`.

[M+93] S. W. Moser *et al.*: *Principles and practice of plastic scintillator design.* Radiation Physics and Chemistry, 41(1):31–36, 1993. `https://doi.org/10.1016/0969-806X(93)90039-W`.

[Mer12] S. Mertens: *Study of Background Processes in the Electrostatic Spectrometers of the KATRIN Experiment.* PhD thesis, Karlsruher Institut für Technologie (KIT), 2012. `https://doi.org/10.5445/IR/1000027058`.

[MNS62] Z. Maki, M. Nakagawa, and S. Sakata: *Remarks on the Unified Model of Elementary Particles.* Progress of Theoretical Physics, 28(5):870–880, November 1962. `https://doi.org/10.1143/PTP.28.870`.

[OMS09] K. B. Oldham, J. Myland, and J. Spanier: *An Atlas of Functions: with Equator, the Atlas Function Calculator.* Springer New York, 2009, ISBN 978-0-387-48807-3. `https://doi.org/10.1007/978-0-387-48807-3`.

[P+75] M. L. Perl *et al.*: *Evidence for Anomalous Lepton Production in* $e^+ - e^-$ *Annihilation.* Physical Review Letters, 35:1489–1492, December 1975. `https://doi.org/10.1103/PhysRevLett.35.1489`.

[P+16] Particle Data Group: C. Patrignani *et al.*: *Review of Particle Physics.* Chinese Physics C, 40(10):100001, 2016. `https://doi.org/10.1088/1674-1137/40/10/100001`.

[P+19] D. Perevoznik *et al.*: *High-speed two-photon polymerization 3D printing with a microchip laser at its fundamental wavelength.* Optics Express, 27(18):25119–25125, September 2019. `https://doi.org/10.1364/OE.27.025119`.

[P+21] T. Pöschl *et al.*: *Measurement of ionization quenching in plastic scintillators.* Nuclear Instruments and Methods in Physics Research Section A: Accelerators, Spectrometers, Detectors and Associated Equipment, 988:164865, February 2021. `https://doi.org/10.1016%2Fj.nima.2020.164865`.

[Pau30] W. E. Pauli: *Offener Brief an die Gruppe der Radioaktiven bei der Gauverein-Tagung zu Tübingen.* December 1930. `https://doi.org/10.1063/1.2995181`, In L. M. Brown: *The idea of the neutrino.* Physics Today, 31(9):23–28, September 1978.

[Pon58a] B. Pontecorvo: *Mesonium and Antimesonium.* Journal of Experimental and Theoretical Physics, 6(2):429–431, February 1958. `http://jetp.ras.ru/cgi-bin/dn/e_006_02_0429.pdf`.

[Pon58b] B. Pontecorvo: *Neutrino Experiments and the Problem of Conservation of Leptonic Charge.* Journal of Experimental and Theoretical Physics, 26(5):984–988, May 1958. `http://www.jetp.ras.ru/cgi-bin/dn/e_026_05_0984.pdf`.

[PR15] H. Päs and W. Rodejohann: *Neutrinoless double beta decay.* New Journal of Physics, 17(11):115010, November 2015. `https://doi.org/10.1088/1367-2630/17/11/115010`.

[PS21] L. Perivolaropoulos and F. Skara: *Challenges for ΛCDM: An update*, 2021. `https://doi.org/10.48550/arXiv.2105.05208`.

[Roy15] The Royal Swedish Academy of Science: *The Nobel Prize in Physics 2015*, October 2015. `https://www.nobelprize.org/uploads/2018/06/press-30.pdf`, visited on July 5th, 2022.

[Rut99] E. Rutherford: *Uranium Radiation and the Electrical conduction Produced by it.* Philosophical Magazine, 47(284):109–163, 1899. `https://doi.org/10.1080/14786449908621245`.

[Rut03] E. Rutherford: *The Magnetic and Electric Deviation of the easily absorbed Rays from Radium.* The London, Edinburgh, and Dublin Philosophical Magazine and Journal of Science, 5(26):177–187, 1903. `https://doi.org/10.1080/14786440309462912`.

[Sac16] I. Sacco: *Development of highly integrated PET/MR detector modules.* PhD thesis, Ruprecht-Karls-Universität Heidelberg (RKUH), 2016. `https://doi.org/10.11588/heidok.00022239`.

[Sai21] Saint-Gobain Ceramics & Plastics, Inc.: *BC-400, BC-404, BC-408, BC-412, BC-416 Premium Plastic Scintillators*, October 2021. `https://www.crystals.saint-gobain.com/sites/hps-mac3-cma-crystals/files/2021-10/BC400-404-408-412-416-Data-Sheet.pdf`, visited on July 5th, 2022.

[Sch20] A. K. Schaller: *Characterization and mitigation of the background in KATRIN.* PhD thesis, Technische Universität München (TUM), 2020. `http://nbn-resolving.de/urn/resolver.pl?urn:nbn:de:bvb:91-diss-20200828-1553598-1-6`.

[Sch21] Y. Schätzle: *Parameter study on the geometry of microchannel plates for the KATRIN-Experiment.* Bachelor's thesis, Karlsruher Institut für Technologie (KIT), May 2021.

[Sga20] D. Sgalaberna, U. Kose & A. De Roeck (CERN): *Using 3D printing techniques for future neutrino detectors*, March 2020. `https://ep-news.web.cern.ch/content/using-3d-printing-techniques-future-neutrino-detectors`, visited on July 5th, 2022.

[SM05] J. E. Sansonetti and W. C. Martin: *Handbook of Basic Atomic Spectroscopic Data.* Journal of Physical and Chemical Reference Data, 34:1559–2259, September 2005. `https://doi.org/10.1063/1.1800011`.

[Sod13] F. Soddy: *The Radio-Elements and the Periodic Law.* Nature, 91:57–58, March 1913. `https://doi.org/10.1038/091057a0`.

[Spi12] C. Spiering: *Towards high-energy neutrino astronomy.* The European Physical Journal H, 37:515–565, July 2012. `https://doi.org/10.1140/epjh/e2012-30014-2`.

[Tor00] L. Torrisi: *Plastic scintillator investigations for relative dosimetry in proton-therapy.* Nuclear Instruments and Methods in Physics Research Section B: Beam Interactions with Materials and Atoms, 170(3):523–530, October 2000. `https://doi.org/10.1016/S0168-583X(00)00237-8`.

[TR21] C. Trigila and E. Roncali: *Integration of polarization in the LUTDavis model for optical Monte Carlo simulation in radiation detectors.* Physics in Medicine & Biology, October 2021. `https://doi.org/10.1088/1361-6560/ac2e18`.

[Tro19] N. R.-M. Trost: *Modeling and measurement of Rydberg-State mediated Background at the KATRIN Main Spectrometer.* PhD thesis, Karlsruher Institut für Technologie (KIT), 2019. `https://doi.org/10.5445/IR/1000090450`.

[Wan13] N. Wandkowsky: *Study of background and transmission properties of the KATRIN spectrometers.* PhD thesis, Karlsruher Institut für Technologie (KIT), 2013. `https://doi.org/10.5445/IR/1000036631`.

[Wei04] S. Weinberg: *The Making of the Standard Model.* The European Physical Journal C – Particles and Fields, 34:5–13, May 2004. `https://doi.org/10.1140/epjc/s2004-01761-1`.

[Wik15] Wikimedia Commons: *Uranium-238 decay chain diagram*, June 2015. `https://commons.wikimedia.org/wiki/File:Decay_chain(4n%2B2,_Uranium_series).svg`, visited on July 5th, 2022.

[Wik21] Wikimedia Commons: *Standard Model of Elementary Particles*, December 2021. `https://commons.wikimedia.org/wiki/File:Standard_Model_of_Elementary_Particles.svg`, visited on July 5th, 2022.

[Z$^+$18] Z. Zong *et al.*: *Study of light yield for different configurations of plastic scintillators and wavelength shifting fibers.* Nuclear Instruments and Methods in Physics Research Section A: Accelerators, Spectrometers, Detectors and Associated Equipment, 908:82–90, November 2018. `https://doi.org/10.1016/j.nima.2018.08.029`.

[Z$^+$20] Particle Data Group: P. A. Zyla *et al.*: *Review of Particle Physics.* Progress of Theoretical and Experimental Physics, 2020(8), August 2020. `https://doi.org/10.1093/ptep/ptaa104`, 083C01.

[Zub20] K. Zuber: *Neutrino Physics*, volume 3rd edition of *Series in High Energy Physics, Cosmology, and Gravitation.* CRC Press, 2020, ISBN 9781138718890. `https://doi.org/10.1201/9781315195612`.

List of Abbreviations and Acronyms

0νββ neutrinoless double beta decay.

2PP two-Photon Polymerization.

2pTEF double passive Transverse Energy Filter.

AFM Atomic Force Microscopy.

AP Analyzing Plane.

APD Avalanche Photodiode.

APH Institute of Applied Physics.

aTEF active Transverse Energy Filter.

BBR Black Body Radiation.

BIXS Beta-Induced X-ray Spectroscopy.

BSM Beyond the Standard Model.

CνB Cosmic Neutrino Background.

CFN Center for Functional Nanostructures.

CMOS Complementary Metal-Oxide-Semiconductor.

CPS Cryogenic Pumping Section.

CRES Cyclotron Radiation Emission Spectroscopy.

DAQ Data Acquisition.

DPS Differential Pumping Section.

EC Electron Capture.

EMCS Earth Magnetic field Compensation System.

FBM Forward Beam Monitor.

FPD Focal Plane Detector.

FPGA Field Programmable Gate Array.

FRET Förster Resonance Energy Transfer.

FSD Final State Distribution.

GEANT Geometry And Tracking.

IDP Interpolating Digital Photosensor.

IE Inner wire Electrode system.

KATRIN Karlsruhe Tritium Neutrino experiment.

KIT Karlsruhe Insititute of Technology.

KNM KATRIN Neutrino Mass campaign.

LARA Laser Raman Spectroscopy.

LFCS Low-Field Correction System.

LIGA *Lithographie, Galvanoformung und Abformung* (lithography, electroplating and molding).

LN_2 Liquid Nitrogen.

LYSO $Lu_{2(1-n)}Y_{2n}SiO_5$, Lutetium-yttrium oxyorthosilicate.

MAC-E Magnetic Adiabatic Collimation combined with an Electrostatic filter.

MS Main Spectrometer.

NAP Normal Analyzing Plane.

NEG Non-Evaporable Getter.

OAR Open Area Ratio.

PAE Post Acceleration Electrode.

PCB Printed Circuit Board.

PDE Photon Detection Efficiency.

PDF Probability Density Function.

PIN Positive Intrinsic Negative (diode).

PMMA Poly(Methyl Methacrylate).

PMT Photomultiplier Tube.

PS Pre-Spectrometer.

pTEF passive Transverse Energy Filter.

PVT Polyvinyltoluene.

RMSD Root-Mean-Square Deviation.
ROI Region Of Interest.
RW Rear Wall.
R&D Research and Development.

SAP Shifted Analyzing Plane.
SBR Signal-to-Background Ratio.
scint-aTEF scintillating active Transverse Energy Filter.
SDS Spectrometer and Detector Section.
SEM Scanning Electron Microscopy.
Si-aTEF Silicon active Transverse Energy Filter.
SiPM Silicon Photomultiplier.
SM Standard Model.
SNR Signal-to-Noise Ratio.
SPAD Single-Photon Avalanche Diode.
STS Source and Transport Section.

TEF Transverse Energy Filter.
TIR Total Internal Reflection.
TTA Triplet-Triplet Annihilation.

UHV Ultra-High Vacuum.
UI User Interface.

WGTS Windowless Gaseous Tritium Source.

XML Extended Markup Language.

ZITI *Institut für Technische Informatik* (Institute of Computer Engineering).

List of Figures

List of Tables